Heisenberg antiferromagnetique model sur le pavage quasicrystaux bidimensionnelle

Attila Szallas

Attila Szallas. Heisenberg antiferromagnetique model sur le pavage quasicrystaux bidimensionnelle. Condensed Matter [cond-mat]. Université Paris Sud - Paris XI, 2008. English. NNT : . tel-00358251

Université de Paris-Sud - Laboratoire de Physique des Solides

Heisenberg Antiferromagnetic model on 2D quasiperiodic tilings

Thèse presentée pour obtenir le grade de

Docteur en Sciences de l'Université de Paris-Sud, Orsay

Discipline : Physique

par

Attila SZÁLLÁS

Soutenue le 14 Novembre 2008 devant la Commission d'examen:

Michel HÉRITIER	Président
Françoise HIPPERT	
Ferenc IGLÓI	Rapporteur
Anuradha JAGANNATHAN	Directeur de thèse
Didier MAYOU	
Timothy ZIMAN	Rapporteur

Contents

Acknowledgements

I would like to thank my advisor, Anu Jagannathan, for her continuous help, teaching, advices and great support of my work. It was a very nice time to working together.

I would like to thank the director of the Laboratoire de Physique des Solides, Prof. Jean-Paul Pouget, for his support in my work. Also I would like to thank the heads of the Theory Group of the LPS, Gilles Montambaux, and earlier, Pascal Lederer for their support. I am indebted to the LPS staff. Their hospitality and support was very nice. It was distinguished pleasure to work in the Theory Group of the LPS that provide me an intriguing working environment in the condensed matter science.

I would like to thank Prof. Ferenc Iglói and Timothy Ziman that they accepted to be my referees. Prof. Ferenc Iglói was also the advisor of my Master's thesis. I am also indebted to him for his teaching and support in that period and after that. I would like to thank Prof. Michel Héritier, that he accepted to be the president of the jury. I would like to thank Françoise Hippert and Didier Mayou, that they accepted to participate in the jury.

I am indebted to Stefan Wessel, the collaboration, the precise Quantum Monte Carlo simulations and the encouragements of him. I am also indebted to Michel Duneau, the collaboration and several discussions.

I would like to thank, my collagues, Piotr Chudzinski, Giovanni Sordi, Adriano Amaricci, the great discussions and advices that helped my work a lot.

I am grateful so much to Beata Kis. Her love, encouragements and vivacious personality was a continuous source of support for me. I am also very grateful to my parents and my brother, Zsolt, their immense love, sacrifice and encouragements supported my work very much.

I would like to thank, the Marie Curie Foundation of the European Union that they supported my work through the contract, MEST CT 2004-51-4307. I would like to thank also the Collegium Hungaricum, the Institut Hongrois de Paris that they provide me the opportunity for living in the Cite Universitaire de Paris.

Résumé

Le pavage de Penrose est une structure quasipériodique bidimensionnelle, utilisée dans la description des composés quasicristallins. Cette structure est parfaitement ordonnée, avec une symétrie de rotation cinq et elle est invariante sous un changement d'échelle par un facteur τ (le nombre d'or). On s'attend à ce que les propriétés d'un modèle d'antiferromagnétisme dans un tel système diffèrent nettement de celles des antiferromagnétiques périodiques. Nous avons étudié les propriétés d'un modèle d'Heisenberg sur le pavage de Penrose construit à partir de losanges, en utilisant une méthode de développement en ondes de spin. Les énergies et fonctions d'ondes des magnons (quantum d'une onde des spins) ont été étudiées dans le cadre d'une théorie linéarisée. A basse énergie, on trouve une loi de dispersion linéaire, comme dans d'autres antiferromagnetiques bipartites, avec une vitesse effective de l'onde de spin inférieure à celle d'un réseau carré équivalent. Les propriétés spatiales des modes propres ont été étudiées en détail. A basse énergie, nous trouvons que les états propres sont relativement étendus. Une analyse multifractale montre qu'ils sont de type "critique", ayant une distribution d'exposants multifractaux. Aux énergies plus élevées, les états deviennent plus localisés, et, en fonction de l'énergie, l'amplitude de la fonction d'onde est non-nulle autour d'un sous-ensemble de sites d'une valeur de coordinence donnée.

L'énergie de l'état fondamental de cette antiferromagnetique, et la distribution des aimantations locales dans cet état ont été calculés. Des projections dans l'espace perpendiculaire montrent la simplicité sous-jacente de ce état "complexe". Un simple modèle analytique, l'étoile de Heisenberg à deux niveaux, a été présenté pour expliquer de la distribution d'aimantation locales dans ce système antiferromagnétique.

Dans une dernière partie, les effets de désordre de type "phason" sont considérés. Nous avons progressivement augmenté le désordre géometrique de la structure originale. Nous avons trouvé que l'etat fondamental conserve son ordre de Néel, mais que la forme de la distribution ainsi que la norme des aimantations sont modifiés. Nous montrons, à l'aide d'un développement en ondes des spin ainsi que par Quantum Monte Carlo, que l'aimantation alternée diminue exponentiellement vers une valeur asymptote en fonction du désordre. La distribution spatiale de magnetizations locales devient plus homogène par rapport à pavage parfait. La vitesse des ondes des spin augmente avec le désordre, et les singularités dans le spectre et les functions d'onde sont en partie lissées. Ces résultats sont comparés avec des résultats connus dans des systèmes désordonnés.

Mots clés: quasicrystaux, le pavage de Penrose, model d'Heisenberg, ondes de spin

Chapter 1

Introduction

Crystals, or periodic solids, show a large variety of structural forms. Their physical properties, phases under different environmental circumstances and depending on their constituent elements and their relations are extremely diverse. Much of modern technology is based on crystalline materials including semiconductors, liquid crystals and superconductors to name a few. It is well-known that periodic solids have symmetry properties restricted to invariance under 2-, 3-, 4-, and 6 -fold point rotations because of physical space is 3 dimensional. Quasicrystals, however, are less restricted due to the relaxation of the condition of strict translational invariance. The physical properties of quasicrystals can be expected to be as diverse, and probably more complex, than those of periodic crystals.

The notion of quasiperiodicity has existed in the mathematical community from 1933 due to work on quasiperiodic functions, introduced by Harald Bohr as a subset of almost periodic functions. The quasiperiodic functions show long range order without periodicity. As regards tilings, the simplest and oldest example of a one-dimensional tiling is the Fibonacci chain. Quasi-crystalline tilings were possibly also known to medieval islamic scientists five centuries before their discovery in the West [1]. The mathematician R. Penrose discovered the five-fold symmetric tiling that bears his name [2], more than a decade before the discovery of axes of five-fold symmetry in a metallic alloy.

In this thesis we will be concerned with quantum magnetism in a quasiperiodic environment, more specifically, with the Heisenberg antiferromagnet in different types of two-dimensional quasiperiodic tilings. The main model studied is the Penrose rhombus tiling, which occupies an important place in the history of quasicrystals and has been studied extensively. To set the context, we begin by describing some simple examples of quasicrystals in increasing spatial dimensions: d=1, d=2, and d=3.

1.1 Quasiperiodic tilings

1.1.1 (1D) The Fibonacci sequence

First of all we are presenting a well known example of the quasiperiodic structure, the Fibonacci sequence, to introduce some main ideas concerning the quasiperiodic structures. The Fibonacci sequence is a one dimensional aperiodic sequence. It is built up from two segments: a "long" and a "short" one, hereafter denoted L and S respectively. The sequence could be built iteratively due to this substitution rule:

$$\sigma = \begin{cases} L \rightarrow LS \\ S \rightarrow L \end{cases} \tag{1.1}$$

where the zeroth element is $F_0 = S$ and the first element is $F_1 = L$. The generated sequence has several nice properties. The sequence itself is self similar in the sense that the sequence after n+1 iteration could be built up due to putting together the sequences after n and n-1 iteration:

$$F_{n+1} = F_n + F_{n-1} \tag{1.2}$$

In this way the last $\#(F_{n-1})$ elements will be similar to the first $\#(F_n)$ one and the first $\#(F_n)$ one to the whole sequence, and so on; where $\#(F_n)$ is the number of elements of the F_n sequence. During iteration the ratio between the number of L elements and the number of S elements is quickly converge to the Golden Ratio: $\tau = \frac{1+\sqrt{5}}{2}$ that is a root of the $x^2-x-1 = 0$ algebraic equation and approximately 1.618034. If one use the substitution $S = 0$ and $L = 1$, and generate the Fibonacci sequence, the sum of the elements after n iteration will be equal with the nth number of the Fibonacci Series: $0, 1, 1, 2, 3, 5, 8, 13, 21, 34, \ldots$. The Fibonacci sequence is often appears in the nature: branching in trees, arrangement of leaves on a stem, the fruitlets of a pineapple, the flowering of artichoke, an uncurling fern and the arrangement of a pine cone. The Fibonacci sequence is quasiperiodic because there is no any finite periodic sequence that could cover the whole infinite sequence but as we have seen the sequence is deteministic due to the substitution rule and has self similarity also.

1.1.2 (2D) The Penrose tiling

In 1974 Roger Penrose showed that it is possible to cover the whole plane with one continuous layer in a non periodic way using just two elements of the rhombuses say: "kite" and "dart" [2]. There is an equivalent covering using "thin" and "thick" rhombuses (Fig. 1.1) where the "thin" rhombus has the angles of $\frac{2\pi}{10}$ and $\frac{8\pi}{10}$ radians and the "thick" one has the angles of $\frac{4\pi}{10}$ and $\frac{6\pi}{10}$ radians. To cover the whole plane using these two basic elements

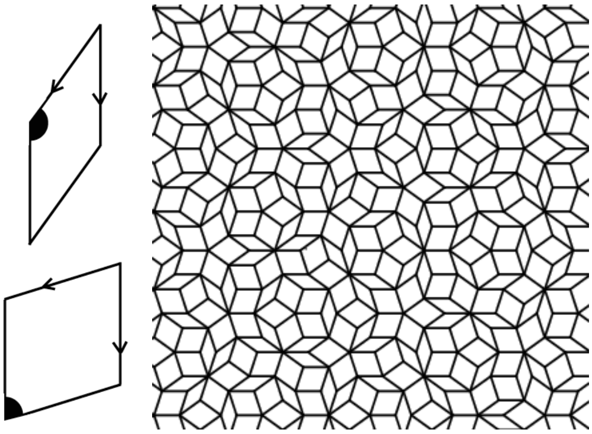

Figure 1.1: In the left there are the two basic rhombuses of the Penrose tiling: the ”thin” (in the top left of the picture) and the ”thick” one (in the left bottom of the picture). In the right there is a finite element of the Penrose tiling.

the rhombuses have to arrange in such a way that they obey certain matching rules (See Fig. 1.1).

Matching rules:

- Each vertices is either fully black or fully blank.
- Two adjacent edges either have both arrows or they are both blank.

The matching rule gives rise to infinitely many Penrose tilings. In this thesis, the term ’Penrose-tiling’ refers to one of these. The Penrose tiling has 5-fold rotational invariant but in a ”weak” sense. It means that for any given pattern, its equivalent under rotation by a multiple of $\frac{2\pi}{5}$ can be found elsewhere on the tiling. The Penrose tiling is self similar under a scale change by a factor of the golden mean τ. More precisely, this means that the structure transforms under so-called inflation (deflation) transformations in such a way as to yield an equivalent tiling of larger (smaller) edge length. Inflation is a reversible operation which can be thought of as a set of decimations of vertices, followed by a re-connection of the new vertices. The equivalence of the old and new structures means here that no environments are created or destroyed in the process of inflation or deflation, and that one can find an exact match between any of the two structures. The structure of the Penrose tiling is closely related to the Fibonacci sequence and to the τ. The ratio of the thick to the thin rhombuses is converge to τ. The sequences of neighbouring rhombuses with parallel sides, are Fibonacci ordered appearances of thick to the thin rhombuses. These are the Conway worms.

1.1.3 (2D) Octagonal tiling

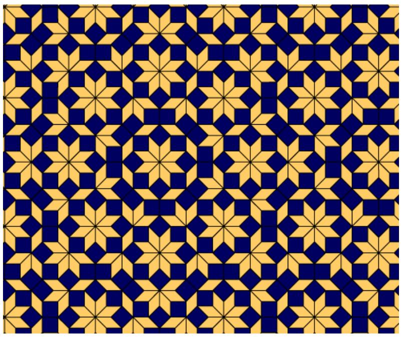

Figure 1.2: The Ammann-Beenker tiling. (The figure was taken from the 'Tilings Encyclopedia' webpage: http://tilings.math.uni-bielefeld.de/).

In 1977 R. Ammann found several sets of aperiodic tiles. One of that was the octagonal or Ammann-Beenker tiling (See Fig. 1.2). The octagonal tiling has perfect 8-fold symmetry. It is self similar under a scale change by the factor of the 'silver mean': $\lambda = 1 + \sqrt{2}$ [3], another example of a quadratic irrational.

1.1.4 (3D) Icosahedral tiling

The icosahedral tiling is one of the most extensively studied tilings in three dimensions. Many of the quasicrystals discovered have icosahedral symmetry, including the very first alloy based on Al and Mn, and can be described using the icosahedral tiling. The icosahedral tiling has the same symmetry properties like the regular icosahedron. The tiling is filling the space with two kinds of polyhedrons, the prolate and oblate rhomboedras, the facets of which have the same rhombic shape. The Penrose tiling is closely related to the icosahedral because of their symmetry properties. The symmetry group of the Penrose tiling is an irreducible subgroup of the symmerty group of the icosahedral tiling. Because of this similarity the icosahedral tiling has the name also 3D Penrose tiling.

1.2 Diffraction properties of the quasiperiodic structures

1.2.1 Diffraction studies

Quasicrystals can be studied by diffraction of *electrons*, *X-rays,* or *neutrons.* All these techniques are based on the interference effects produced by the phase differences between scattered waves of the particles mentioned above. Each atom in the sample may be consid-

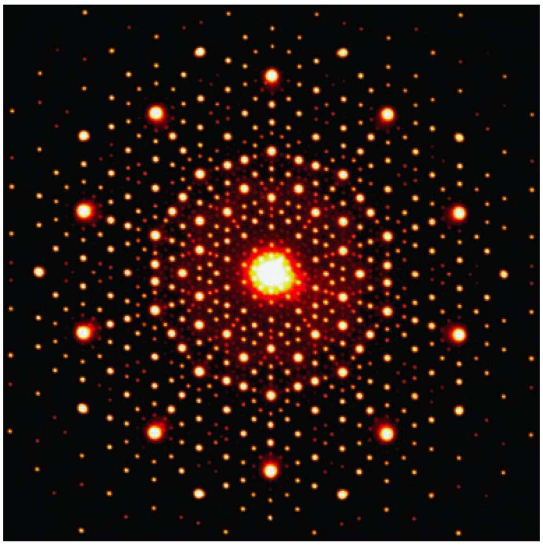

Figure 1.3: Electron diffraction patterns taken along the tenfold symmetry axis of the $Al_{72}Ni_{20}Co_8$ decagonal quasicrystal, one of the best quasiperiodic ordered materials available today. (The figure was taken from [4])

ered to be a source of secondary spherical waves with a scattering power, peculiar to the atom considered. The diffraction experiment provides the structure factor, which is related to the Fourier transform of the real space distribution of the atoms (See Fig. 1.3). The symmetry properties of the structure factor are thus related to those of the atoms.

1.2.2 Discovery of the quasicrystals

Although for long time tilings were simply a mathematical curiosity, till Dan Shechtman and his group in April observed a metallic solid (AlMn) with long range orientational order but with icosahedral point group symmetry [5] in 1982. They rapidly cooled down AlMn alloys from the melt. During first order phase transition 1 μm grains solidified out, of a different phase than the other crystalline Al-alloys. The electron diffraction patterns clearly displayed the six fivefold, ten threefold and fifteen twofold axes of the icosahedral symmetry that is inconsistent with translational invariance of the lattice. But the diffraction peaks were sharp, δ-function like, similar like in periodic crystals. This discovery of Shechtman, Blech, Gratias and Cahn influenced a series of theoretical and experimental studies about quasiperiodicity and quasi-crystalline materials. Since then, many new quasi-crystalline compounds have been and are still being discovered. Most of them are transition metal compounds (Al, V, Mn, Cu, Fe, Co, Ni -based) that show 5, 8, 10, 12 -fold rotational symmetry, respectively. Most are metastable, although they appear to be stable around room temperature.

1.2.3 Diffraction properties of the quasicrystals

The main properties of the quasicrystals are a point like diffraction pattern as in periodic crystals, but with rotational symmetries inconsistent with translational invariance in three dimensions:

- The diffraction pattern shows fine peaks that appear everywhere in the whole reciprocal space without restricted region like the Brillouin zone for periodic crystals. It means that there's no shortest wavelength in real space that is equivalent with the lack of translation invariance.
- The diffraction peaks $\vec{q}$ are possible to indexed unambiguously with N indices where N is finite and bigger than 3 (1.3). It means that the quasiperiodic structure is a projection of a periodic structure in a hyperspace with dimension bigger than 3.

$$\vec{q} = \sum_{i=1}^{N} n_i \vec{e}_i, \qquad n_i \in \mathbb{Z} \tag{1.3}$$

More precisely, the quasiperiodic structure forms a $\mathbb{Z}$ -module. The $\mathbb{Z}$ -module with *rang N* in a d-dimensional space can be considered to be an irrational projection of a periodic lattice in N dimensions. This is the property on which the 'cut and project method for obtaining tilings is based on. The real space quasiperiodic structure has an another property that is important in non-periodic structures: self similarity under the scale change by a factor of an irrational number (also called hierarchical symmetry).

1.2.4 The new definition of the crystals

Quasicrystals are now treated on an equal footing as crystals, and in 1991 the International Union of Crystallography amended the definition of crystal, reducing it to the ability to produce a clear-cut diffraction pattern and acknowledging the possibility of the ordering to be either periodic or aperiodic.

1.3 Puzzles about the structure

The real structures of quasi-crystalline materials remains a puzzle. At the time of the discovery of the quasicrystals it was debated whether quasi-crystalline material really were a new state of matter. Linus Pauling one of the greatest crystallographer of the 20th century argued that quasicrystals are not different than periodic crystals but ”just” twinned (periodic) crystals [6]. This twinned periodic crystal hypothesis was answered due to the careful analysis of the electron and X-ray diffraction experiments. Most models proposed for quasicrystals are based on tilings and assume that the atoms (or clusters of atoms) are situated on the vertexes of a quasiperodic tiling. But why the atoms and molecules do form a complex, quasiperiodic pattern rather than a regularly-repeating, crystal arrangement? For example, in the Penrose tiling, the notion has been that atoms arrange themselves into two types of clusters analogous to rhombic Penrose tiles and have interactions which force connections between clusters analogous to the Penrose matching rules for tiles [7, 8]. An another possible model for quasicrystals was the random tiling model when one suggest the same building blocks like for Penrose tiling but without matching rules. (Elser [9], Henley [10]). In contrast to the perfect tiling, the random tiling has a lower free energy due to the associated entropy, explaining why materials might choose to condense with this type of long range order. Careful X-ray diffraction experiments must be done to distinguish the random tiling from the perfect tiling, as Bragg peaks occur in the same positions - this shows that the geometrical constraints are locally strong enough to ensure that even in random tilings the structure retains long range order with an infinite correlation length. Also for the random tiling model the atoms should arrange themselves into two types of clusters analogous to rhombic Penrose tiles. These models suggest that the conditions necessary to form quasicrystals are significantly more complex than the conditions for forming crystals. Both of these models include the requirement of two types of cluster appears to be necessary to obtain quasiperiodicity. The energetics should be very special that permit two clusters in the just the right proportion in density (and exclude any other clusters), especially considering that most known quasicrystals are composed of metallic elements with central force potentials rather than rigid covalent bonding [11]. In the case of the Penrose picture, there is the additional problem of finding energetics that impose the matching rules. Solving these problems it was suggested to use for model the single repeating cluster. The repeating cluster is analogous to the unit cell in periodic crystals. The novel feature is that the neighboring clusters “overlap.” Atoms in the overlap region are shared by the two clusters enabling the hypothetical surfaces that bound the clusters to interpenetrate [11, 12]. Petra Gummelt have found that the decagonal tiles with appropriately chosen overlap rules can force a perfect quasiperiodic tiling [13]. Jeong and Steinhardt [11] provided a simple, alternative proof which makes clear the isomorphism to two-tile Penrose tilings. A cluster aggregate model has also been suggested [4], but the problem remains open at this time.

1.4 Electronic properties of the quasicrystals

1.4.1 Experimental measurements of electronic properties

Most systems studied show a gap or pseudogap in the electronic density of states close to the Fermi level. One of the most striking properties observed in quasiperiodic metallic alloys are the remarkably low values of the electrical conductivity, which is lower than one would expect, from the pseudogap in the density of states. In the case of $Al-Cu-Fe$ and $Al-Cu-Ru$ alloys, in which stable, virtually defect-free icosahedral phases can be formed, the resistivity is enormous, and increases to over 100 $\mu\Omega m$ as the degree of structural order increases [14, 15, 16, 17]. This is very unusual for metallic alloys. The resistivity decreases at high temperature, contrarily to the usual metallic behavior. Anomalies also appear in thermopower and in the low temperature specific heat [18]. Furthermore, quasicrystals with higher structural perfection show lower conductance [19, 20]. Disorder appears to facilitate transport in the quasicrystal, contrarily to its effect in disordered metals. Finally, studies of complex alloy system for the AlPdMn with very large unit cells show that the conductivity was higher for these than for a single grain quasicrystal of similar composition, although both alloys had comparable structural quality. This could indicate that the transport is not just determined by local properties, but also by the long range quasiperiodic structural order [21].

1.4.2 Theoretical approaches to describe the electronic properties

As regards theory, it is interesting to consider the possibility of Anderson localization, or strong localization, [22] which is known to occur for strongly disorder and/or low dimension. "Localization" refers to the wave function which is modified with respect to the wave-like solutions present in a periodic solid. It can also refer to other types of waves in the solids like acoustic and spin waves, for example. In one dimension the quantum fluctuations is so strong that any kind of randomness could make the system to be localized. Work in disordered crystals has shown that in three dimensions and above, there can occur a transition between localized-delocalized states, called the metal-insulator transition (MIT). This phenomenon exist also in the case of the aperiodic systems, when the aperiodicity was shown to localize the wavefunctions.

In low dimensional systems (mostly in 2D films) also the weak localization is an important effect which occurs in disordered electronic systems at very low temperatures. The effect manifests itself as a positive correction to the resistivity of a metal or semiconductor. The origin of the effect is that the disordered electronic system, the electron motion is diffusive rather than ballistic. The resistivity of the system is related to the probability of an electron to propagate between two given points in space. This probability due to quantum mechanics is a sum of the quantum-mechanical amplitudes of the paths. The weak localization correction can be shown to come mostly from quantum interference between self-crossing paths in which an electron can propagate in the clock-wise and counter-clockwise direction around a loop. Due to the identical length of the two paths along a loop, the quantum phases cancel each other exactly and these (otherwise random in sign) quantum interference terms survive disorder averaging. Since it is much more likely to find a self-crossing trajectory in low dimensions, the weak localization effect manifests itself much stronger in low-dimensional systems (films and wires).

In quasicrystals, in the perfect structure, without disorder, the transport is either ballistic at sufficiently long time (in approximants) or follows a power law also at sufficiently long time. D. Mayou and G. Trambly De Laissardière developed a theory for quantum transport in quasicrystals [23].

A number of standard techniques used in crystals are ruled out in quasicrystals since one cannot use the Bloch-theorem. One does not have exact rotational symmetries for quasiperiodic tilings either, which have rotational invariance just in the weak sense. Two properties that can be exploited in quasicrystals derive from their representation in higher-dimensional space (the cut-and-project method described in Ch.2) and these are the hierarchical structure, and the perpendicular (or internal) space representation. These properties and the properties of the basic blocks (rhombi in general case) like bipartiteness that any calculations could use on quasiperiodic tilings to perform that. The scale invariance of quasiperiodic structures, and in consequence, the potential seen by the electrons, must play an important role in determining the spatial dependence and the energy of the eigenstates. The characteristic singular features in the density of states and other electronic properties are in fact a result of this symmetry.

Calculations for one dimensional quasiperiodic chains

Many methods exist in the 1D case: bosonization technique, renormalization group, DMRG, for example. M. Kohmoto and his coworkers made one of the first contributions to understanding the physics of quasiperiodic chains [24], where they investigated the localization problem on a one dimensional electron model. They have concluded that in the case of quasiperiodic chain the wavefunction won't be localized nor delocalized but always in an intermediate regime between the two. Julien Vidal and his coworkers studied analytically one dimensional interacting spinless fermions in a Fibonacci potential [25]. They showed that the effects of the quasiperiodic modulation are intermediate between those of a commensurate potential and a disordered one. The system exhibits a metal-insulator transition whose position depends both on the strength of the correlations and on the position of the Fermi level. Consequently, the conductivity displays a power law like size and frequency behaviour characterized by a non trivial exponent. Kazuo Hida calculated the low-energy properties of the half-filled Fibonacci Hubbard models using weak-coupling renormalization group and density matrix renormalization group methods [26]. He concluded that in the case of diagonal modulation, weak Coulomb repulsion is irrelevant and the system behaves as a free Fibonacci chain, while for strong Coulomb repulsion the charge sector becomes a Mott insulator and the spin sector behaves as a uniform Heisenberg antiferromagnetic chain. The off-diagonal modulation always drives the charge sector to a Mott insulator and the spin sector to a Fibonacci antiferromagnetic Heisenberg chain.

Calculations in two dimensional tilings

For the electron problem of the two dimensional quasiperiodic tilings many attempts have been made at solving them. V. E. Korepin derived a completely integrable models for quasicrystals. For illustration he calculated the bulk free energy of the Penrose and the icosahedral tiling [27]. C. Sire and J. Bellissard studied a renormalization group attempt for a tight-binding Hamiltonian on the octagonal tiling. In the limit of large potentials compared to the hopping parameters, they found numerical evidences that the spectrum is a Cantor set with zero Lebesgue measure. F. Piechon and A. Jagannathan calculated spectral properties on the octagonal tiling [28, 21, 29]. They find similarities and universal behavior, but also significant differences between quasiperiodic models and models with disorder. Like weakly disordered metals, the quasicrystal can be described by the universal level statistics that can be derived from random matrix theory. Their analysis of spectral rigidity shows that electrons diffuse with a bigger exponent (super-diffusion) than in a disordered metal. Adding disorder attenuates the singular properties of the perfect quasicrystal, and leads to improved transport. Using hierarchical, i.e. self similar properties it is possible to introduce approximative real space renormalization group methods as performed A. Jagannathan on octagonal tiling [30]. She has used an approximative block substitution on the octagonal tiling. The available blocks of spins have reduced and the Hamiltonian of the block was calculated exactly treating like a Heisenberg star cluster [31]. This procedure is possible to redone in the case of another self similar tilings but the exact procedure is not at all obvious. Each tiling is different and her method needs modifications in the case of different tilings.

1.5 Magnetic properties of the quasicrystals

1.5.1 Experimental measurements of the magnetic properties

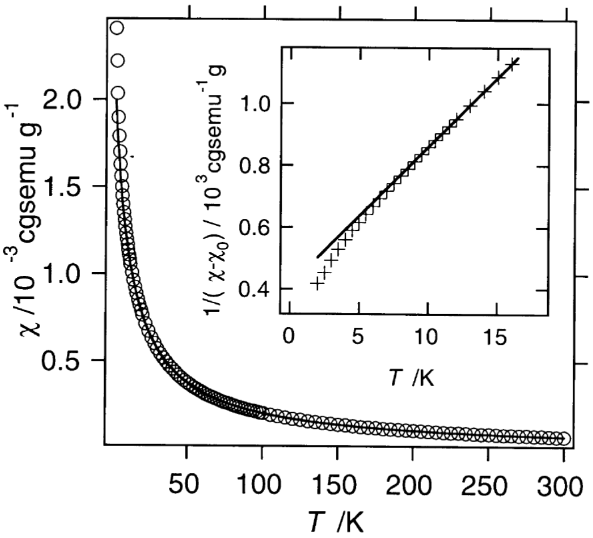

Figure 1.4: Magnetic susceptibility as a function of temperature of $Zn_{60}MgHo_{10}$. Solid curve indicates a least squares fit to Curie–Weiss law. Inset is an enlarged plot of the inverse magnetic susceptibility as a function of temperature. Solid line in the inset indicates a least squares fit to Curie–Weiss law. (This figure was taken from [32].)

Amongst the Al-based quasicrystals, just a few of them are magnetic [33, 34, 35]. In these systems, the magnetic moment originate from the itinerant *d* electrons of the transition-metal elements. The magnetic moment per transition metal atom is typically very small, and there appears to be no magnetic long range order in these compounds. In 1993, an icosahedral quasicrystalline phase were discovered in the Zn-Mg-R compound (R = rare earth elements: R = Gd, Tb, Dy, Ho, Er) [36, 37, 38]. These quasicrystals have well localized 4f electrons and have sizeable moments. X-ray structural studies suggest that the rare earth elements are situated quasiperiodically at definite sites of the quasicrystals [39].

The ZnMgHo compound obeys the Curie-Weiss law at high temperatures [40, 41, 42, 32]. The estimated effective moment is almost equal to that of a Ho^{3+} free ion. This indicates that all Ho atoms in the quasiperiodic lattice sites in the sample have local magnetic moment [32]. The magnetic susceptibility starts to deviate from the Curie-Weiss law below about 6 K [32] (See Fig. 1.4). Then, it abruptly shows spin-glass-like freezing at $T_f \approx 2K$. The spin-glass-like freezing was also detected in the temperature dependence of the ac susceptibility

[42, 43] and muon spin-relaxation μSR rate [44].

Charrier, Ouladdiaf, and Schmitt performed neutron diffraction experiment in powder pattern [45]. They reported coexisting magnetic Bragg reflections and diffuse scattering, which simultaneously developed below T_N, where $T_N \approx 7$ K. They concluded that magnetic long-range order is established below T_N . However, long-range order is consistent neither with the susceptibility, nor with the μSR result. Indeed, two later studies revealed that high quality icosahedral samples exhibit only the diffuse scattering part of the first work [46, 47]. Therefore, from the neutron powder diffraction and the susceptibility, one may conclude that the spins in the Zn-Mg-Ho icosahedral quasicrystal freeze below T_f with the static short-range spin correlations resulting in the magnetic diffuse scattering.

In diffuse neutron scattering experiments, T. J. Sato and his collaborators have found magnetic short range order in the $Zn_{60}Mg_{31}Ho_9$ compound [48, 47, 49]. The measuring temperature was 1.6 K for polarized neutron scattering. This was the first quasiperiodic magnetic compound that showed at least short range order. Later also Sato and his collaborators found the Zn-Mg-Tb to have short range order at 1.4 K [50]. From the neutron scattering intensity maps (Fig. 1.5 for ZnMgHo) both of the two cases (ZnMgHo, ZnMgTe) the magnetic structure of the compound show icosahedral symmetry.

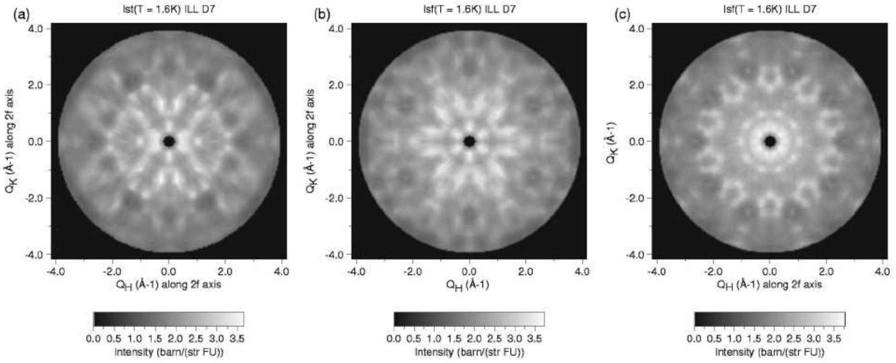

Figure 1.5: Magnetic-scattering intensity maps for ZnMgHo at $T = 1.6$ K for the (a) 2F, (b) 3F, and (c) 5F planes obtained from the spin-flip scattering of polarized neutrons. (from [49])

1.5.2 Theoretical approaches to describe magnetism

Quantum magnetism in a quasiperiodic environment

The discovery of the magnetic order in the Zn-Mg-RE (rare earth) compounds [48, 47, 49, 50] poses the question of magnetic ordering in such systems. As we have mentioned earlier the magnetism in the rare earth compounds is connected to the localized $4f$ electrons. This suggests using a simple Heisenberg model to describe magnetic properties in these quasicrystals. Very little is known about the long range ordered state, when one exists, in such materials. The experimental compounds have frustration and disorder, which complicate the analysis, and can lead to spin glass phase at low temperature. We have chosen to consider a simpler class of models, which are unfrustrated and do allow for long range Neel antiferromagnetic order.

We consider the usual description of the quasicrystals based on tilings, in two dimensions. The reduced dimensionality makes it easier to visualize and allows us to consider larger systems. Due to thermal fluctuations, long range order is only present at zero temperature. We have extensively studied the two dimensional Penrose tiling, taking nearest neighbor couplings which act along the edges of the rhombus.

We (A. Jagannathan and A. Szallas) have performed a linear spin wave analysis (LSWT) on S=1/2 Heisenberg antiferromagnet on the 2D Penrose approximants and its disordered counterparts. Stefan Wessel (Stuttgart University) made the Quantum Monte Carlo (QMC) analysis on the same systems. Before presenting our studies we summarize briefly the earlier achievements in this field.

One dimensional aperiodic spin chains

The aperiodic tiling is a deterministic, non-periodic tiling that could built up from two basic elements and they include the quasiperiodic tilings. There have been many studies of aperiodic spin chains, and many of these use renormalization group (RG) method. The model that is most frequently considered is the classical or quantum Ising model. In general, the (d+1)-dimensional classical and d-dimensional quantum systems have related critical properties [51]. In the presence of a marginal perturbation which leads to non-universal exponents are the corresponding quantum exponents obtained by taking an appropriate limit of the classical expressions. The fluctuations around the average coupling scale with L^{ω}, where ω is the wandering exponent of the aperiodic sequence [51, 52]. The relevance of the aperiodic fluctuations is determined by the Harris-Luck criterion.

$$\omega_c = 1 - \frac{1}{d_m \nu_0} \tag{1.4}$$

where ω_c is the critical fluctuation, d_m is the dimensionality of the fluctuations, ν_0 is the correlation exponent of the physical model. If $\omega > \omega_c$ the fluctuations are relevant, $\omega = \omega_c$ marginal, $\omega < \omega_c$ irrelevant, respectively (Uwe Grimm in [53] pp. 199.). Igloi et al. considered layered Ising model [54] where the layers follow hierarchical sequences. They calculated several bulk and surface critical exponent and concluded that the system is isotropic till the structural fluctuations are less than critical, otherwise anisotropic when the structural fluctuations are critical. In [51] Igloi et al. calculated the critical properties of several aperiodic and the hierarchical chain using exact RG method due to the observation that the spectrum of the zero field Ising model is included by the spectrum of the transfer matrix of the directed walk. J. Hermisson et al. [55] derived the Harris-Luck criterion using exact renomalization scheme for Ising model with coupling that ordered due to an aperiodic tiling generated by substitutions. Igloi et al. [56] compare the aperiodic spin chains with random one. They found the same critical properties at the critical point but differences at the off-critical region. J. Hermisson generalized the exact renormalization group method for XY model and investigate arbitrary aperiodic spin chains [57]. He found that the relevance criteria in general for XY model is different than for Ising model for a given aperiodic chain. T. Tokihiro calculated on the 1D Fibonacci and 2D triadic Penrose tilings, using Heisenberg model with long range hierarchical interactions [58]. To our best knowledge Kazuo Hida has performed the first time calculations on quasiperiodic tiling using Heisenberg Hamiltonian with short range, nearest neighbor interaction [59] using DMRG method. He has developed also a real space renormalization group method for S=1/2 Heisenberg antiferromagnet with couplings ordered by the Fibonacci sequence. He has found that the ground state of this model belongs to a new universality class with a logarithmically divergent dynamical exponent which is neither like Fibonacci XY chains nor like XY chains with relevant aperiodicity. This result was obtained by DMRG calculations and further supported by calculations with renomalization group method. A. Szallas has worked out a block substitution method for the hierarchical quantum Ising, Potts and Heisenberg chain and using the Ma-Dasgupta-Hu renormalization group technique [60, 61] he had calculated the scaling properties of the ground state energy [62]. He found the same scaling exponent in both of the three models. For XXZ model Andre P. Vieira made an important contribution to understand the aperiodic quantum spin chains [63, 64]. He has used the Ma-Dasgupta-Hu renormalization group technique using block substitutions on several aperiodic chains with relevant and marginal aperiodicity.

Ising, XY and classical spin models

For Penrose tiling, real space configurations have been thus far primarily studied in the context of classical spins. Godreche et al. [65] showed an approximative renormalization group method for Ising spins on the Penrose tiling that is closely follows the inflation rules of the tiling, which are easily described in terms of Robinson triangles. They are also able to obtain a phase diagram consisting of a variety of ordered phases. H. Aoyama and T. Odagaki presented a renormalization group analysis of the two-dimensional Ising model on both the Kite-Dart and Rhombi Penrose tilings [66]. They demonstrated the existence of the phase transition and obtain the critical temperature and the thermal critical index. The thermal critical index is found to be close to unity. T. Dotera and R. Abe [67] have performed a high temperature expansion for ln Z of the Ising model on the dual Penrose tiling, where Z is the partition function in the absence of the magnetic field. The critical compressibility factor and the average correlation function are calculated in terms of duality relation. Y. Okabe and K. Niizeki have performed Monte Carlo simulations on Ising model on the Penrose tiling and it dual [68]. They investigated both ferro and antiferromagnetic couplings. They concluded that the duality relation between the critical temperatures with the ferromagnetic coupling holds. And the antiferromagnetic system on the dual Penrose lattice shows no long-range order due to a frustration. Sorensen et al. [69] studied the ferromagnetic Ising model with zero field on Penrose related lattices also with Monte Carlo simulations. They investigated different type of boundary conditions. They conclude that despite its quasiperiodicity, the Ising model on the Penrose tiling belongs to the same universality class as Ising model on the periodic lattices. But the boundary conditions could change the critical behavior. Ledue et al. [70] investigated classical XY model on the Penrose tiling. In their model they consider three type of interactions considering the three type of possible length between sites of the Penrose rhombi. At low frustration their model have antiferromagnetic ground state. They found an evidence for a Kosterlitz-Thouless transition also, like in periodic lattices, in the thermal variation of the specific heat. Vedmedenko et al. has investiagted Monte Carlo simulations [71, 72] on many quasiperiodic tilings, and also Penrose tiling, with classical three dimensional spins. They investigated the stable antiferromagnetic magnetization configurations. They found that the combination of the geometric frustration and the quasiperiodic order of the atoms lead to complicated noncollinear ground states. The structure of the magnetic ground state could be divided into subtilings that are not correspond to the spatial order. In [73] Vedmedenko et al.

investigated ferromagnetic coupling between classical three dimensional spins on the Penrose tiling using Monte Carlo simulations. They found a quasiferromagnetic decagonal structure at weak exchange interaction.

1.6 Outline of the thesis

This thesis is divided into seven chapters. The first three chapters summarize the earlier results of the field, give a general introduction to the subject, and also introduce the main concepts and methods. Chapters 4, 5, 6 present our results. The last chapter summarizes the results and discusses some possible directions for future work. The Appendix shows some technical details that could help clarify the notions mentioned in the main text, and may be useful for those wishing to work in the area.

Chapter 2. The second chapter summarizes the geometrical properties of the quasiperiodic tilings and the methods that one uses for generating the tiling. We present the main generating method, the cut and project method how one could generate quasiperiodic tiling with a projection from a hyperlattice. The cut and project method is described due to the example of the Fibonacci sequence and also the case of an arbitrary tiling where the periodic hyperlattice is arbitrary N dimensional. We present also the oblique projection method that is able to generate quasiperiodic approximants that are structurally very similar like the quasuperiodic tiling but periodic. The second main part is the description of the Penrose tiling. First of all the description of the cut and project method specially in the case of the Penrose tiling. After this we summarize the main properties of the Penrose tiling and its approximants.

Chapter 3. The third chapter describes the physics background of the topic of the thesis. We present the possible ground states for Heisenberg antiferromagnets, their relevance and their properties. We point out the particularity of the structure of the Penrose tiling, like bipartiteness and generally high coordination numbers, concerning the ground state properties of the Heisenberg antiferromagnet. The properties of the ground state, the structure of the Penrose tiling and the demand of relatively big system size, to figure out the quasiperiodicty of the model, suggest one of the possible method for the calculations, namely the linear spin wave approximations (LSWT). We describe the background and the derivation of this method. We describe how it is possible to transform the original Heisenberg Hamiltonian to bosonic operators that are the creation and annihilation operators for magnons. Also we present the linearization of this new bosonic Hamiltonian. For the diagonalization of the Hamiltonian we describe a real space diagonalization method based on earlier works [74, 75]. In the end of the chapter we figure out the requirements of the calculcations that we'd like to perform and the possible methods with that one able to calculate ground state energy at two dimensional quasiperiodic quantum spin system.

Chapter 4. The fourth chapter presents the results concerning the energy spectrum and the properties of the magnon wavefunctions of the Heisenberg antiferromagnet on the Penrose tiling. We describe the different energy regions of the spectrum and its particular features like low energy regions, degenerate states, gaps, pseudo gaps, etc. The second main part is devoted to the presentation of the properties of the magnon wave functions. Firstly we are focusing on the question of the wave function localization. We figure out our results about the dependence of the participation of the wave function on the sites with different coordination numbers. We showed this in the context of the perpendicular space representation, that representation comes directly from the generating method of the quasiperiodic tilings, the cut and project method. In the end of the chapter we perform an inverse participation ratio (IPR) anaysis of the wavefunction and a multifractal analysis also.

Chapter 5. The fifth chapter is devoted to the ground state energy and the description of the spatial distribution of the staggered magnetization on the tiling and an approximative explanation of that. Firstly we present the scaling of the ground state energy and its expectation value for the thermodynamic limit. The second part of the chapter is devoted to the properties of the staggered magnetization. We describe firstly the real space distribution of the staggered magnetization and the finite size scaling of the average staggered magnetization. The coordination number dependence is very important because it is suggested by earlier studies of magnetism on 2D tilings and also because one of the particularity of our topic is the geometrical structure of the tiling on where the physical model based on. So we present the coordination number dependence of the staggered magnetization. And also we perform this analysis in the perpendicular space that show the highly ordered structure of the magnetization on the this tiling. Also we point out an approximative model based on the Heisenberg star clusters for the explanation of the observed distribution of the staggered magnetization. At the end of the chapter we present a static structure factor calculation that make some connections with our calculations and neutron diffraction experiments.

Chapter 6. In the sixth chapter we present our results about the randomization of the quasiperiodic tiling and its consequences in the physical properties. Firstly we introduce the context of disorder in quasiperiodic tilings and a particular excitation that just exist in quasicrystals, the phason excitation. We define a randomly distributed phason flip excitation on our tilings. We present the changes in geometry due to phason flips. We point out the effects of the phason flips on several physical properties like the energy spectrum and wavefunctions, ground state energy, average staggered magnetization, staggered magnetization distribution. Also we make a comparison of the results on ground state energy and average local staggered magnetization done by LSWT and QMC. We figure out some possible explanation of the observed effects due to phason disorder.

Chapter 7. In the seventh chapter we summarize our results and outline some possible research topics that could follow our research. These topics are the LSWT calculations on the 3D icosahedral tiling and the calculations concerning the entanglement properties of the quasiperiodic Penrose tiling.

Appendix In the Appendix we show some derivation and description that could interested by specialists or probably well known facts but necessary for make the thesis to be complete.

Chapter 2

The Penrose tiling and its approximants

2.1 Introduction

The description of the structure of the perfect periodic crystal is mathematically simple, in that all positions can be written in terms of a small set of primitive lattice vectors. The structure of a quasiperiodic tiling is not as trivial: even though all vertices can be expressed as linear combinations of integer multiples of a small set of basis vectors, the allowed linear combinations are not given by a simple rule. In the case of the Penrose tiling, more specifically, all vertices can be expressed in terms of integer multiples of five unit vectors $((1,0),(\cos\theta,\sin\theta),(\cos 2\theta,\sin 2\theta),(\cos 2\theta,-\sin 2\theta),(\cos\theta,-\sin\theta);\theta = 2\pi/5)$ which can be regarded as projections of the five basis vectors of a five-dimensional (5D) cubic lattice (See Fig. 2.2). This tells us that the sites can be obtained by projecting points of a 5D hyperlattice onto the physical (also called parallel) 2-dimensional space. The 2-dimensional physical space corresponds to an irrational plane of the hypercubic lattice, and this rules out the possibility of a periodic repetition length in any direction of the $x-y$ plane. The projection matrices and the general formalism for obtaining this tiling by the so-called 'cut and project' method is described in [76]. We should mention that other methods exist to obtain Penrose tilings, such as the multigrid method ([77] pp. 26), inflation of elementary tiles [78, 79, 80], or growth from an intial seed using matching rules [2]. In this chapter we will describe the cut and project method, which we chose for its relative simplicity and adaptability.

For numerical calculations we use approximant tilings (or just in simple, approximants) of the perfect infinite quasiperiodic Penrose tiling. The approximants are generated by the so-called oblique projection method (described in the Appendix). Briefly, the points lying in the volume selected for projection in the 5D lattice are selected according to a rationally oriented plane, and this gives rise to a periodic structure of a unit cell size that can be arbitrarily large, approaching the infinite quasicrystal in the limit of infinite size.

2.2 The 'cut and project' method

The 'cut and project' method [81, 82, 76, 83, 84, 85, 86] as we mentioned in the introduction was developed to obtain quasiperiodic tilings.

2.2.1 The cut and project method for the Fibonacci tiling

To illutrate the method we will begin by presenting the well-known 1D example: the generation of the Fibonacci tiling by the cut and project method.

One considers a two dimensional square lattice: $\mathbb{Z}^2$ that has X and Y axis, respectively. Consider the straight line E that has irrational orientation compare to X, Y: $\tau' = \tan\Theta_{EX}$ and $\tau'' = \tan\Theta_{EY}$ where τ', τ'' are irrational numbers (Fig. 2.1). This is the line that will be tiled. Moving a unit square C, parallelly to the plane of the square lattice and fixing one of its point to E, we get a strip, S. S will contain a line that is broken in integer points. This line is periodic if and only if τ' is rational number. The tiling on E is now obtained by projecting orthogonally the broken points of this line to E. The projections on E will be a quasiperiodic tiling of lengths A $= \sin\Theta_{EX}$ and B $= \cos\Theta_{EX}$. If $\tan\Theta_{EX} = \tau$, the golden mean, the tiling on E will be the Fibonacci tiling. In particular if one take τ' through a sequence of rational slope, τ'_n where the sequence is converging to the irrational τ, one get a sequence of periodic tilings that have a periodic length converging to infinity. These are the approximants of the Fibonacci tiling.

2.2.2 The cut and project method for arbitrary quasiperiodic tiling

Now we describe the cut and project method in arbitrary dimension. There exist several equivalent description of the cut and project method. We have chosen the method described below because it is easy to generalize to get the oblique projection method (described in the Appendix).

One considers an N dimensional square lattice, Λ.

$$\Lambda = \mathbb{Z}^N \tag{2.1}$$

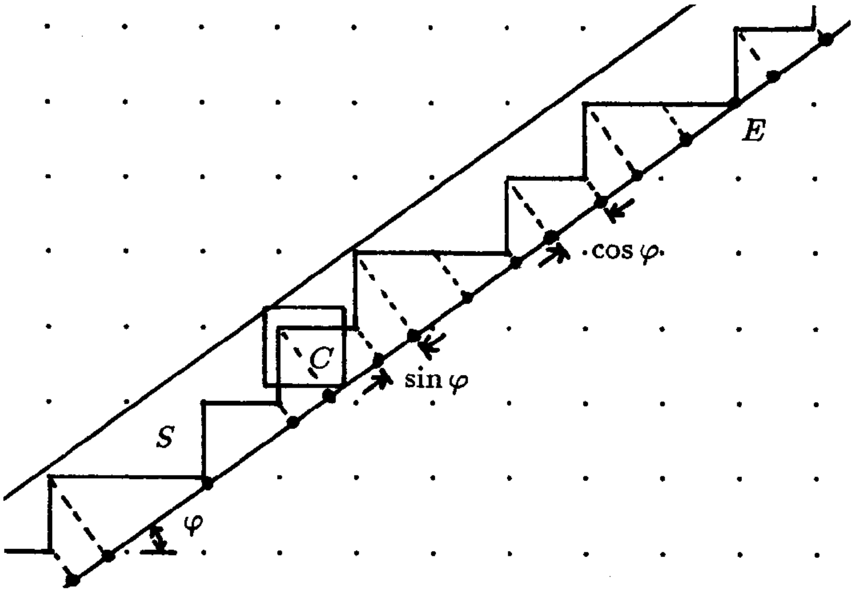

Figure 2.1: Generating the Fibonacci tiling by the 'cut and project' method. (The figure was taken from the dissertation of [87])

We suppose that Λ has n-fold rotational invariance, represented by the discrete rotation group Γ^n. Let C be the unit hypercube of $\mathbb{R}^N$. One considers the irreducible subgroups of the rotation group Γ^n. Consider one of them, called $\Gamma^n_{E_{||}}$. Choosing $\Gamma^n_{E_{||}}$ depends on the structural properties that the tiling should fulfill (e.g. the type of rotational invariance). Consider $E_{||}$, an $N_{||}$ dimensional subspace of $\mathbb{R}^N$ that is invariant under $\Gamma^n_{E_{||}}$. The basis of $E_{||}$ will be a certain transformation of the basis of Λ:

$$E_{||}(j) = \sum_{i=1}^{N} q_{ji} \cdot \Lambda_i \tag{2.2}$$

where $E_{||}(j)$ is the basis vector of $E_{||}$, and Λ_i is the basis vector of Λ, respectively. One considers $E_{\perp}$, the $N_{\perp} = N - N_{||}$ dimensional subspace of $\mathbb{R}^N$ that is perpendicular to $E_{||}$. One considers the orthogonal projections $\Pi_{||}$ to $E_{||}$, and $\Pi_{\perp}$ to $E_{\perp}$. One projects the unit hypercube C, to $E_{\perp}$:

$$W = \Pi_{\perp}(C) \tag{2.3}$$

The projected object, W, will be the so called "window". One projects a point, X, of Λ, to $E_{||}$, if $\Pi_{\perp}(X)$ will be included by W. The point set $\Lambda_{||} = \Pi_{||}(\Lambda)$ will be invariant under

$\Gamma^n_{E_{||}}$.

The orientation of $E_{||}$ is depends on q_{ji}-s. If q_{ji}-s are just rational numbers $\Lambda_{||}$ will be periodic. If q_{ji}-s are just irrational numbers $\Lambda_{||}$ will be quasiperiodic. In the mixed case when q_{ji} are partly rational and irrational the $\Lambda_{||}$ will be periodic in some direction but quasiperiodic in certain others. In general $\Lambda_{||}$ will not have perfect n-fold rotational invariance because $\Lambda_{||}$ is invariant just under $\Gamma^n_{E_{||}}$ but not under Γ^n.

2.3 The Penrose tiling

2.3.1 The Penrose tiling by cut and project method

In 5 dimensions, the hypercubic lattice $\Lambda = \mathbb{Z}^5$ is invariant under 5-fold rotations. One could represent the 5-fold rotations in 5 dimension with $\hat{\gamma}$:

$$\hat{\gamma} = \begin{pmatrix} 0 & 0 & 0 & 0 & 1 \\ 1 & 0 & 0 & 0 & 0 \\ 0 & 1 & 0 & 0 & 0 \\ 0 & 0 & 1 & 0 & 0 \\ 0 & 0 & 0 & 1 & 0 \end{pmatrix} \tag{2.4}$$

One can check: $\hat{\gamma}^5 = \hat{\mathbf{1}}$. The 5-fold rotation group Γ that have the orthogonal representation $\hat{\gamma}$ is not irreducible, but decomposes into 3 irreducible subgroups: $\Gamma_{E_{||}}, \Gamma_{E_{\perp}}, \Gamma_{\Delta}$, respectively. The $\Gamma_{E_{||}}$ and $\Gamma_{E_{\perp}}$ are invariant in 2 dimensional subspaces: $E_{||}$ and $E_{\perp}$, respectively. The Δ is invariant in a 1 dimensional subspace: (1, 1, 1, 1, 1). All the 3 subspaces are orthogonal to each other. The $E_{||}$ is called the parallel subspace and the direct sum of the $E_{\perp}$ and Δ is called the perpendicular subspace. The restriction of $\hat{\gamma}$ to $E_{||}$ is a $\frac{2\pi}{5}$ rotation around the Δ axis. The restriction of $\hat{\gamma}$ to $E_{\perp}$ is a $\frac{4\pi}{5}$ rotation around the Δ axis too. The invariant subspaces are determined by their orthogonal projection operators also: the projector operator that project from Λ to that subspace. The projectors in orthogonal basis are the following.

The projector to $E_{||}$:

$$M_{||} = \sqrt{\frac{2}{5}} \begin{pmatrix} 1 & \cos\theta & \cos 2\theta & \cos 2\theta & \cos\theta \\ 0 & \sin\theta & \sin 2\theta & -\sin 2\theta & -\sin\theta \end{pmatrix} \tag{2.5}$$

The projector to the perpendicular subspace, $E_\perp \bigoplus \Delta$:

$$M_\perp = \sqrt{\frac{2}{5}} \begin{pmatrix} 1 & \cos 2\theta & \cos\theta & \cos\theta & \cos\theta \\ 0 & \sin 2\theta & -\sin\theta & \sin\theta & -\sin 2\theta \\ \frac{1}{\sqrt{2}} & \frac{1}{\sqrt{2}} & \frac{1}{\sqrt{2}} & \frac{1}{\sqrt{2}} & \frac{1}{\sqrt{2}} \end{pmatrix} \tag{2.6}$$

where $\theta = 2\pi/5$. The projected hyperlattice, $M_{||}(\Lambda)$ is a $\mathbb{Z}$ - module that built up from 5 vectors that form a regular pentagon because of the $\frac{2\pi}{5}$ rotations (See Fig. 2.2). In a similar way also $M_\perp(\Lambda)$ is a $\mathbb{Z}$ - module that built up from 5 vectors that form a regular pentagon but with permuted base vectors because of the $\frac{4\pi}{5}$ rotations and the plane is shifted with $\frac{1}{\sqrt{5}}$ to the direction of Δ (See Fig. 2.2).

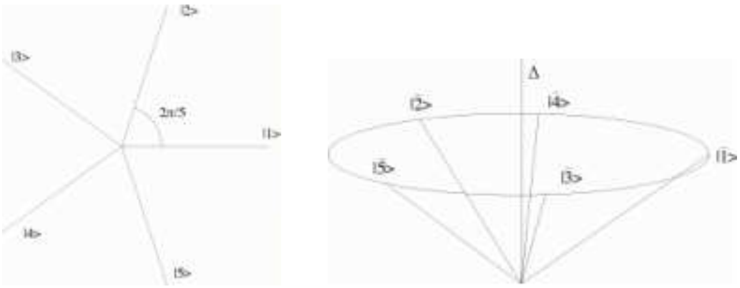

Figure 2.2: The basis vectors of the projected hyper lattice, $\Lambda^{||}$. The projections are the $M_{||}$ and $M_\perp$. In the case of $M_{||}$, the basis vectors form a regular pentagon on $E_{||}$ (in the left hand side). In the case of $M_\perp$ the basis vectors also form a regular pentagon but in a shifted plane to the Δ direction compare to $E_\perp$ (in the right hand side). (The figure was taken from the report of Michel Duneau and Denis Gratias, Introduction a la quasicristallographie)

The main steps of the Penrose tiling generating procedure is the following. One choose a finite section of the $\Lambda = \mathbb{Z}^5$: X. X includes finite number of vertexes, X_i, designated by five-dimensional vectors: $(n_1, n_2, n_3, n_4, n_5)$. One projects the five dimensional unit hypercube, C to the perpendicular subspace, $E_\perp \bigoplus \Delta$, and called the projected object, W like “window” : $W = M_\perp(C)$. W has a form of rhombic icosahedron. The n_i-s in C have the possible values: 0 or 1. In this way the only possible values for the third component of $M_\perp(C)$ are:

$$[M_\perp(n_1, n_2, n_3, n_4, n_5)]_3 = \frac{1}{\sqrt{5}} \cdot z_\perp \tag{2.7}$$

where

$$z_\perp = \sum_{i=1}^{5} n_i = 0, 1, 2, 3, 4, 5. \tag{2.8}$$

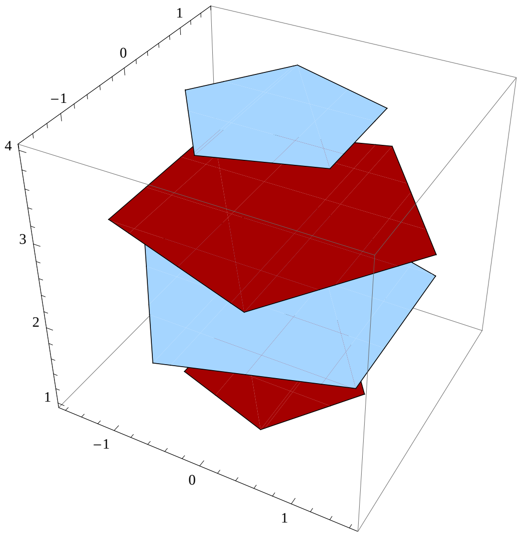

Figure 2.3: The four selection windows in perpendicular space. The selection windows $z_\perp = 1, 3$ (red pentagons in the figure) are corresponding to the "A" sublattice. The selection windows $z_\perp = 2, 4$ (blue pentagons in the figure) are corresponding to the "B" sublattice, respectively.

0 and 5 values correspond to point like objects, so there are 4 planes that should take into account: W_1, W_2, W_3 and W_4 (See Fig. 2.3). The W_i acceptance window in each of these four planes in the perpendicular subspace is a pentagon. Two such pentagons are shown in Fig.2.4 (corresponding to $z_\perp = 1$ and 2), the other two being the same upto an inversion. X_i is selected for projection if its projection in the three dimensional perpendicular space, $E_\perp \bigoplus \Delta$, belongs to the region W: if $M_\perp(X_i) \in W$ then $\exists\ P_i = M_\parallel(X_i)$. Finite samples of arbitrarily large size can be readily generated using this selection criterion, by considering large enough X volumes of Λ.

Technical note: in order to avoid ambiguities (when points fall on the edges of the selection window) one shifts $\mathbb{Z}^5$ by some arbitrary distance. This results, in particular, in tilings without an artificial center of symmetry.

The parity of the vertex as given by $z_\perp$ determines the sublattice to which it belongs. Thus, the points that project into the planes $z_\perp = 1, 3$ correspond, say, to sublattice A , while the planes $z_\perp = 2, 4$ correspond to sublattice B (See Fig. 2.3). In the infinite tiling, the two sublattices are equivalent, and the "even" and "odd" windows are the same upto an inversion.

This approach to generating the quasiperiodic tiling allows one an alternative visualization of the Penrose tiling in perpendicular space. Each family of sites of Fig.2.4 (upper) projects into a *distinct* domain, i.e. the perpendicular space representation allows us to separate sites according to their coordination number. We will use this useful property of the Penrose tiling in order to represent the complex antiferromagnetic ground state in a simpler way in Ch.4.

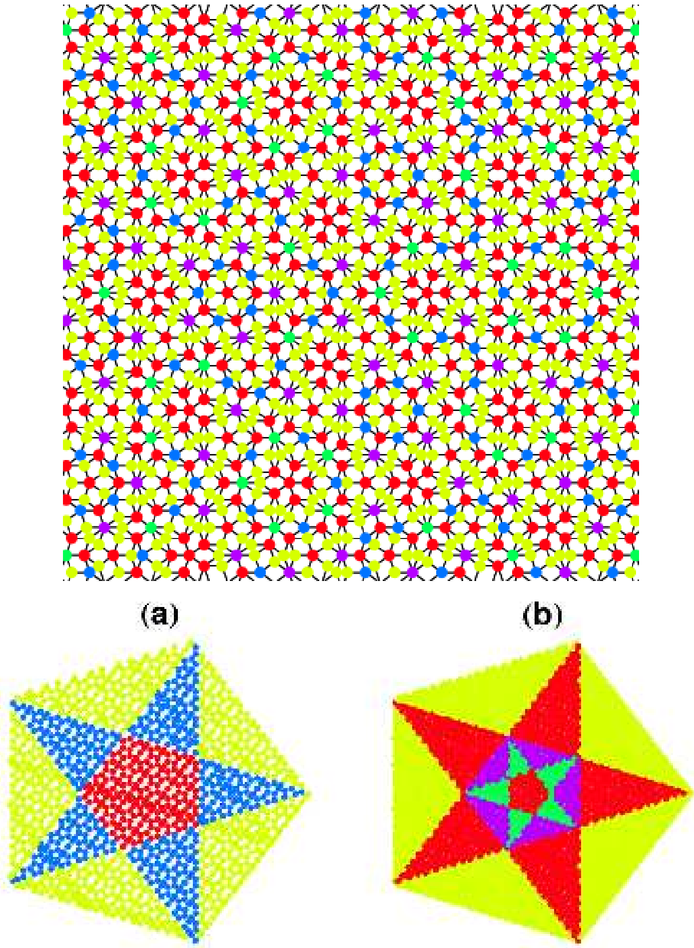

Figure 2.4: (upper) Portion of the tiling showing vertices colored differently, according to coordination number z (lower) The same tiling after projection into perpendicular space (a) the plane $z_\perp = 1$, b) the plane $z_\perp = 2$)

2.3.2 Properties of the Penrose tilings

Sublattice equivalence The Penrose tiling is bipartite. The bipartite tiling means that we could distinguish two sublattices on the tiling when all the site on one sublattice just have a kind of neighbors that are located on the another sublattice and vice versa. On the infinite tiling, the two sublattices are equivalent. It means that all kind of geometrical

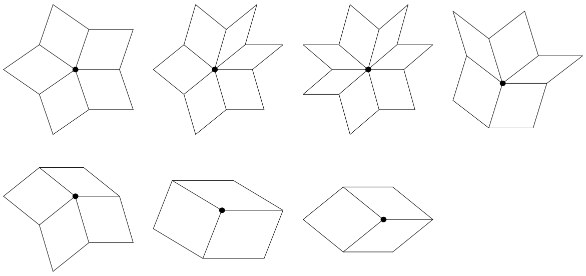

Figure 2.5: Some local environments in the Penrose tiling.

properties like e.g. frequency distribution of the coordination numbers will be exactly the same. On finite tiling the equivalence is just partially but at big system size the differencies between the two sublattices are very small.

Local isomorphism One remarkable feature of the Penrose tiling is that despite the absence of perfect translational invariance, patterns of arbitrarily large size in different regions of the tiling can be made to overlap, "local isomorphism". The mean repetition distance of a pattern of linear size R is proportional to R. This is a property that replaces the strict translational invariance of crystalline structures.

Rotational invariance Rotational invariance holds in the same "weak" sense. It means that for any given pattern, its equivalent under rotation by a multiple of $\frac{2\pi}{5}$ can be found elsewhere on the tiling.

Hierarchical symmetry The Penrose tiling possesses a hierarchical symmetry, being invariant under so-called inflation and deflation transformations (See Fig. 2.6). Inflation is a reversible operation which can be thought of as a set of decimations of vertices of the tiling, followed by a re-connection of the new vertices. The new tiling is defined on a length scale that is bigger by the factor τ. The equivalence of the old and new tilings means here that no environments are created or destroyed in the process of inflation or deflation, and that one can find an exact match between any arbitrary (finite) regions of the two tilings.

Local environments

Strictyly speaking, the Penrose tiling, like all quasiperiodic tilings, has infinitely many environments since each site is unique. However, when considering the local environments at the level of the nearest neighbors there are just 7 possibilities (upto five-fold rotations).

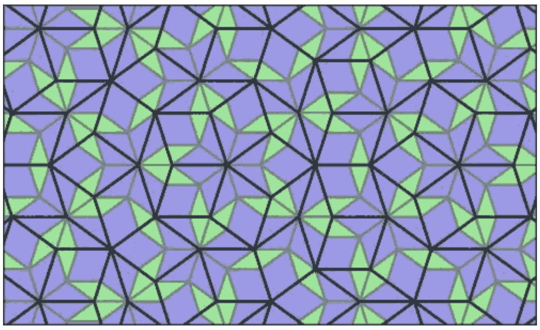

Figure 2.6: Hierarchical symmetry in the Penrose tiling. The tiling with thin light grey edges and blue and green rhombuses is the original Penrose tiling. The tiling with thick black edges is the inflated tiling by τ. The inflated tiling is also a Penrose tiling with edges τ times bigger than the original one and the vertexes of the inflated tiling are also vertexes of the original tiling. (The figure was taken from the following website: http://www.ams.org/featurecolumn/archive/penrose.html)

For convenience, we will choose to classify vertices in terms of their coordination number, z. This number will turn out to be the primary parameter in the study of local magnetic order. One can also classify the local environments by including information about the structure up to a bigger distance. For example in Ch.5. we will need to use also the average "nearest neighbor coordination number". Sites have coordination number values $3, 4, 5, 6, 7$. The average coordination number must be exactly 4 for the Penrose tiling, as can be shown easily using the Euler theorem. The frequencies of the coordination numbers can be calculated exactly in terms of the golden ratio τ. Their values are shown in Fig. 2.7, which was obtained for a finite sample of 11556 sites. This figure also shows the results for the frequencies when a site with coordination number z have a nearest neighbor with coordination number z_2. The Fig.2.5 shows seven type of local environments are present in the tiling. The first figure shows a five-fold symmetric site, which in fact comes in two varieties, the F (for football cluster) and the S (for star cluster). The properties of these sites under decimation are different. More will be said on these sites when we discuss the results for the ground state staggered magnetization distribution.

2.3.3 Approximants of the Penrose tiling

To obtain periodic approximants, one uses the oblique projection method described briefly in the Appendix. Details of the construction of the projection operators for the so-called Taylor approximant can be found by M. Duneau and M. Audier in [88], where they only considered the smallest approximant, having 36 sites. We have generalized the procedure,

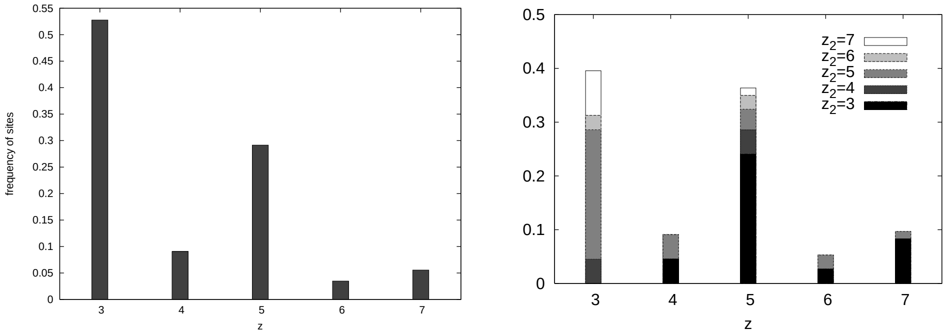

Figure 2.7: (LEFT) Frequency of the coordination number (z) for Taylor τ^6 approximant. (The system size is N=11556) (RIGHT) Frequencies of the coordination number (z_2) for the nearest neighbors that have coordination number z. (The system size is N=4414)

and obtained the following system sizes (See Fig. 2.8):

Inflations	τ	τ^2	τ^3	τ^4	τ^5	τ^6
System size	96	246	644	1686	4414	11556

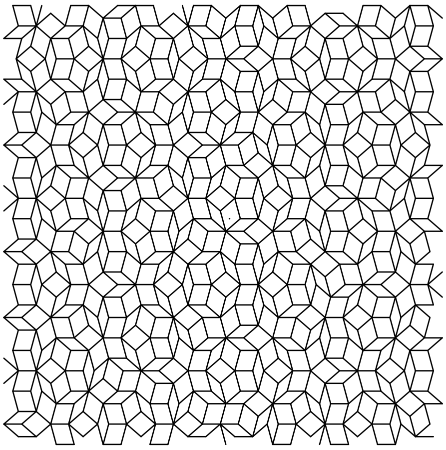

Figure 2.8: Taylor τ^3 approximant (N=644 sites)

In order to ensure that the antiferromagnetic ground state has total spin $S = 0$, one requires that sublattices A and B be of the same size. This was achieved for our finite approximants by shifting each of the four selection windows in perpendicular space, until the number of A and B sublattice points selected are equal.

The coordination numbers and the average coordination number are exactly the same like for perfect Penrose tiling. All coordination numbers are appearing with a frequency close to that expected in the perfect Penrose tiling (See Fig. 2.7). The structure locally resembles the perfect Penrose tiling. Due to the condition of periodic repetition in the plane, the approximant must be "defected" with respect to the perfect tiling at a length scale comparable to the periodic length of the approximant. As the system size increases, differences due to the long range disparities of the two structures become negligible for the physical properties that we are interested in.

Chapter 3

The T=0 Heisenberg antiferromagnet

3.1 The ground state of the 2D Heisenberg antiferromagnets

We consider the nearest-neighbor antiferromagnetic spin-$\frac{1}{2}$ Heisenberg model on bipartite tilings,

$$H = J \sum_{\langle i,j \rangle} \mathbf{S}_i \cdot \mathbf{S}_j, \quad J > 0, \tag{3.1}$$

where $\langle i, j \rangle$ are pairs of linked vertices of the tiling. We will assume that the antiferromagnetic coupling J is the same for all bonds. A tiling is bipartite when one can distinguish two sublattices - that are distinct from each other and together cover all the original tiling. The couplings J correspond to the case where all the nearest neighbors of each site are sites of the other sublattice. This property ensures that there is no frustration, i.e., if one considers classical spin variables, the ground state is one for which all bonds are "satisfied" – with all the spins on one of the sublattice are pointing in one direction and the spins on the another sublattice pointing in the opposite direction. The Mermin–Wagner-Hohenberg theorem (also known as Coleman theorem) [89, 90, 91] states that continuous symmetries cannot be spontaneously broken at finite temperature in one and two dimension. In one dimension, quantum fluctuations destroy order also at T=0. Although there is no long range order at finite temperature for two dimensional magnetic system, it is probable that the cases considered do have long range Néel order at T=0.

We recall some well-known facts: in the case of a ferromagnet ($J < 0$) the quantum and classical ground states are the same: one in which all spins point in one direction, breaking the rotational invariance of the Hamiltonian. The classical ground state for an antiferromagnet is a state when all spins point in one direction on one of the sublattices and point to the opposite direction in the other sublattice. However, it is easy to see that such a state is not an eigenstate of H, and therefore cannot be the ground state. The true ground state is known for 1D periodic chains with uniform J, for which the solution was given by Bethe in 1931 [92]. No exact result for the ground state for the 2D antiferromagnet is known, even for simple lattices like square lattice. P.W. Anderson proposed that the ground state of the square lattice could be a highly entangled ground state, referred to as "resonating valence bond" (RVB) [93]. He suggested that this state, for a square lattice of antiferromagnetically coupled copper ions might be the precursor of the high temperature superconductivity found in the layered cuprate compounds. However, several experimental [94] and numerical studies suggested that the ground state is in fact the symmetry broken Néel type state. Many approximate methods can be used to study the problem: spin wave expansion, high temperature expansion, renormalization group, Schwinger boson theory, and other methods (See [95]). In this thesis we use linear spin wave theory (LSWT), to determine the ground state and spectrum approximately. Unlike the case of lattices, here one cannot solve the problem by Fourier transforming the Hamiltonian. However, using the real space diagonalization method of White, Sparks and Ortenburger [74] Wessel and Milat developped a method that is applicable for non-periodic tilings also [75]. We will describe the main steps of this approach in this chapter.

Role of the dimension, spin quantum number and the structure

When we consider quantum spins, the ground state energy is lower than the classical value, due to the quantum fluctuations or "spin waves" in the case of periodic structures. As studies using a variety of analytical and numerical methods have shown (see review [95]), the effects of quantum fluctuations vary depending on the dimension, the spin quantum number S, and the type of structure. Quantum fluctuations are expected to become smaller as S increases, and as the dimension increases. The $S = 1/2$ is the most quantum system, and the system with big S number is considered classical like.

In a given dimension, and for simple lattices, one can ask what the local quantum fluctuations are when the coordination number is changed. In two dimensions, two examples of unfrustrated systems are the square lattice with $z = 4$ and the honeycomb lattice with $z = 3$ (see the review in [96]). Spin wave calculations, as well as Quantum Monte Carlo calculations [97, 98, 99, 100, 101] have shown that the order parameter is smaller in the $z = 3$ case. The values of the staggered magnetization, defined by the value of $m_s = |\langle S_i^z \rangle|$ as obtained by QMC calculations are $m_s^{sq} = 0.3173$ and $m_s^{hc} = 0.2788$ (with sq and hc

standing for square lattice and honeycomb lattice respectively). This is in accord with the already remarked tendency towards a less classical behavior for systems of lower dimension, hence fewer nearest neighbors.

In contrast, as pointed out in [98], when the coordination number is not constant, the local magnetization tends to be in fact larger when z is smaller. In the dice lattice, where sites can have $z = 3$ and $z = 6$, spin wave theory and QMC calculations have shown that it is the small z sites that have the larger value of the local staggered magnetization, with $m_s^{z=6} = 0.3754$ while $m_s^{z=3} = 0.4381$. This result shows the "counter-intuitive" trend towards a *less* classical behavior for sites of bigger z in structures having a distribution of z values. Other systems showing this tendency including the quasiperiodic octagonal tiling and, as shown in [102], the Penrose tiling.

3.2 The linear spin wave theory

3.2.1 Spin wave theory

Close to zero temperature the spin system coupled by exchange interaction has wavelike states called spin waves. The energy of the spin wave is quantized, and the unit energy of a spin wave called a magnon. Holstein and Primakoff introduced the spin wave theory first time for ferromagnets at 1940 [103]. Anderson [104] and Kubo showed that results could be expressed as an $1/S$ expansion (more references can be found here [95, 105, 106]).

We now describe spin wave theory, applied to Heisenberg antiferromagnet on finite, bipartite tilings with N_A site on the A- and N_B site on the B- sublattice. We consider the case where $N_A = N_B$, so that the ground state spin is expected to have S=0 (Lieb-Mattis theorem, [106]). Spin wave theory is based on the assumption that the ground state has long range order and that quantum fluctuations around the classical ground state are "small". In this case the quantum system may found near to the classical ground state in that sense that the states of the quantum system that is "closer" to classical ground state has much higher probabilities than the other states. We will specify more this "distance" later. Using this argument it seems reasonable to make a restriction in the Hilbert space and neglect that part of the Hilbert space that is far from the classical ground state. The classical ground state for antiferromagnets are "spin up" ($|\uparrow\rangle$) in the A sublattice and "spin down" ($|\downarrow\rangle$) in the sublattice B (Fig. 3.1).

(the opposite configuration is equivalent under a symmetry operation). The distance from the classical ground state can be expressed by introducing the "spin-deviation" oper-

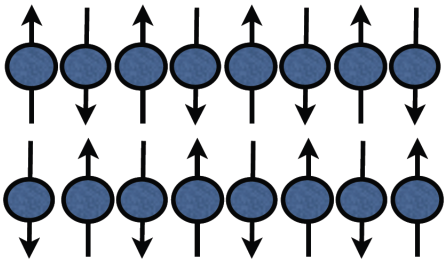

Figure 3.1: Schematic picture of the ground state in a 2D classical antiferromagnet.

ator:

$$n_i \equiv S_{cl} - \hat{S}_i^z \tag{3.2}$$

$$n_j \equiv S_{cl} + \hat{S}_j^z \tag{3.3}$$

In this representation the Hilbert space is spanned by

$$\prod_r |n_r\rangle \tag{3.4}$$

The n_r operators commute like the spin operators: $[n_i, n_j] = \delta_{i,j}$ because of the definition of the n_r and the spin commutation relation. The eigenvalues of the n_r operator are $0, 1, \ldots, 2S$. It is useful to introduce the Holstein-Primakoff boson operators in this way:

$$a^\dagger \mid n_r\rangle \equiv \sqrt{n_r + 1} \mid n_r + 1\rangle \tag{3.5}$$

$$a \mid n_r\rangle \equiv \sqrt{n_r} \mid n_r - 1\rangle \tag{3.6}$$

with a similar definition for $b^\dagger$, b in the B sublattice. n_r will be the bosonic number operator for $a^\dagger$, a if r is in the A sublattice

$$n_r = a_r^\dagger a_r \tag{3.7}$$

and the same type of relation holds for the B sublattice. These Holstein-Primakoff boson operators obey the usual bosonic commutation relations:

$$[a_r, a_{r'}^\dagger] = [b_r, b_{r'}^\dagger] = \delta_{r,r'} \tag{3.8}$$

All other pairs of $a, b, a^\dagger, b^\dagger$ operators commute with each other. Using these equations one can substitute the spin operators with the Holstein Primakoff operators in the following way:

$$\begin{aligned} S_i^z &= S - a_i^\dagger a_i, \\ S_i^+ &= \sqrt{2S}\left(1 - \frac{a_i^\dagger a_i}{2S}\right)^{1/2} a_i, \\ S_i^- &= \sqrt{2S} a_i^\dagger \left(1 - \frac{a_i^\dagger a_i}{2S}\right)^{1/2}, \end{aligned} \tag{3.9}$$

$$\begin{aligned} S_j^z &= -S + b_j^\dagger b_j, \\ S_j^+ &= \sqrt{2S} b_j^\dagger \left(1 - \frac{b_j^\dagger b_j}{2S}\right)^{1/2}, \\ S_j^- &= \sqrt{2S}\left(1 - \frac{b_j^\dagger b_j}{2S}\right)^{1/2} b_j, \end{aligned} \tag{3.10}$$

for $j \in B$.

3.2.2 Linearization

One could write the nonlinear term in (3.9, 3.10) using the series expansion of n_i, n_j respectively (3.11).

$$f_S(\hat{n}_r) = \left(1 - \frac{\hat{n}_r}{2S}\right)^{1/2} = 1 - \frac{\hat{n}_r}{4S} - \frac{\hat{n}_r^2}{16S} - \frac{\hat{n}_r^3}{32S} - \dots \tag{3.11}$$

Assuming that the expectation value of n is small enough, one can linearize the above expression, i.e. keep only the first term. This is consistent with the assumption that the ground state is close to the classical one. Studies have shown that the expectation value of the bosonic number operator are typically small when the two dimensional Heisenberg antiferromagnet is totally unfrustrated. Our system, the S=1/2 Heisenberg antiferromagnet on T=0 fulfills this requirement. The linearized Hamiltonian of the Heisenberg antiferromagnet, has now the following simple form:

$$\begin{gathered}
H_{AF} = J\sum_{\langle i,j\rangle} \mathbf{S}_i\mathbf{S}_j = \\
J\sum_{\langle i,j\rangle}[S_i^zS_j^z + S_i^xS_j^x + S_i^yS_j^y] = J\sum_{\langle i,j\rangle}[S_i^zS_j^z + \frac{1}{2}(S_i^+S_j^- + S_i^-S_j^+)] = \\
J\sum_{\langle i,j\rangle}[(S - a_i^\dagger a_i)(-S + b_j^\dagger b_j) + \\
\frac{1}{2}S(\left(1-\frac{a_i^\dagger a_i}{2S}\right)^{1/2} a_i \left(1-\frac{b_j^\dagger b_j}{2S}\right)^{1/2} b_j + a_i^\dagger \left(1-\frac{a_i^\dagger a_i}{2S}\right)^{1/2} b_j^\dagger \left(1-\frac{b_j^\dagger b_j}{2S}\right)^{1/2})] = \\
H_0 + H_1 + H_2
\end{gathered} \tag{3.12}$$

where

$$H_0 = -JS(S+1)N_b \tag{3.13}$$

$$H_1 = JS\sum_{\langle i,j\rangle}\left(a_i^\dagger a_i + b_j b_j^\dagger + a_i^\dagger b_j^\dagger + b_j a_i\right) \tag{3.14}$$

H_2 regroups the higher order terms that we neglect in the linear approximation.

3.2.3 Real space diagonalization

The Hamiltonian in the terms of bosonic operators have the following form (non-constant H_1 term):

$$\mathcal{H} = X^\dagger H X \tag{3.15}$$

where $\mathcal{H}$ is H_1/JS. H is a Hermitian complex number matrix and X including the N independent bosonic operators:

$$X = (a_1, \ldots, a_{N_A}, b_1^\dagger, \ldots, b_{N_B}^\dagger) \tag{3.16}$$

X normally includes all the 2N independent bosonic operators: $a_i, a_i^\dagger, b_j, b_j^\dagger$. However, after diagonalization in this basis we will get N doubly degenerate eigenvalues because of the equivalence of the two sublattices. We can see this in the form of the Hamiltonian (3.14) where $a_i, b_j^\dagger$ are always on the right hand side of the products and $a_i^\dagger, b_j$ are always on the left hand side. Changing the sublattices ($a \leftrightarrow b$) and considering the adjoint of the H_1 we will get the same expression. So we can reduce X to the size of N (3.16).

The method for this type of Hamiltonian is based on [74]. H is Hermitian, thus there exists a linear transformation, T, that diagonalizes H.

$$X = TX' \tag{3.17}$$

where X' is the vector of transformed bosonic operators in the case when H is diagonal. One then has

$$HT = (T^{\dagger})^{-1}\Omega_H \tag{3.18}$$

where Ω_H is the diagonal matrix. The commutation relation for $X, X^{\dagger}$ is the following:

$$[X, X^{\dagger}] = X(X^*)^T - (X^* X^T)^T = g \tag{3.19}$$

The values of g are coming from the bosonic commutation relations that's why g is diagonal and has a structure: 1 are the first N/2 elements and -1 are the second N/2. Using (3.17) the same commutation relation is:

$$[TX', X'^{\dagger}T^{\dagger}] = TX'(X'^*)^T(T^*)^T - (T^* X'^* X'^T T^T)^T = g \tag{3.20}$$

The commutation relation for $X', X'^{\dagger}$ is similarly:

$$[X', X'^{\dagger}] = X'(X'^*)^T - (X'^* X'^T)^T = g' \tag{3.21}$$

From (3.20) and (3.21):

$$Tg'T^{\dagger} = g \tag{3.22}$$

From this with a simple reorganization we get:

$$(T^{\dagger})^{-1} = g^{-1}Tg' \tag{3.23}$$

This last formula give a notable simplification for the expression (3.18) because we get an $N \times N$ eigensystem problem of gH in the place of a difficult operator equation. The eigenvalues will be $g'\Omega_H$ and the eigenvector matrix will be T where the columns of T are eigenvectors of gH:

$$(gH)T = (g'\Omega_H)T \tag{3.24}$$

The order of X'_i and the order of the column vectors of T are related. The gH matrix will have N^+ positive eigenvalues, λ_i^+ and N^- negative eigenvalues, λ_i^-. Obviously $N^+ + N^- \leq N$. Because of the structure of the gH matrix: $N^+ = N^-$. More precisely for all λ_i^+ exist a $\lambda_{i'}^- = -\lambda_i^+$. Because of this, (3.21) and (3.24), g' should have a form $\pm\delta_{ij}$ with equal number of 1 and -1. To fulfill (3.24) T should include its eigenvector in the same order as $g'\Omega_H$ includes its eigenvalue. So in this way the order of $+1$ (-1) in g' should be the same as the eigenvectors in T that are connected to positive (negative) eigenvalue. To consider the simplest case let's order the eigenvalues in decreasing sequence. In this way the positive eigenvalues come first and after the negative ones. The eigenvectors will have the same order as the connected eigenvalues have. The g' will be $(1, \ldots, 1, -1, \ldots, -1)$ and X', because of the bosonic commutation relations (3.8), will be the following:

$$X' = (\beta_1, \ldots, \beta_{N^+}, \beta^\dagger_{N^+ +1}, \ldots \beta^\dagger_{N^+ + N^-}) \tag{3.25}$$

where β_i, $\beta^\dagger_{i'}$ are bosonic operators.

3.2.4 The ground state energy and the local staggered magnetization in the linear spin wave theory

Now we derive two important quantities, the ground state energy and the local staggered magnetization in the context of the linear spin wave theory.

Calculations of the ground state expectation values in the LSWT The expectation values of β boson number are zero in the ground state. When multiplying odd number of bosonic operators the expectation value is zero as well. From these and bosonic commutation relations we get the following expressions:

$$n_i = X'^\dagger_i X'_j = 0 \qquad X'_i X'^\dagger_j = \delta_{ij} \tag{3.26}$$

These two expressions will be useful during the calculations of the ground state expectation values.

Ground state energy Using (3.14) the expression of the ground state energy is:

$$E_0 = -JS(S+1)N_b + JS \sum_{k=1}^{N_-} |\lambda^-_k|. \tag{3.27}$$

Local staggered magnetization The expression of the local staggered magnetization is:

$$\text{sublattice A} \qquad m_s(i) = \langle S_i^z \rangle = S - \langle a_i^\dagger a_i \rangle = S - \sum_{k=N^+ +1}^{N^+ + N^-} T_{ik}^* T_{ki} \tag{3.28}$$

$$\text{sublattice B} \qquad m_s(j) = \langle S_j^z \rangle = S - \langle b_j^\dagger b_j \rangle = S - \sum_{k=1}^{N^+} T_{jk} T_{kj}^* \tag{3.29}$$

for each of the sublattices A and B.

3.3 Remarks about the method

As we mentioned earlier, the diagonalization is done numerically for finite systems. Two types of boundary conditions were considered – 'open boundary condition' and the 'periodic boundary condition'. For finite pieces of the infinite quasiperiodic tiling the open boundary condition is the only possible choice. This is because such pieces cannot be fitted together to tile all of space. We considered such finite pieces, and also approximants, in order to compare the solutions found in these two situations. The open boundary condition makes the boundary sites behave differently than the bulk. The LSW wavefunctions show strong localization at the boundary that does not exist in the bulk. Only sites well within the interior of the piece were found to have the same properties of those in the approximants (which have no boundary sites). In sum, the finite size samples can give qualitatively correct results for local properties, but we need to calculate on much bigger samples. Because of this disadvantages we use periodic approximants of the perfect quasiperiodic tilings in a place of the finite size pattern of the perfect tiling.

The main requirements about the methods that one would apply to physical models on quasiperiodic tiling is that the method should be able to treat enough big system size in a reasonable CPU time. Looking at the tiling, it is evident that the quasiperiodic features of the structure will only start to appear for system sizes i.e. $N > 200$ at least, because the self-similar properties of the geometry do not exist in very samples. These requirements reduce the possible methods that we could use. The most precise numerical method for any calculation for quantum system is the Exact Diagonalization method (ED) that provide exact solution for the spectrum and wavefunction of a given Hamiltonian up to the numerical accuracy. However the state of art for the system size for ED is around $N \leq 40$, which is by far not enough for quasiperiodic systems. The Density Matrix Renormalization Group (DMRG) technique is an often used method for calculation on 1D system because of its efficiency, but is hard to implement in higher than 1D. Also the currently possible sizes that can be studied by DMRG are still too small. The Quantum Monte Carlo (QMC) method is a very powerful one for non-perturbative investigation of spin systems at finite temperature [107]. It is possible to calculate $S = 1/2$ Heisenberg antiferromagnets at least up to several thousand of sites in a reasonable amount of time. All the important physical observables that have classical analogues are possible to calculate like the magnetic structure factor and the ground state energy and get a relevant expectation values of them for $T = 0$. However, wave functions and related quantities like the inverse particpation ratio (IPR) are not possible to calculate with QMC. Therefore, to get a more complete picture, we found it necessary to study the systems by both LSWT and QMC. For more about the QMC method, the following literatures and references therein [108, 107, 109, 110].

Chapter 4

Magnon energies and wavefunctions of the Penrose tiling

4.1 Energy spectrum and density of states

The real space diagonalization procedure gives the energies $\Omega_m^{\pm}$ as well as the T-matrix (See Ch.3. and the Appendix) for each of the systems considered. The two sets of energies Ω_m^{+} and Ω_m^{-} become identical in the infinite system size limit when the two sublattices become strictly equivalent. In our case, at finite size, since the two sublattices are not identical, the numerical values are slightly different (less than a percent for the larger systems and not visible on the scale of our figures). The density of states (DOS) shows the distribution of the energy levels. We used the following expression for the density of states:

$$N(E) = \frac{1}{N} \sum_{m=1}^{N/2} \delta(E - \Omega_m^{+}) \tag{4.1}$$

The energy E is expressed in units of J. Fig.4.1 shows the density of states figure for the Taylor 6 approximant (N=11556 sites).

The integrated density of states figure is defined similarly by:

$$N(E) = \frac{2}{N} \sum_{m=1}^{N/2} \theta(E - \Omega_m^{+}) \tag{4.2}$$

Fig.4.2 shows the integrated density of states (IDOS) figure for the Penrose tiling approximant. Data for three successive Taylor approximants has been plotted, with the points in red corresponding to the largest system size, points in green to the medium size, and

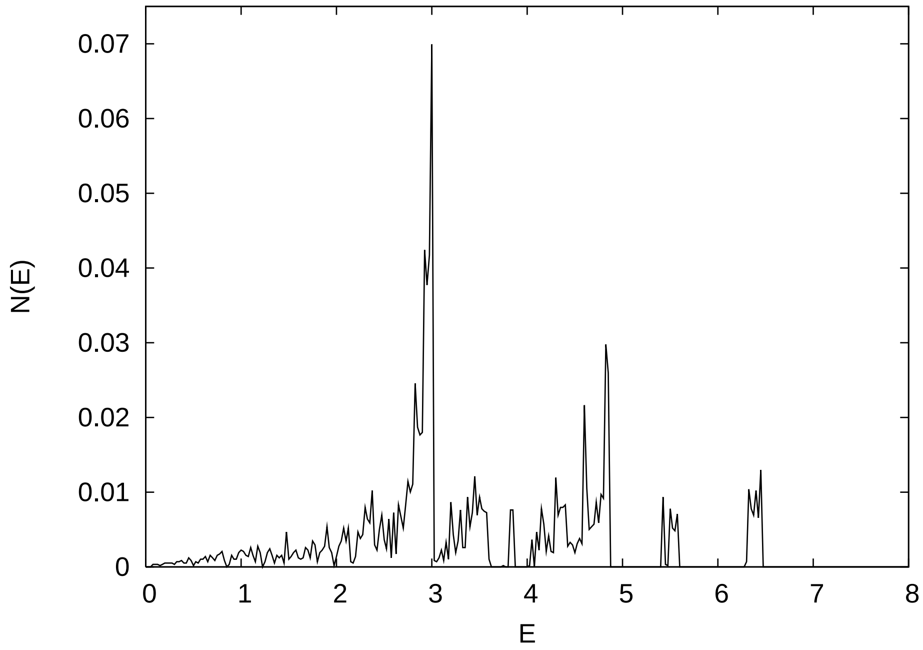

Figure 4.1: Density of states calculated for the Taylor 6 approximant (N=11556 sites).

points in blue to the smallest size. The DOS is only slightly size dependent, as seen by the overlapping of the three sets of data points. The salient features of the figure are the several groups of closely spaced energy levels, the main gaps, which are stable with increasing system size, and a discrete jump at the energy $E = 3$, corresponding to a macroscopic degeneracy, as discussed below. One sees the characteristic fluctuating form of the density of states typical of quasiperiodic systems.

Low energy region

The lowest energies correspond to states of relatively extended character, as we will discuss below. As shown in Fig.4.3 the low energy part of the IDOS can be fitted to a power law of the energy, $N(E) \sim E^2$ reflecting a linear dispersion of the magnon modes in this region of the spectrum. Fitting to a form $N(E) = E^2/(8\pi c^2)$ gives a sound velocity on the Penrose tiling of $c = 1.08J$. It is interesting to compare this result for c with the corresponding values on the square lattice and the octagonal tiling, both having in common with the Penrose tiling the same value of the classical energy per spin $E_{cl}/N = -2JS^2$. This value is $c_{sq} = 2\sqrt{2}JSa \approx 1.41J$ on the square lattice (for edge length $a = 1$ and $S = 1/2$). On the octagonal tiling, our estimated value is $c_{octa} \approx 1.3J$, in agreement with Milat and

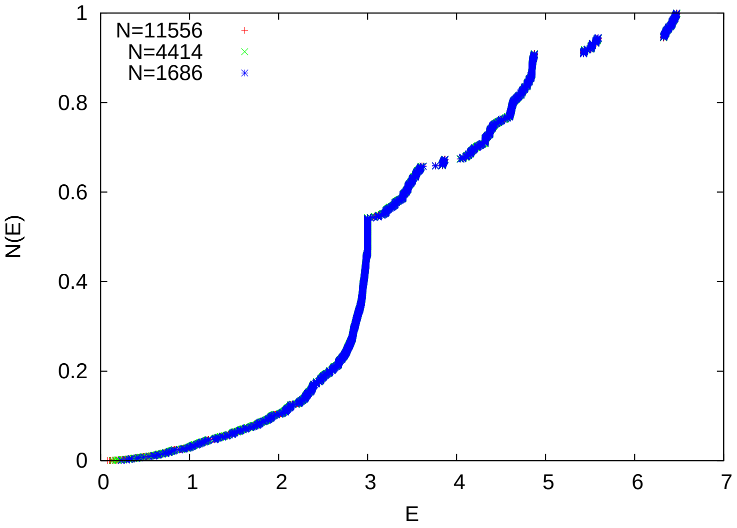

Figure 4.2: Integrated density of states (IDOS) figures for three system sizes (N=1686 (blue), 4414 (green), 11556 (red)). From the high overlapping of the curves one suggest a small size dependence for the IDOS.

Wessel's IDOS data [75]. To resume, an acoustic-type dispersion relation is obeyed at long wavelengths, with a spin wave velocity which is smaller than in the octagonal tiling, which is in turn smaller than the value on the square lattice. This is presumably due to the fact that the density of sites is largest in the Penrose systems, followed by the octagonal tiling, and finally the square lattice.

Exactly degenerate states

E=3J is a degenerate eigenvalue caused by the special structure of the Penrose tiling. The fraction of degenerate eigenvalues (degeneracy divided by the system size) scales with $N^{-1/2}$ (Fig. 4.4 (left)). The infinite system size limit from the fit is 0.0807. The degenerate wavefunctions are localized on 3-fold sites and form closed loops. The smallest such loops occur around "star-like" five-fold star structures (Fig. 4.4 (right)).

Minibands at higher energy

At higher energy (3 < E(J) < 5) the wavefunctions are centered primarily on the 4 and mostly on 5-fold sites. At highest energy one can distinguish several groups of energies separated by gaps. The highest energy bands around the values $E \approx 5.4$ and $E \approx 6.4$, correspond to wavefunctions that are localized on the 6- and 7-fold sites, as will be shown shortly.

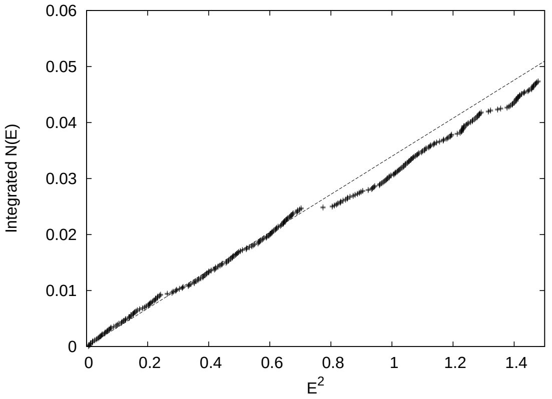

Figure 4.3: Fit of the low energy part of the integrated density of states figure of the Taylor 6 approximant (N=11556 sites). From the gradient of the curve the magnon speed is determinable.

4.2 Weight fractions and partial densities of states

We now discuss the magnon wavefunctions and their spatial characteristics for the different parts of the energy spectrum. We first show that the coordination number plays an important role in determining the extent to which a site participates in the wavefunction for a given eigenmode, $\psi^{(E)}$. This can be seen from Figs.4.5a) through e), which show the weight fractions as a function of the energy, for each of the five values of the coordination number z. The weight fractions were defined as

$$f_n = \sum_{i \in F_n} |\psi_i^{(E)}|^2 / \sum_j |\psi_j^{(E)}|^2 \tag{4.3}$$

where the $F_3, F_4, ...$ are the subsets of sites whose coordination numbers are $z = 3, \ldots, 7$. Only sites of sublattice A are considered (a similar calculation for sublattice B gives the same results).

The plots of the weight fractions show a number of interesting properties of the magnon modes. In particular, they show the preponderance of certain types of site in the different energy bands. Thus it is clear from Fig.4.5 e) that the highest energies correspond to states having a large amplitude on sites of $z = 7$. The highest energy band has a width of about 0.16 and is centred around $E = 6.4$. Fig.4.7a) represents one such state in real space, with sites are shown with varying intensity depending on the square of the wavefunction amplitude. The lightest spots are those on sites with $z = 7$. The group of states next highest in energy are those involving $z = 6$ sites, and correspond to energies in the range

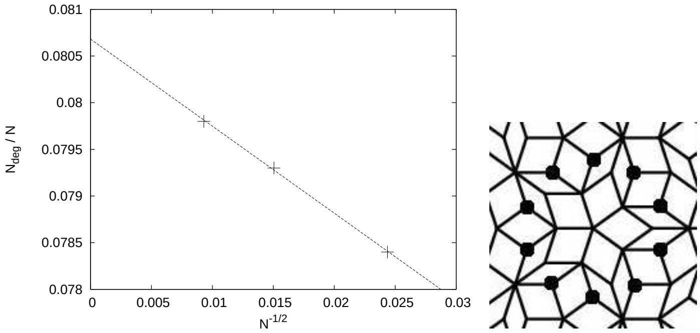

Figure 4.4: (LEFT) Finite size scaling of the number of the degenerate eigenmodes (with eigenvalues: +3, -3) per the system size. The values are seems to fit to the line of $N^{-1/2}$. The extrapolated value to the thermodynamic limit is 0.0807. (RIGHT) Schematic wavefunction intensity picture, with degenerate eigenvalue = 3. The wavefunction is localized around a five-fold star.

$5.43 < E < 5.49$. These states have a smaller dispersion than the states in the topmost group of energies, reflecting the fact that the six-fold sites are significantly fewer in number than the seven-fold sites.

The middle band of energies, $3 < E < 5$ arises for states involving sites of $z = 5$, which account for about 30% of the sites. From Fig.4.5c) one sees that the four-fold sites are particularly important in a narrow range of energy within this band. As seen by the large step in $N(E)$ at $E = 3$, a large number of degenerate states occur at this energy. This is due to wavefunctions that have their entire support on the $z = 3$ sites. These are string-like states forming closed loops – on length scales that range from a small ring (around the footballs, for example) to being as large as the system size. A linear combination of such degenerate states is shown in Fig.4.7b).

The lowest energy states , for $E \leq 1$, are the closest to extended states. The wavefunction amplitudes depend less sensitively on the site coordination number. The fact that all sites participate is best seen from Fig.4.6, where we have plotted for each of the five z-values the average probability for a given site, f_n/N_n, (where N_n is the number of sites of the nth family), as a function of the energy E. Clearly, for the low energy states, the probability amplitude is nonzero for all the values of z. On the other hand, not all of the sites participate in a given wavefunction, and for a given energy the wavefunction is mainly confined to a set of disconnected patches. The lower the energy, the larger the patches where the wavefunction is non-zero. Figs.4.7c) and d) show the states corresponding to two energies. For $E = 0.8887$ there are many closely spaced small patches. As the energy gets smaller, the patches of non-zero amplitude get larger, along with the spacing between them,

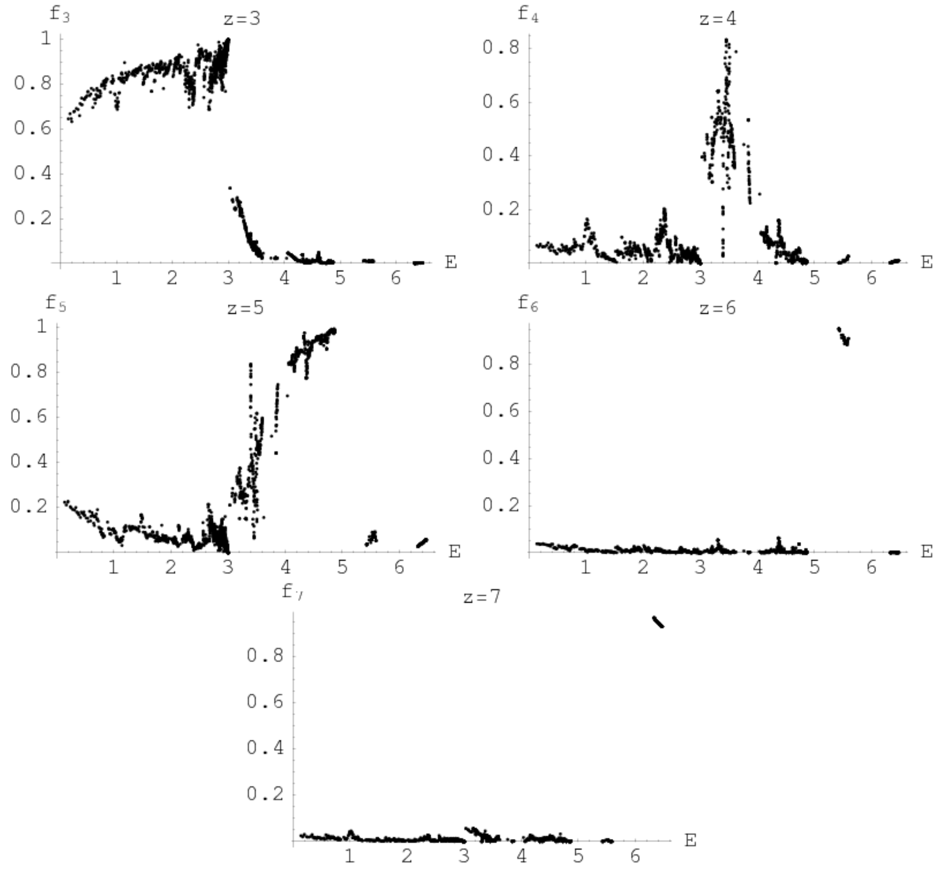

Figure 4.5: a) - e) Weight fractions f_n (see text) as a function of E for $z = n$ ($n = 3, \ldots, 7$), as computed for the Taylor 5 approximant (N=4414 sites).

and at energy $E = 0.1692$, for example, the wave function has two large patches (which are of course repeated periodically, due to the boundary conditions). To resume, the dimension of the support of eigenstates decreases as a function of the energy, from two at small E, to one at $E = 3$, tending to zero at the highest energies.

4.3 Perpendicular space representation of the wavefunctions

In the preceding section we alluded to the fact that the perpendicular space representation of the Penrose tiling is a useful way to see the environment-dependence of spatially varying quantities. We now illustrate this in the case of the four wavefunctions shown in Figs.4.7 represented in perpendicular space by Figs.4.8. Each vertex of the Taylor approximant is mapped (see the Appendix for more details) onto a point $\{x_\perp, y_\perp, z_\perp\}$. We show the projection in the plane $z_\perp = 2$ of the Penrose tiling, with regions shaded according to the local

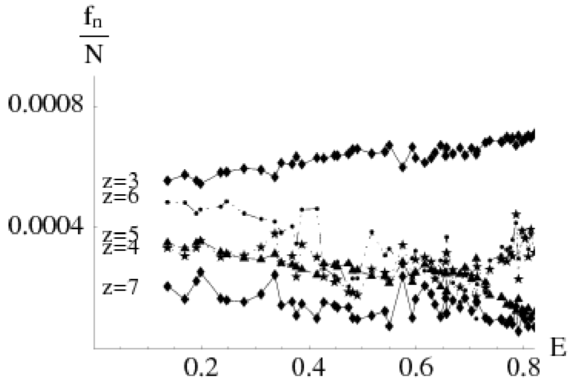

Figure 4.6: The average value of $\psi_i(E)^2$ per site for each z plotted against E for states in the bottom of the spectrum.

value of the wavefunction. Specifically, the intensity of the spot at site i is proportional to the value of $|\psi_i(E)|^2$. Fig.4.8a) shows the perpendicular space projection for the wavefunction corresponding to the energy $E = 6.469$. The spots of maximum intensity are in the region that corresponds to $z = 7$. Fig.4.8b) shows, similarly, that the wavefunction for $E = 3$ is non-zero for the region corresponding to $z = 3$. The last two figures show wavefunctions that are delocalized in perpendicular space (ie, all sites are involved, regardless of the value of the coordination number).

4.4 Participation ratio and multifractal analysis.

We present the results for the inverse participation ratio (IPR), defined by

$$P^{-1}(E) = \frac{\sum_j |\psi_j(E)|^4}{(\sum_j |\psi_j(E)|^2)^2}$$

Recall that as N is increased, the inverse participation ratio decreases as $1/N$ for truly extended states, tends to a constant for localized states, and has an intermediate behavior scaling as $N^{-\beta}$ for the so-called critical states. This quantity has been much studied in the case of tight-binding models for electrons in disordered systems, in particular, close to or at the critical disorder for the metal-insulator transition (MIT) [111]. For electrons in the Penrose and Ammann-Kramer-Neri tilings, Grimm et al [112] have found a distribution of values of β ranging between 0.5 and 1. Turning now to our spin problem, Fig.4.9 shows the results for $\log(P^{-1}(E))$ versus E for the Taylor approximants for three different sizes. (Note: the values have been calculated separately for each sublattice, according to the corresponding sector $\Omega^{\pm}$ of the eigenvalue spectrum). The fluctuations in the IPR tend to

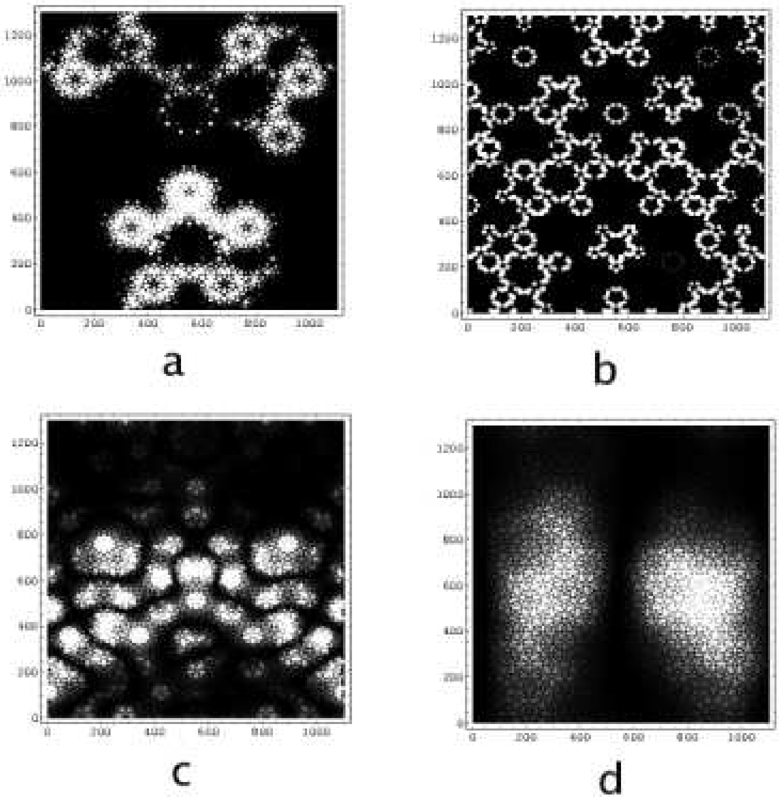

Figure 4.7: Intensity plots representing the probability $\psi_i(E)^2$ for different energies E (the lighter shade corresponds to a higher probability): a) $E = 6.469$ b) $E = 3.0000$ c) $E = 0.8887$ d) $E = 0.1692$. The solutions have been obtained for the Taylor 5 approximant (N=4414 sites).

be quite large from one energy to the next, (note that the figure is plotted on the logarithmic scale), however, the smoothed IPR is an increasing function of E over most of the energy spectrum. There is a noticeable dip in some of the IPR values as the energy approaches the value $E \approx 3$, and at $E = 3$ the value of the IPR does not reflect the spatial extent of the eigenstates, because of the mixing of the macroscopically degenerate states at this energy.

Fig.4.9 shows the most marked size dependence in the region of small energies, in accord with our earlier observation that states relatively delocalized at low energy. At high energies, the states are more localized, and the size dependence is accordingly smaller.

As a general remark, results for the IPR should be treated with precaution, in the case of quasiperiodic systems, as compared with disordered ones. In the latter case, away from the MIT, the decay of the wavefunctions is typically exponential, and degenerate states are

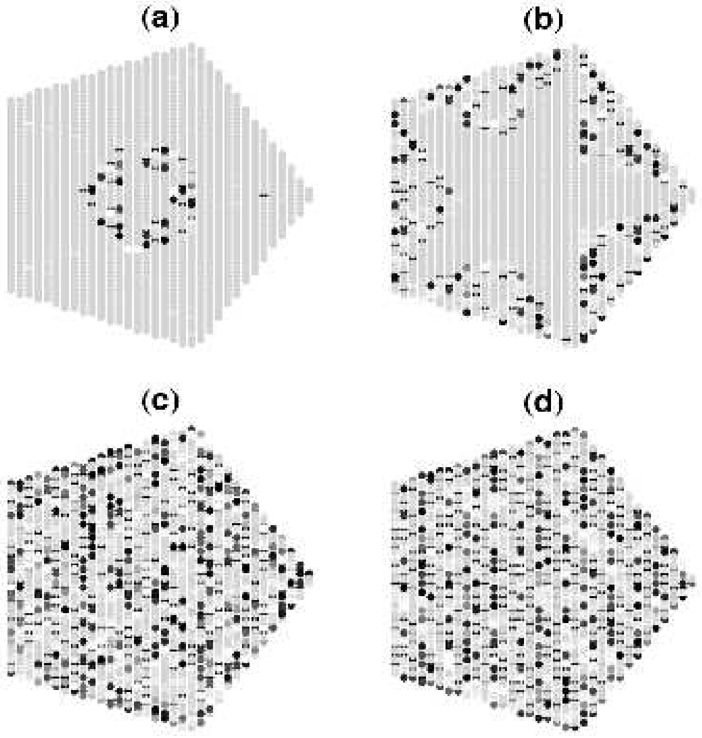

Figure 4.8: Intensity plots in perpendicular space representing the probability $\psi_i(E)^2$ for different energies E (a darker shade corresponds to a higher probability): a) $E = 6.469$ b) $E = 3.0000$ c) $E = 0.8887$ d) $E = 0.1692$

unlikely. In the quasicrystal, exactly degenerate states do occur at special values of the energy ($E = 3$ here), which leads to an IPR value equal to that of extended states, due to linear combinations of localized states. Our results for the IPR, taken together with the preceding analyses of the wavefunctions, indicate that wavefunctions can be considered to be two dimensional, and power law extended in the lower end of the spectrum. The average value of β , found by fitting the form $P^{-1}(E) \propto N^{-\beta}$ found in this region is $\beta \approx 0.9 \pm 0.1$.

4.4.1 Multifractal analysis.

The multifractal character of wavefunctions for quasiperiodic Hamiltonians can be considered to be established in a number of one dimensional models [113] and strongly indicated in a number of two dimensional systems including the tight-binding model for electrons [112] and the phonon problem [114], and even in three dimensional models [115]. The scaling properties of the wavefunctions can be investigated by calculating the $f(\alpha)$ spectrum.

For computation of the multifractal spectrum, we use the standard box-counting proce-

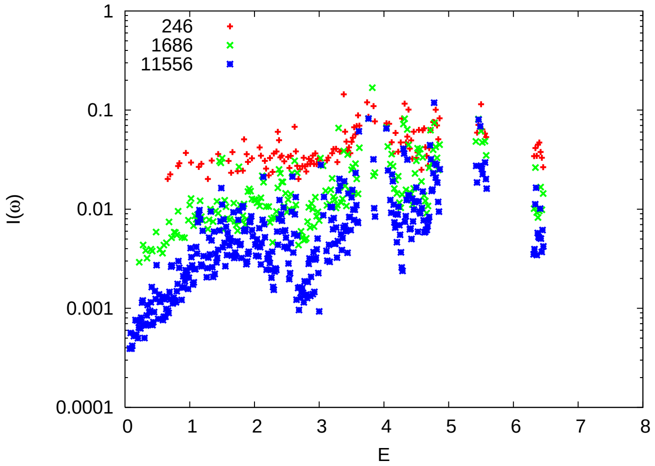

Figure 4.9: Inverse participation ratio (IPR) plotted on a log scale as a function of the energy for three successive Taylor approximants

dure, [116, 117] first dividing the system of L^d sites into $N_l = (L/l)^d$ boxes of linear size l and determining the box probability of the wave function in the i box by $\mu_i(l) = \sum_n |\psi_{kn}|^2$, where the summation is restricted to sites within that box and ψ_{kn} denotes the amplitude of an eigenstate with energy E_k at site n. The normalized qth moments of this probability $\mu_i(q,l) = \mu_i^q(l)/\sum_{j=1}^{N_l} \mu_j^q(l)$ constitute a measure. From this, the Lipschitz-Hölder exponent or singularity strength can be obtained, [118]

$$\alpha_q(L) = \lim_{\delta \to 0} \frac{\sum_{i=1}^{N_l} \mu_i(q,l) \ln \mu_i(1,l)}{\ln \delta} , \tag{4.4}$$

as well as the corresponding fractal dimension

$$f(\alpha_q(L)) = \lim_{\delta \to 0} \frac{\sum_{i=1}^{N_l} \mu_i(q,l) \ln \mu_i(q,l)}{\ln \delta} , \tag{4.5}$$

which yields the characteristic singularity spectrum $f(\alpha)$ in a parametric representation. In Eqs. (4.4) and (4.5), $\delta = l/L$ denotes the ratio of the box sizes and the system size. If the qth moments of the measure counted in all boxes are proportional to a power τ_q of the box size, $\langle \sum_{i=1}^{N_l} \mu_i^q(l) \rangle \propto l^{-\tau_q}$, multifractal behavior may be derived. The $f(\alpha)$ spectrum and the mass exponent τ_q are related by a symmetric Legendre transformation, $f(\alpha) = \alpha q - \tau_q$, with $\alpha = d\tau_q/dq$ and $q = df(\alpha)/d\alpha$.

As $f(\alpha)$ depends on system size, and our system sizes are rather small, an extrapolation to infinite size is not without risk. Nevertheless, we have investigated the multifractal

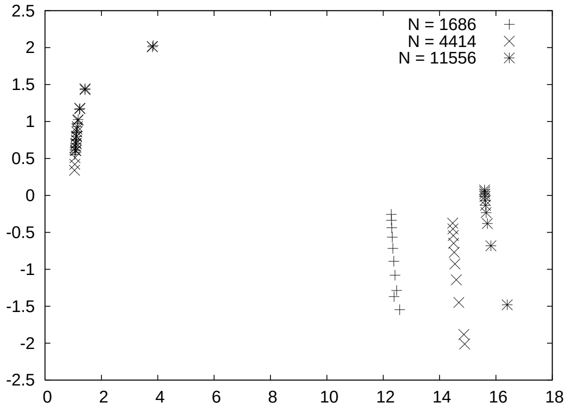

Figure 4.10: Some examples of $f(\alpha)$ plots for small energy eigenstates in three Taylor approximants. The curves have a maximum at $\alpha(0) \sim 4$ with $f[\alpha(0)] = 2.0$. The information dimension for these wavefunctions is $\alpha_1 \approx 1.5$. Probably because of finite size effects the curves are not continuous.

scaling properties in the low energy end of the spectrum, where the states are extended, and have an patchy structure, with peaks and valleys spaced farther and farther apart as energy decreases – see Figs. 4.7c) and d). We find evidence for a nontrivial distribution of exponents in the limit of large system sizes. Fig.4.10 shows the results of a multifractal analysis of two representative low energy states for three system sizes. The shape is a priori size dependent, and state dependent as well. One can nevertheless distinguish a smooth functional form of the $f(\alpha)$ function in each case. The curves have a maximum at $\alpha(0) \sim 4$ with $f[\alpha(0)] = 2.0$, which is the dimension of the support – also called similarity dimension – of the wavefunction of this system. The so-called information dimension for these wavefunctions is given by $f[\alpha(1)] = \alpha_1$ (also known as D_1). It corresponds to the intersection of the $f(\alpha)$ curve and a straight line of slope 1 and we find $\alpha_1 \approx 1.5$. For comparison, for a three dimensional system at the metal-insulator transition (MIT) the critical values have been found to be [119] $\alpha(0) = 4$ and $\alpha(1) = 2$.

Chapter 5

Ground state properties of the local staggered magnetization on the Penrose tiling

5.1 Ground state energy

The ground state energy per site has the following expression (see Ch.3.):

$$E_0 \cdot N = -JS(S+1)N_b + JS\sum_{k=1}^{N_-} |\lambda_k^-|. \tag{5.1}$$

We considered the ground state energy (GSE) in the periodic approximants of size N ranging from 246 to 11556 (Taylor τ^2 ,..., τ^6 approximants). The results of ground state energy for each approximants are given below:

N	246	644	1686	4414	11556
GSE	-0.643726	-0.643216	-0.643062	-0.643012	-0.642995

For periodic Heisenberg model, one expects based on general arguments that the ground state energy will scale with $N^{-3/2}$ [120, 98]. We found a good agreement for our quasiperiodic system to this scaling form also, and were able thus to obtain the ground state energy for the thermodynamic limit. We find that it is obeyed on the average in the Taylor approximants, with deviations that get smaller as size increases. Our extrapolation to infinite

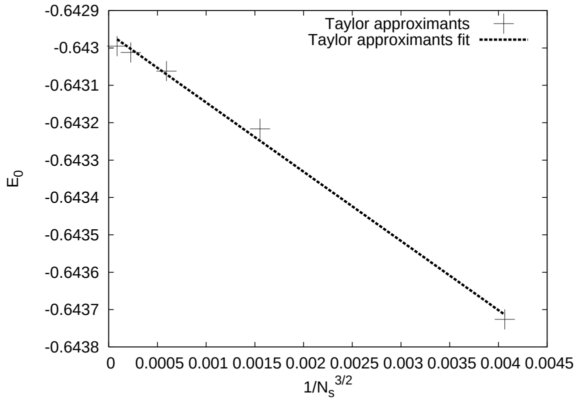

Figure 5.1: Finite size scaling for ground state energy to the Taylor approximants (N=246, . . . , 11556)

system size gives an asymptotic value:

$$E_0 = -0.643(0) \pm 0.0001$$

The possible causes of the deviations:

As can be seen in the figure, the deviations from the scaling form occur with positive and with negative sign, depending on system size. This may be due to fact that successive Taylor approximants are obtained by different shear projections. Since each approximant was obtained by a different rational section in five dimensional space, the distribution of local environments differ from sample to sample. The approximants seem to have local environments and z-values first tending towards one distribution, and then another when the size is increased. The ground state energy must of course depend on the distribution of local environments. In [121] it was argued that the ground state energy of the tiling may depend in a simple way on moments of the variable zS. It was proposed in [122, 121] that the ground state energy may be expressed as an series in the moments of z^{-1}:

$$E_0 = -\frac{1}{2} zS^2 [1 + 4\zeta_1(1/zS) + 4\zeta_2(1/zS)^2] \tag{5.2}$$

The first moment is just the average value of $z = 4$ in all cases. However $\langle (zS)^{-1} \rangle$ varies from sample to sample, and this possibly accounts for the sign and magnitude of the observed deviations from the straight line power law behavior.

5.2 Staggered local magnetizations

The absolute value of the local staggered magnetizations in the ground state are given in linear spin wave theory by the following expressions for the sites of the A and the B sublattices:

$$\begin{aligned} m_s(i) &= |\langle S_i^z \rangle| = S - \sum_{k > \frac{N}{2}-1} |A_{ik}|^2 \qquad (i \leq N/2) \\ m_s(j) &= |\langle S_j^z \rangle| = S - \sum_{k \leq \frac{N}{2}-1} |B_{jk}|^2 \qquad (j > N/2) \end{aligned} \tag{5.3}$$

5.2.1 Spatial dependence of the staggered magnetization

Fig.5.2 represents how local magnetizations vary in space on a portion of the Penrose tiling. The color of the circles around each vertex varies from red (small magnetization) to blue (high magnetization). Next to this a grayscale figure shows the symmetries of the spatial distribution of the local staggered magnetism. In the right hand side of the figure I black lines are drawn to indicate a self similar structure formation where we can distinguish four self similar levels. The defects of the Taylor approximants (with repsect to the perfect tiling) give an upper limit for the size of self similar structure formation. At length scale comparable to the system size, no self similar formation is possible because of the required translational invariance of the Taylor approximants.

The scaling of the average staggered magnetizations may be seen in Fig.5.3(left), where we show the values of the staggered magnetization in 5 different approximants and sizes ($N = 246$ to $N = 11556$). The average magnetizations appears to scale with $N^{-1/2}$, as for periodic systems [120, 98]. In Fig.5.3, right hand side, the scaling of the average site magnetization for sites with the same coordination number is presented. These values also seem to scale with $N^{-1/2}$. The fit give an expectation value for the average staggered magnetization to the thermodynamic limit with the following value:

$$\overline{m_s} = 0.356(6)$$

The expectation values for the average local staggered magnetization for sites of a given coordination number ”z”:

z	3	4	5	6	7
$\overline{m_s}$	0.382	0.329	0.326	0.340	0.335

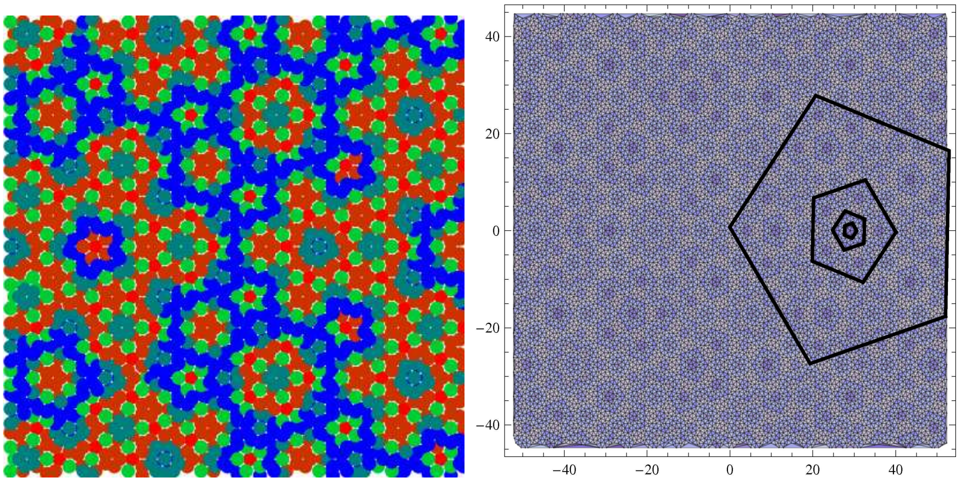

Figure 5.2: (LEFT) A portion of a Taylor approximant with vertices colored according to the value of the onsite magnetization (magnetization values : red (small), green (intermediate) blue (highest)) (RIGHT) Real space distribution of the staggered magnetization on the Taylor 6 (N=11556) approximant of the Penrose tiling. Linearly interpolated values where the larger values shown lighter. The 4 pentagons show 4 levels of self-similar structure in the magnetization values.

The lowest values of staggered magnetization are found on a certain subset of $z = 5$ sites. The largest values are found on the low coordination sites of $z = 3$.

5.2.2 Coordination number dependence and distribution

As the figure shows, the local staggered magnetization depends, to a first approximation, on the coordination number, although the distribution is very wide for certain values of z - the width arises because of differences in next-nearest neighbor environment. Fig.5.4 indicates the average values and the standard deviations of the staggered magnetization on sites with a given coordination number. The dashed line are LSWT data, the continuous line are QMC data. The figure shows that Quantum Monte Carlo gives a narrower spread of the magnetization. Linear spin wave theory clearly overestimates the fluctuations from average behavior, giving a too high value for $z = 3$ and too low values for higher values of z. Finite Penrose samples gave the same results as the periodic approximants when the sites on the free boundary layer were excluded from the analysis. In the Fig.5.5 we show all the local staggered magnetization values depending from the coordination number. The magnetization values are shifted depending on the approximant and on the system size (from left to the right: Taylor τ^2 ,..., τ^6 approximants, N=246, 644, 1686, 4414, 11556). We observe strong size dependence in the figure. The Fig.5.6 presents the separated staggered

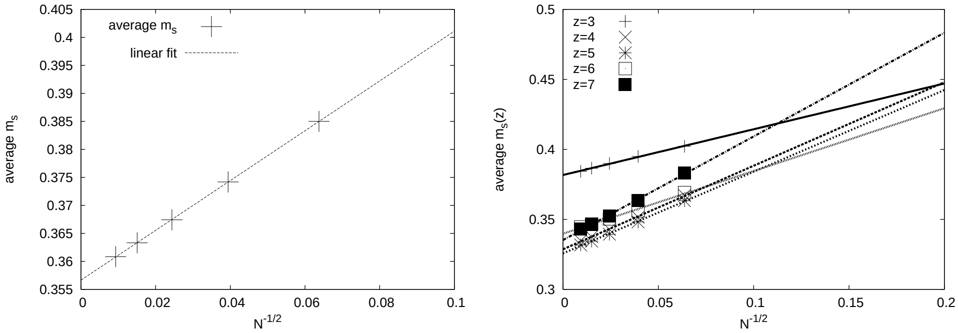

Figure 5.3: (left) Finite size scaling of the average local staggered magnetization (lines indicate fit to power law $N^{-1/2}$). (right) Finite size scaling of the average local staggered magnetization for each coordination number z

magnetization distribution function for different coordination numbers. The figures use the same scale to make comparisons easier. There is a continuum of values, as expected for a quasiperiodic structure, but also some pronounced peaks, corresponding to specific local configurations. Some of the main observations will be described further below in the next section. The distribution function for 3-fold sites include three well separated peaks that belongs to three different type of 3-fold sites. The 4-fold sites show low dispersion and a high peak around staggered magnetization value 0.33. The magnetization values of the 5-fold sites are distributed widely and it is possible to distinguish at least three main peaks. The sites with the lowest magnetization values (peak is around 0.304) correspond to the 5-fold sites at the center of a football shape cluster (called F-sites in [102]). The well separated highest magnetization values (peak is around 0.378) correspond to the 5-fold sites that are at the centers of a star shape cluster (called S sites in [102]). The magnetization values between these two that have the biggest population (with two peaks at 0.331 and 0.338) and they correspond to the non-regular 5-fold sites. The 6-fold sites show a much less population and a relatively high peak (0.344) that show low dispersion for 6-fold sites. The 7-fold sites have bigger population than the six fold sites and show a much more dispersive feature (the mean value is around 0.346).

5.2.3 Perpendicular space representation of the ground state staggered magnetization

We show, in Fig.5.7, two sets of projections onto perpendicular space of the vertices of the Taylor approximants. The corresponding onsite magnetizations, as calculated for the tiling in real physical space, are colored according to their values as previously, in Fig.5.2. The

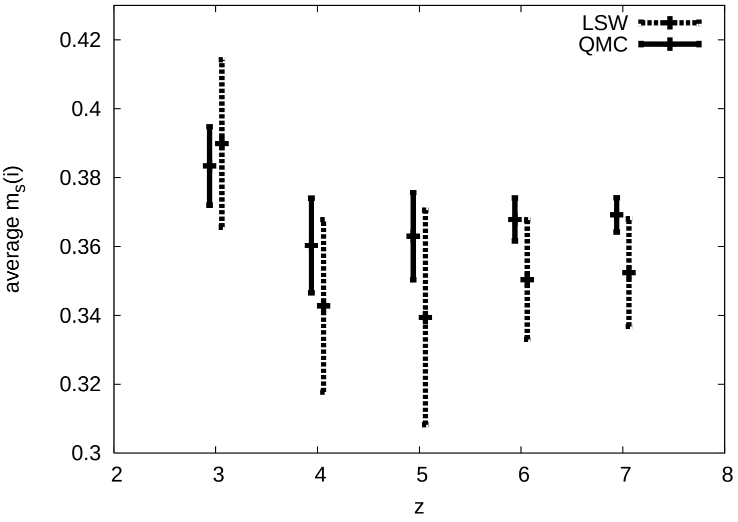

Figure 5.4: Averages and standard deviations of the local staggered magnetization as a function of z for N=1686 (LSW theory (dashed line) QMC (continuous line))

figures show that, as expected, the domain corresponding to each coordination number has a distinct color. The colors are not absolutely uniform since no two sites are identical. Self-similar patterns can be investigated using this type of representation, however our system sizes are not large enough to enable a quantitative analysis of self-similarity in the ground state. Fig.5.7a shows the domain corresponding to the F sites, as a central star-shaped region, which has the lowest m_{si} values. The S sites project into a different star-shaped domain shown in Fig. 5.7b, and can be seen to have a bigger value of the staggered local magnetization. We mentioned that the Penrose tiling is invariant under the inflation transformation where edge lengths are expanded by a factor τ. If there is any self similarity of the ground state under an inflation operation, it can be perceived on the perpendicular space magnetization map as pairs of similar patterns in regions which are related via an inflation transformation.

5.3 Predictions using the Heisenberg star model

We first consider the effects of variation of the number of nearest neighbors using a simple Heisenberg star model (Fig. 5.8), as first outlined in [123]. A central spin $\mathbf{S_0}$ is coupled to z neighbors $\mathbf{S_j}$. The exact set of eigenenergies and eigenstates of an isolated cluster are easy to find. In particular, the ground state will be rotationally invariant in spin space. However, we are interested in a situation where the cluster is embedded in an antiferromagnetic

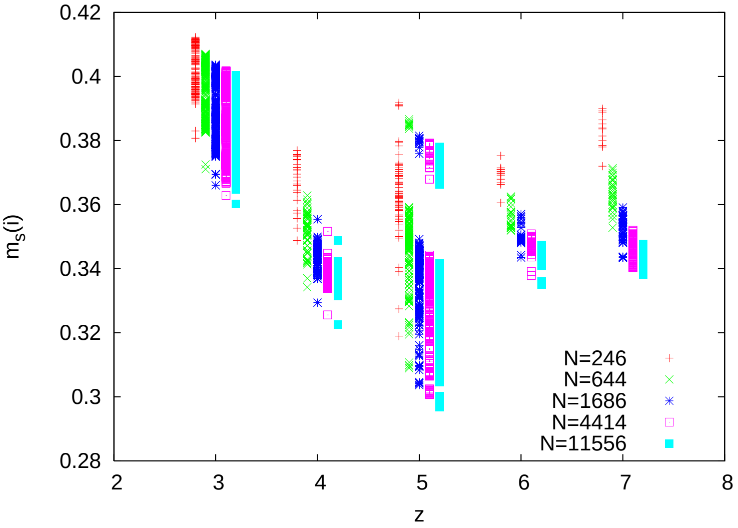

Figure 5.5: Local staggered magnetization dependence on the coordination number for different Taylor approximants. The system sizes we considered are (from left to the right) N=246, 644, 1686, 4414, 11556 (Taylor τ^2 ,. . . , τ^6 approximants).

background. Assuming therefore an initial symmetry broken state of the finite cluster, one can apply the methods of spin wave theory to this case. The Hamiltonian $H = \sum_{j=1}^{z} J\mathbf{S}_0.\mathbf{S}_j$, can be expanded in boson operators a (describing the center site spin fluctuations) and b_j, as described in [123]. The corresponding magnetizations are respectively $m_0 = S - \delta m_0$ and $m_j = S - \delta m_j$ where (for $z > 1$)

$$\begin{aligned} \delta m_0 &= 1/(z-1) \\ \delta m_j &= 1/z(z-1) \end{aligned} \tag{5.4}$$

Quantum fluctuations of the center spin are thus larger than those of the outer spins. This is a consequence of the fact that in such clusters, the classical term, which creates an onsite potential $V_0 \propto z$, thereby discouraging boson formation on the center site, is dominated by the transverse terms. These terms in $a^\dagger b_j^\dagger$ create and annihilate boson pairs on each link, leading to quantum fluctuations being greater for sites with more neighbors.

This cluster model is a first approximation and contradictory to our results. In order to explain the multiple peaks in the values of m_{si} seen numerically for a given z, we must take into account longer range structural details.

We consider therefore the two tier Heisenberg star shown in Fig.5.8, as described in

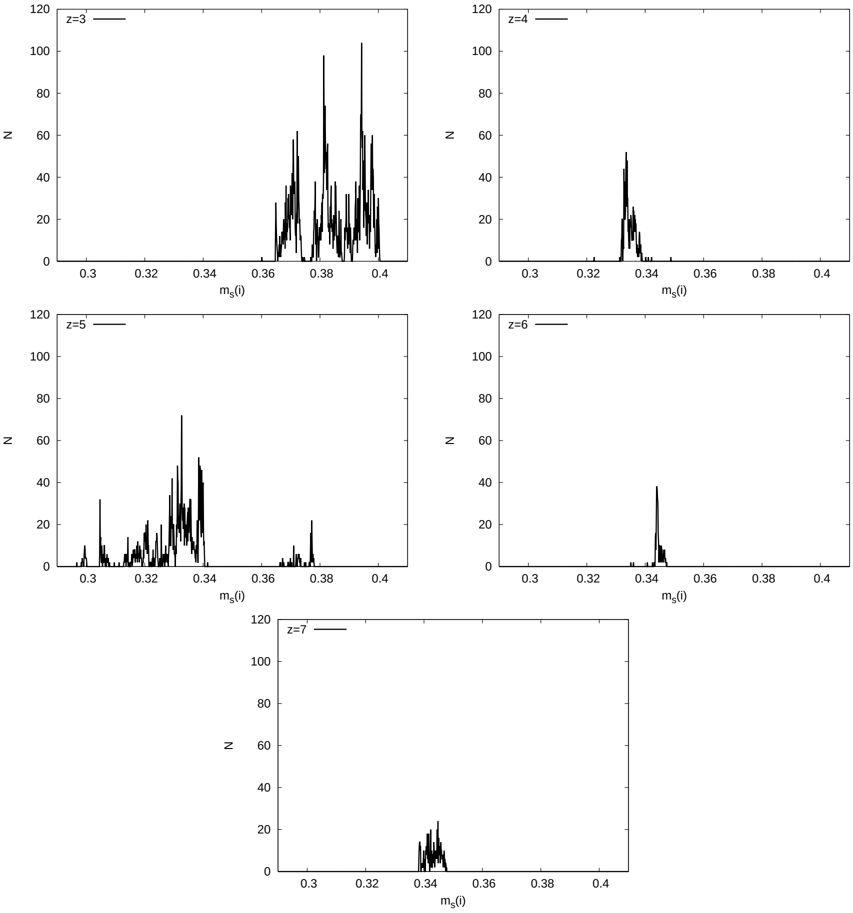

Figure 5.6: Probability distribution of the local staggered magnetizations for the five different values of the coordination number. The figures use the same scale for easier comparison. System size considered is N=11556.

[102]. The Hamiltonian of this cluster is linearized after introducing Holstein-Primakoff operators a_0, a_i, $(i = 1, ..., zz')$ and b_j, $(j = 1, .., z)$ The resulting expression for the center site magnetization is

$$
\begin{aligned}
m_s(z,z') &= \frac{1}{2} - \frac{z f_1^2(z,z')}{f_2^2(z,z') - z f_1^2(z,z') - 4z'}, && (5.5)\\
\text{where} \qquad f_{1(2)} &= -z' \pm (2 - z + \sqrt{4 - 4z + (z+z')^2}) && (5.6)
\end{aligned}
$$

The main new feature of $m_s(z,z')$ is its non-monotonicity. m is shown plotted against z for various values of z' in Fig.5.9. For each of the curves of fixed z', a shallow minimum is seen to occur for values $z \sim 1 + z'$, that is, when the coordination numbers of the center

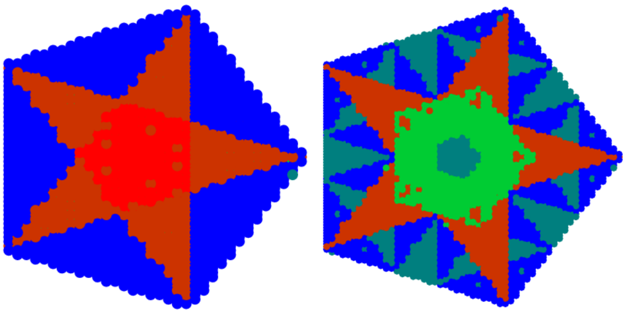

Figure 5.7: (Color online) Fig.5.2 represented in perpendicular space. Two planes are shown (corresponding to $z_\perp = 1, 2$) (magnetization values : red (small), green (intermediate) blue (highest))

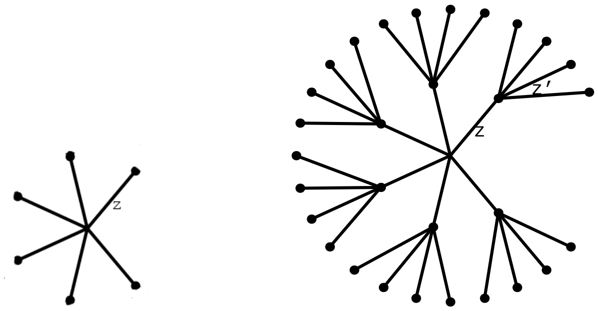

Figure 5.8: (left) Heisenberg-star cluster: a central spin is coupled with z mutually uncoupled neighbors. (right) Two-tier Heisenberg star

site and the nearest neighbors are matched. Using numerical linear spin wave calculations we get the following surfaces for the staggered magnetization in the case of different z and z' value: Fig. 5.9 right hand side.

z	z' (corresponding frequency)	$m_s(z, z')$
3	4 (31%),4.33 (27%), 4.67 (42%)	0.41, 0.42, 0.43
4	3 (100%)	0.36
5	2 (14%),2.4 - 3.2 (81%), 4 (5%)	0.26, 0.35, 0.41
6	3 (100%)	0.37
7	2.3 (100%)	0.33

Table 5.3: Values of z' (and their frequencies) for each coordination z and the predicted values of $m(z, z')$ using Eq.5.5

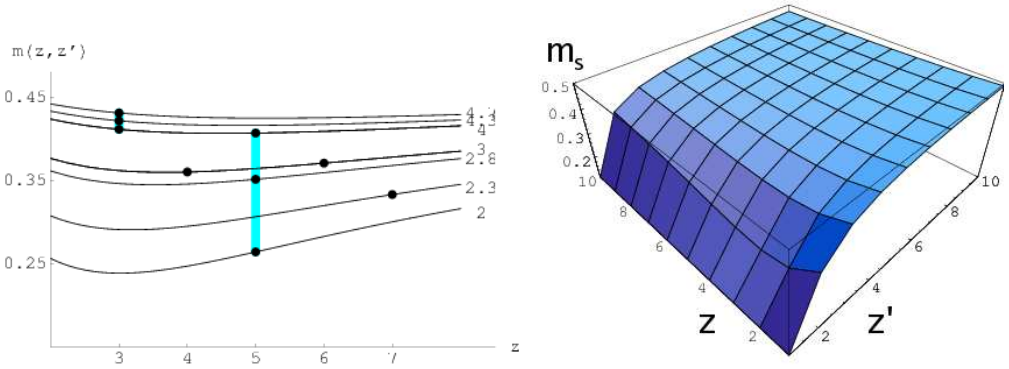

Figure 5.9: (LEFT) $m_s(z, z')$ plotted as a function of z (see text) for selected values of z' (as given in Table 1). (RIGHT) $m_s(z, z')$ presented as a surface on the z, z' plane (numerical LSW calculation).

Returning to the Penrose tiling and approximants thereof, we use the number of next nearest neighbor bonds $n(z)$ to classify sites of a given z. The $z = 3$ sites can be classified in three subgroups, depending on z', as shown in Table 5.3. To take the case of $z = 3$, three values corresponding to three main local configurations are found, to be compared with the three principal peaks of the z=3 curve in Fig.5.6. The substructures arise due to differences in the third nearest and further neighbor configurations. The number of next nearest neighbors also serves to distinguish between the different $z = 5$ sites, of which there are three main types as we mentioned in the section before. There are two varieties of five-fold symmetric sites: the football-shaped clusters (F) and the star-shaped clusters (S). The former have $z' = 2$, while the latter have $z' = 4$. The F sites thus have the smallest onsite magnetizations and the S-sites, on the contrary, have the largest onsite magnetization. The remaining (most frequently occurring) $z = 5$ sites which do not have a local five-fold symmetry have intermediate values of z'. These results agree well with the staggered magnetization distribution shows in Fig.5.6. For other z values, like z=4, 6 and 7 the staggered magnetization distribution function have non zero values in a narrow range of values. This is a consequence of the fact that there is only z' value for these families of sites.

5.4 Spin-spin correlation

The spin-spin correlation is defined by

$$C_{ij} = \langle \hat{S}_i \hat{S}_j \rangle \tag{5.7}$$

where i, j are site indexes. We have investigated the spin-spin correlation in the Penrose tiling versus the distance between the sites. In the Fig. 5.10 we show the spin-spin correlations of a given site, having $z = 3$ and placed at the origin, and the other 3-fold sites (red dots) and the 4, 5, 6, 7 -fold sites (black dots).

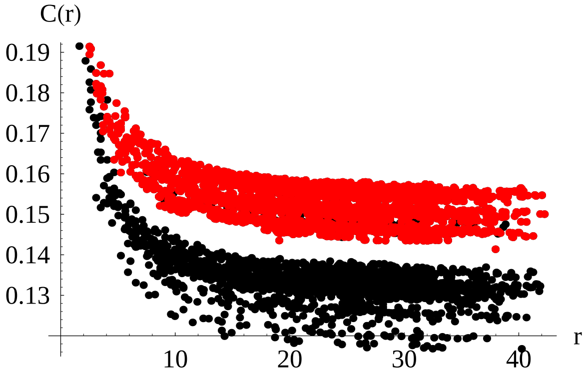

Figure 5.10: Spin-spin correlation as a function of distance between a fixed $z = 3$ site placed at the origin and all the other sites of the tiling. The red dots correspond to the correlation function with other z=3 sites. The black dots are the correlations with all of the other sites.

The figure shows that the spin-spin correlation is not one but several inverse distance laws, with asymptotic values that depend on the magnetization distribution. For a given family of sites, the correlation decreases as (5.8).

$$C(r) \sim \frac{1}{r} \tag{5.8}$$

where $r = |r_i - r_j|$. The asymptotic values of each of the parallel curves is explained as follows. In linear spin wave theory the longitudinal spin-spin correlation is independent of the distance between the spins. This is seen from the following equation between longitudinal correlation and staggered local magnetism:

$$\begin{gathered}\langle S_i^z S_j^z \rangle = \langle (S - a_i^\dagger a_i)(-S + b_j^\dagger b_j) \rangle = \\ -S^2 + S\langle a_i^\dagger a_i \rangle + S\langle b_j^\dagger b_j \rangle + O(2) = \\ \langle S - a_i^\dagger a_i \rangle \langle -S + b_j^\dagger b_j \rangle + O(2) = \\ \langle S_i^z \rangle \langle S_j^z \rangle + O(2)\end{gathered} \tag{5.9}$$

In spin wave theory, therefore, the longitudinal part of $C(r)$ does not depend on the distance r. The (5.8) dependence comes from the transverse part.

5.5 Static Structure factor

Most of our knowledge of the structure of condensed matter comes from diffraction experiments. An incident radiation such as X-rays, neutrons, electrons is scattered from the set of atoms in the solid. Because of the long range ordered arrangement of the atoms, the interference of waves scattered from different atoms can cause a distinct pattern of constructive and destructive interference to form. This is the diffraction pattern caused by the crystal. Neutron scattering investigations of condensed matter have the advantage that neutrons have no electric charge and can penetrate better in the bulk material. As neutrons have spin, they can also provide information on the distribution of magnetic moments in the solid. In the elastic scattering of neutrons there is no energy transfer between the scattering neutron and the atoms of the target, and all neutron energies are included in the experiment. This experiment measures the integrated or static structure factor, defined by :

$$S_\alpha(\mathbf{k}) = \int_{-\infty}^{\infty} d\omega S_\alpha(\mathbf{k},\omega) = \sum_{i,j=1}^{N_s} e^{i\mathbf{k}\cdot(\mathbf{r}_i-\mathbf{r}_j)}\langle S_i^\alpha S_j^\alpha\rangle \tag{5.10}$$

where α is either x, y or z. In the nonmagnetic phase, the so-called nuclear structure factor is given by a similar definition, without the spin components S_z. The static structure factor is related to the observed Bragg peak intensities, by:

$$I(\mathbf{k}) = S(\mathbf{k})S(\mathbf{k})^* \tag{5.11}$$

5.5.1 Static longitudinal structure factor

The static longitudinal ($\alpha = z$) structure factor has the following form, using (5.9) in (5.10) :

$$\sum_{i,j=1}^{N_s} e^{i\mathbf{k}\cdot(\mathbf{r}_i-\mathbf{r}_j)}\langle S_i^z S_i^z\rangle = (\sum_{i=1}^{N_s} e^{i\mathbf{k}\cdot\mathbf{r}(i)}\langle S_i^z\rangle)(\sum_{j=1}^{N_s} e^{-i\mathbf{k}\cdot\mathbf{r}(j)}\langle S_j^z\rangle) + C$$

that is equal to the square of the Fourier transform of the magnetization, $(\sum_{i=1}^{N_s} e^{i\mathbf{k}\cdot\mathbf{r}(i)}\langle S_i^z\rangle)^2$. We have investigated the static longitudinal magnetic and nuclear structure factors numerically for a finite number of $\mathbf{k}$ vectors. The highest intensity peaks are shown in the Fig. 5.11.

One sees on comparing the nucelar and the magnetic structure factors, that they have a similar appearance, with the peaks of one lying in between the peaks of the other, in such a way that if the two patterns are overlapped, there are twice as many peaks as in the original structure factor. This leads to our hypothesis that peaks can be indexed

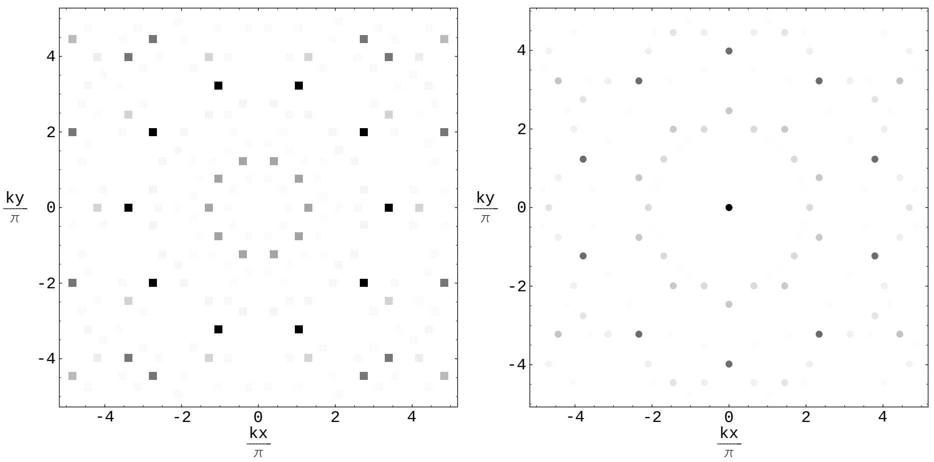

Figure 5.11: (left) Intensity plot of the static longitudinal magnetic structure factor $S^{\|}(\mathbf{k})$ for the $S = 1/2$ Heisenberg antiferromagnet on the 4414 sites approximant of the Penrose tiling. The relative intensity is denoted by a linear gray scale ranging between zero (white) and one (black). (right) Intensity plot of the Fourier transform of the coordinates of the sites (nuclear diffraction pattern) on the 4414 sites approximant of the Penrose tiling. The relative intensity is denoted by a linear gray scale ranging between zero (white) and one (black).

using four indices which are integers for non-magnetic peaks and integer or half-integer for the magnetic peaks. A simple one-dimensional case was forst considered to explain this effect by R. Lifshitz [124], and another example of this effect was also observed for the octagonal tiling [75]. In the magnetic phase, the peaks at half integer indices arise due to the doubling in size of the antiferromagnetic unit cell in five dimensions. This, coupled with the extinctions in the structure factor due to the multiplicity of each unit cell, then leads [124] to the observed ”shifting” or ”displacement” of the magnetic peaks with respect to the nonmagnetic ones. To compare the magnetic and nuclear structure factor we made a figure (Fig. 5.12) where the two structure factors are normalized with respect to their maximum intensity.

Since large single quasicrystals are difficult to obtain, powder diffraction patterns are more commonly measured in experiments. The crystallites within such a powder sample can have arbitrary different orientations, one measures a structure factor where the intensities are averaged over the solid angle, to obtain $S(|\mathbf{k}|)$. We calculated this powder pattern for the approximants of the Penrose tiling (Fig. 5.13).

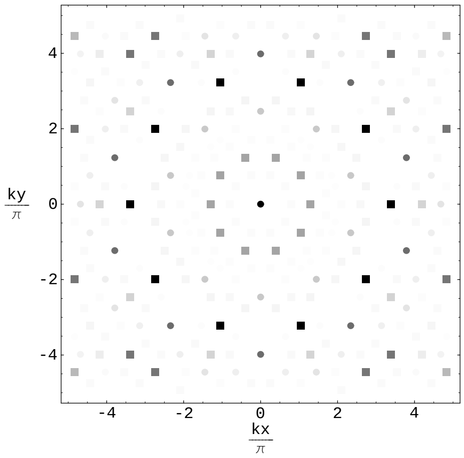

Figure 5.12: Combination of the two intensity plots above in the same intensity plot. The relative intensity is denoted by a linear gray scale ranging between zero (white) and one (black).

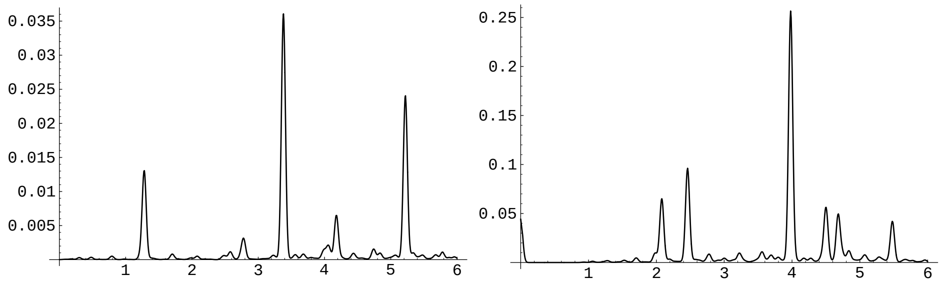

Figure 5.13: (left) Radial intensity plot of the static longitudinal magnetic structure factor $S^{\|}(\mathbf{k})$ for the $S = 1/2$ Heisenberg antiferromagnet on the 4414 sites approximant of the Penrose tiling. (right) Radial intensity plot of the Fourier transform of the coordinates of sites on the N=4414 approximant. In both figures the x axes is $\mid \mathbf{k} \mid$ and y axes are the intensities of the peaks of the static longitudinal structure factors: $S_z(\mathbf{k})$.

Chapter 6

Magnetic properties of the phason disordered Penrose tiling

6.1 Introduction

In this chapter we discuss the effects of phason disorder in the ground state of the Penrose tiling antiferromagnet. Phason disorder is of solely geometrical type. A single phason flip operation is a purely local change of tiling geometry, involving a discrete jump of a single site to a new position. The perfect tiling can be disordered by randomly choosing sites for such phason flips, each of which reorganizes the structure locally, in the vicinity of the flipped site. This type of disorder is strongly constrained, as one does not modify the basic building blocks of the structure, but only the way they are put together.

In practice, most of the structurally refined quasicrystals are assumed to be basically deterministic, with phonon and phason disorder at finite temperatures [125]. However, one can also consider essentially random quasiperiodic structures, which could be preferred for entropic reasons by the system [126]. Theoretical models for the Heisenberg Hamiltonian [102, 127] make a number of simplifications in that they consider a) two dimensions, b) all sites to be occupied by spins and c) interactions to be restricted to adjacent spins. Lastly, earlier studies did not take into account disorder, which is almost certainly present in the experimentally studied alloys. To describe the real systems it would be necessary to dilute the lattice, introducing disorder and frustration, and this is outside the scope of the current study, which focuses on disorder effects only. The question raised here would concern the T=0 magnetic properties of such structures, in which the phason disorder is "frozen-in".

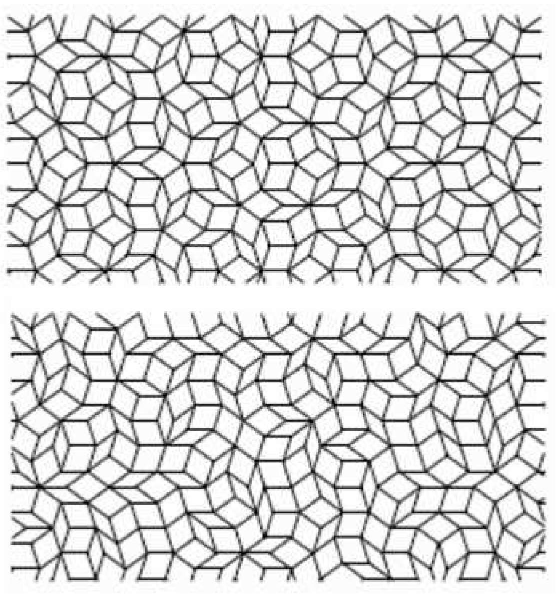

Figure 6.1: Samples of a perfect tiling (up) and a randomized tiling (down).

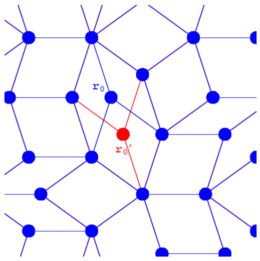

Figure 6.2: A single phason flip showing the original (r_0) and final positions (r_0'). The original sites and bonds are shown in blue and the new site and new bonds in red.

6.1.1 Definition of the phason flip

We term "phason flip" the process by which a 3-fold site hops to a new allowed – in terms of the tile configurations – position. The old site disappears, as do the three bonds linking it to its neighbors, while a new 3-fold site appears on a different sublattice (See Fig. 6.2 in the left hand side). If $\vec{r_0}$ and $\vec{r_j}$ ($j = 1, 2, 3$) are the position vectors of the central site and its three neighbors, the new position of the central site is given by:

$$\vec{r'_0} = \sum_{j=1}^{3}(\vec{r_j} - \vec{r_0}) - \vec{r_0}. \tag{6.1}$$

Three new bonds appear linking to the new site to the sites at the positions $\vec{r_j}$ $(j = 4, 5, 6)$ where $j = 4, 5, 6$ are the sites that has exactly two neighbors from the group of sites of $j = 1, 2, 3$. The new coordination numbers of all of the seven sites are involved are computed. The new connectivity matrix is determined and the set of sites available for the next phason flip is determined. The locations of the phason flips are chosen randomly using uniform distribution. This process is executed by a loop until a N_{ph} number of flips. A phason flip thus gives a local reshuffling of bonds involving the six sites surrounding a 3-fold site, and it shifts the central site from sublattice A to sublattice B. To maintain a ground state of total spin zero, our random selection of phason flip choose the sites alternately from A and B sublattice and restricted N_{ph} to be even. This method of disordering the sample ensures that:

- The average coordination number is exactly 4
- The two sublattices remain equal in size
- The randomization generates samples of fixed phason strain. [1]

Fig. 6.1 shows a portion of a perfect (deterministic) tiling on the left, and a typical example of a disordered tiling on the right.

6.1.2 Definition of the phason disorder

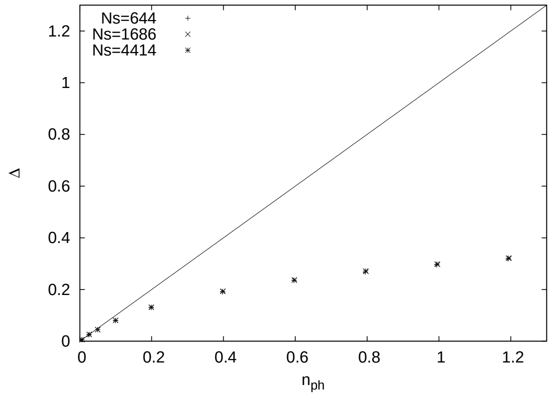

Figure 6.3: Dependence of the disorder (Δ) from the phason flip normalized with the system size (n_{ph}).

---

[1] In the 'cut and project' scheme (See Ch.2.) the deviations from perfect order correspond to fluctuations in which the orientation of the cut in the 5D hyperspace remains constant.

For a given total number of flips N_{ph}, we calculate the degree of disorder Δ by performing an average over the overlap distance between the perfect sample and the disordered samples. The overlap distance will be the number of shifted sites. This number normalized with the system size will be the degree of disorder (Δ) for a given number of phason flips (See Fig. 6.3). The system sizes that we considered are N=644, 1686 and 4414 spins. The number of realizations considered are 100 for N=644, 1686 and 10 for N=4414. The number of realizations was chosen so as to ensure a reasonable standard deviation for the data in a reachable CPU time. There is an upper limit to the number of phason flips we are able to introduce in the tilings, which occurs due to the fact that our starting point is a periodic approximant. Such tilings are necessarily defected with respect to a perfect Penrose tiling, and as a result inacceptable configurations are observed to appear after a number of flips slightly greater than N ($\approx$ 3.1 N).

6.2 Geometrical properties of the randomized tiling

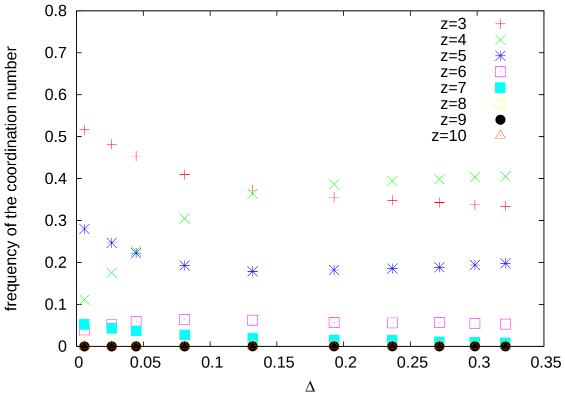

Figure 6.4: Dependence of the coordination number distribution from the degree of disorder (Δ). On the y axis: the ratio of the number of the sites with a given coordination number per the system size in the case of certain degree of disorder. (The system size we considered is N=4414.)

Phason flips clearly lead to a modification of local environments on the tiling, and in particular, the apparition of new local environments that were not present in the original tiling such as 8-fold, 9-fold and 10-fold vertices. These vertices are also possible to appear using the two building blocks of the Penrose tiling, the “thick” and the “thin” rhombuses but in the Penrose tiling they are not appearing because of the matching rules of the Penrose tiling. During randomization these constraints could not make effect so all the possible vertices will appear. Furthermore, finite-sized regions of perfect five-fold rotational symmetry progressively disappear with increasing degree of disorder. We have made a study of the evolution of the frequency of sites of each coordination number $z = 3, ..., 10$ as a function of the degree of disorder. As shown in Fig. 6.4, the disorder clearly increase the number of 4-fold sites at the expense of the 3-fold and the 5-fold sites. The original perfect structure has a large number of 3-fold and 5-fold sites, included by the most common cluster found in the original perfect Penrose tiling, the "football"-shape five-fold stars. These clusters are destroyed progressively by disorder. The evolution of coordination numbers will be significant for the qualitative analysis that we will present below for the staggered magnetization.

6.3 Energy spectrum and wavefunctions

We consider the antiferromagnetic spin-$\frac{1}{2}$ Heisenberg model:

$$H = J \sum_{\langle i,j \rangle} \mathbf{S}_i \cdot \mathbf{S}_j \tag{6.2}$$

as in the earlier chapters, for spins situated on vertices of the tiling. Nearest-neighbor interactions are antiferromagnetic, $J > 0$, and act between pairs of sites that are linked by an edge. Since all the structures we consider are constructed from the same set of tiles – the thick and the thin rhombus – these antiferromagnets are unfrustrated. Therefore we are able to use the linear spin wave theory also for these tilings at $T = 0$. The LSWT calculation is carried out in the same way as for perfect tiling and as we described at Ch.3. Using the results of these calculations now we describe the energy spectrum and eigenmodes for the randomized tilings. The density of states, defined by $\rho(E) = \sum_\mu \delta(E - \omega_\mu)$, is shown in Fig. 6.5. The figure shows that the principal effects of the disorder on the density of states are to progressively smoothen the fluctuations and fill in the gaps. The low energy tail is linear, and can be fitted to give a spin wave velocity that *increases* with phason disorder as shown in Fig. 6.6. This indicates that spin wave propagation is facilitated by the phason disorder, in analogy with the problem of quantum diffusion of electrons in the tight binding model in quasiperiodic tilings [88]. In addition, the localized states at $E = 3$ disappear progressively. These states arise, as shown in [127] on closed loops of 3-fold sites. Such loops are eliminated when a phason flip occurs on the one of the participating sites.

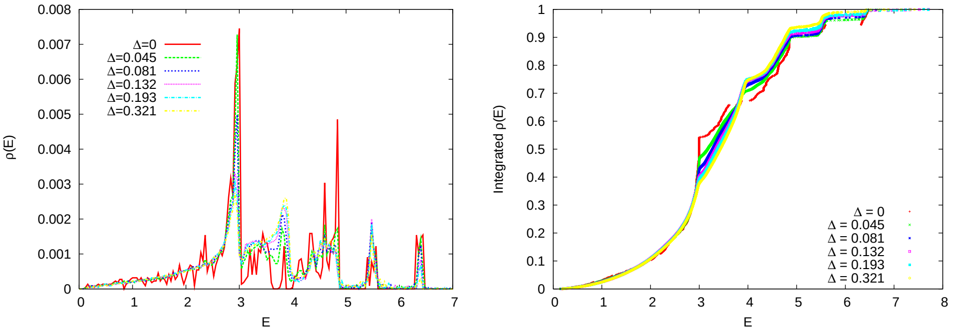

Figure 6.5: (left) Density of states $\rho(E)$ plotted against the degree of disorder. (right) Integrated density of states plotted against the degree of disorder. The system size we considered in both cases is N=4414.

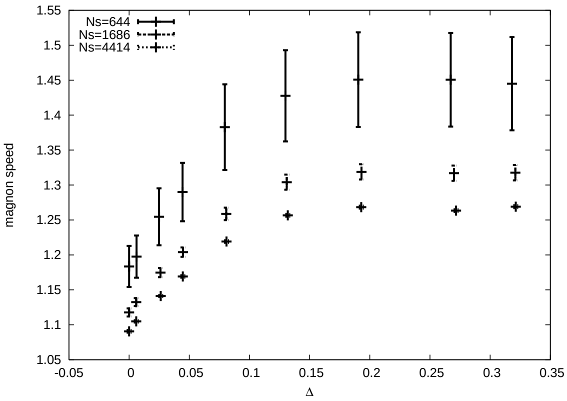

Figure 6.6: Effective spin wave velocity as a function of disorder. The system sizes we considered are N=644, 1686, 4414.

6.4 Local staggered magnetisation on the disordered Penrose tiling

6.4.1 Ground state energy

The average ground state energy per site $e_0 = E_0/N$ is shown as a function of disorder in Fig. 6.7 for three different system sizes. e_0 decreases exponentially with Δ. The smooth curve shows a fit to the form $e_0 = e_{dis} + (e_{perf} - e_{dis})e^{-a\Delta}$, with $a = 11.16$, $e_{dis} = -0.6500$ and $e_{perf} = -0.6429$. The asymptotic value of the GS energy e_{dis} represents the average value of the ground state energy of maximally randomized Penrose approximants, which lies, clearly, somewhat below the GS energy of the perfect system. In other words, overall,

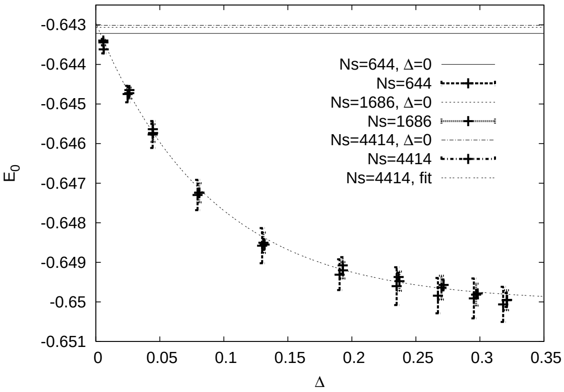

Figure 6.7: Ground state energy as a function of increasing disorder Δ at three different system sizes (N=644, 1686, 4414). The horizontal lines are the ground state energy for the perfect tiling at the same system sizes. The vertical bars indicate the standard deviation for sample-to-sample fluctuations. The exponential curve is a fit of the data points of the biggest system size to the function of $e_0 = e_{dis} + (e_{perf} - e_{dis})e^{-a\Delta}$.

the nearest neighbor bond energy increases in absolute value. This indicates that the introduction of phasons disorder tends to increase the quantum fluctuations in the tilings, as compared to the perfect case.

6.4.2 Ground state staggered magnetization

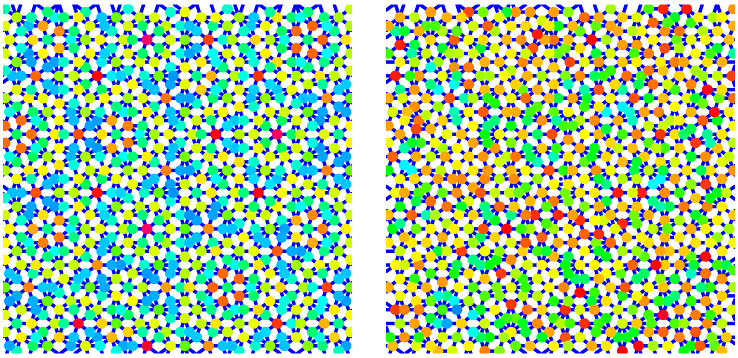

Figure 6.8: Color representation of the local staggered magnetizations in a perfect tiling (left) and a disordered tiling (right) showing sites of magnetizations ranging from high (blue) to low (red) values.

The spatial variations of the staggered magnetization in the ground state are illustrated in the right hand figure in Fig. 6.8, while the left hand figure corresponding to the data for the perfect tiling is shown for comparison. The figures show that the distribution is more homogeneous in the disordered tiling, which furthermore lacks the hierarchical features of the perfect tiling. The redder appearance of the right hand figure also illustrates that globally the magnetizations are smaller for the disordered system.

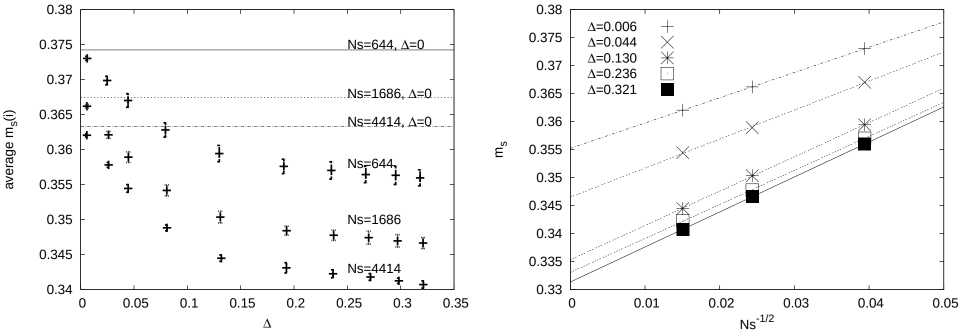

Figure 6.9: (left) Average staggered magnetizations for three different system sizes (N=644, 1686, 4414) plotted as a function of the disorder. The horizontal lines are the average staggered magnetization for the perfect tiling at the same system sizes. The vertical bars indicate the standard deviation for sample-to-sample fluctuations. (right) Finite size scaling of the average staggered magnetization for different degree of phason disorder.

Now we show the results of the average ground state staggered magnetizations. Fig. 6.9 (left) shows the global average of the staggered magnetization, after averaging over all of the sites, for three different system sizes as a function of disorder. The curve shows the decrease in the global staggered magnetization with increasing disorder. As for the ground state energy curve, the decrease is at first exponential and then levels off. We have carried out a finite size scaling (Fig. 6.9 (right)) for different degrees of phason disorder, using the fit to the $N^{-1/2}$ function. As in the perfect tiling, average magnetizations seem to scale with $N^{-1/2}$ as for periodic systems [98]. The expectation values of the average staggered magnetizations for the thermodynamic limit are presented in the Fig. 6.12. The average staggered magnetization dependence show the same type of exponential dependence from the degree of disorder as the ground state energy. A linear rescaling of the data for the ground state energy and the average staggered magnetization ($L(x) = (x - x_{min})/(x_{max} - x_{min})$) shows that these quantities have similar dependence from the degree of disorder, as seen in Fig. 6.10. We have not so far found an explanation for this proportionality which holds for all concentrations of phason disorder.

One can calculate the evolution of the distribution of staggered magnetizations with increasing phason disorder. In the perfect tiling, this distribution has several peaks, each

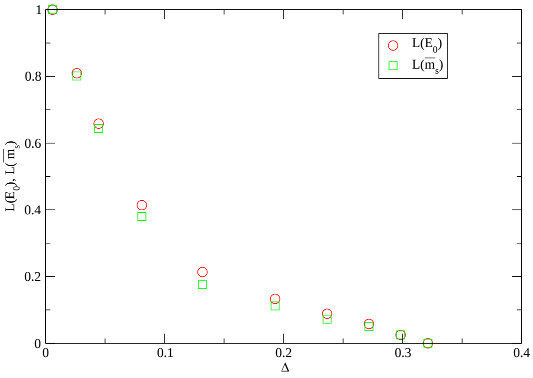

Figure 6.10: The ground state energy and average staggered magnetization transformed linearly versus phason disorder ($L(x) = (x - x_{min})/(x_{max} - x_{min})$). The two quantity seems to show approximately linear dependence from each other.

of which corresponds to a distinct coordination number. In the disordered tilings, the differences between different coordination numbers is smoothed out. As Fig. 6.11 shows, the distribution becomes smoother as disorder is increased. In addition, the average value shifts to lower values. The smoothing occurs due to a greater number of local environments created by the phason flips, and due to the loss of self similarity at large length scales. The distribution of the staggered magnetizations seems to be more ”sensitive” (i.e. changing more) to the increasing phason disorder than the average magnetizations.

The results for the staggered magnetizations can be qualitatively explained in terms of a finite cluster model [102]. In this approximation, the local environment is retained up to second neighbor level in the spin wave calculation. With this simple approximation many of the results can be obtained, using data about nearest neighbor and next nearest neighbor coordination number as input structural parameters. We conclude from this that the local staggered magnetization values are dependent mainly on the local environments for the perfect as well as the disordered Penrose tilings (Fig. 6.12 inset).

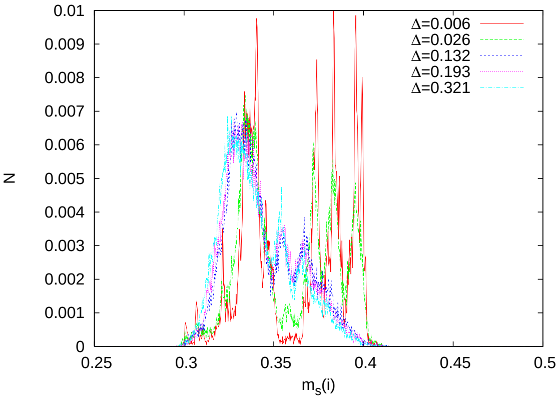

Figure 6.11: Evolution of the staggered magnetization distribution for different degrees of disorder. The system size we considered is N=4414.

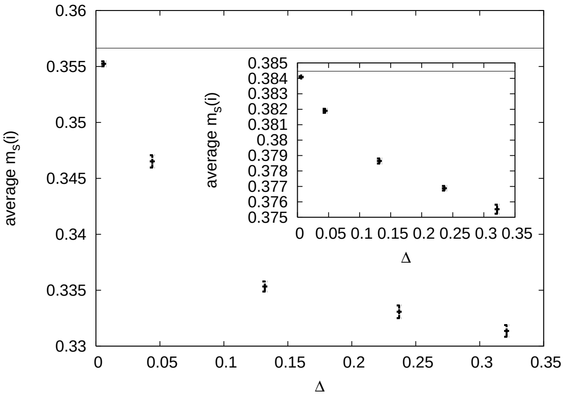

Figure 6.12: Average local staggered magnetization in the case of different degree of disorder (Δ). The straight line is the average local staggered magnetization for the perfect Penrose tiling approximant. We considered the expectation values for the thermodynamic limit. In the inset: local staggered magnetization on the central site of a two level Heisenberg-star cluster. We use the same coordination number distribution like the whole tiling has in the case of different degree of disorder (Δ). The straight line is the average local staggered magnetization for the two level Heisenberg-star cluster using the same coordination number distribution like the perfect Penrose tiling.

Chapter 7

Discussion et perspectives

7.1 Summary

The Penrose tiling is a perfectly ordered two dimensional structure with fivefold symmetry and scale invariance. Quantum spin models on such a system can be expected to differ significantly from more conventional structures as a result of its special symmetries. We considered a Heisenberg antiferromagnet on the Penrose rhombus tiling, and showed it has an inhomogeneous Neel-ordered ground state. Spin wave energies and wavefunctions were studied in the linear spin wave approximation. A linear dispersion law was found at low energies, as in other bipartite antiferromagnets, with an effective spin wave velocity lower than in the square lattice. Spatial properties of eigenmodes were characterized in several different ways. At low energies, eigenstates were found to be relatively extended, and appeared to show multifractal scaling. At higher energies, states were found to be more localized, and, depending on the energy, confined to sites of a specified coordination number. The ground state energy of this antiferromagnet, and local staggered magnetizations were calculated. Perpendicular space projections were shown, showing the underlying simplicity of this "complex" ground state. A simple analytical model, the two-tier Heisenberg star, was presented to explain the staggered magnetization distribution in this antiferromagnetic system.

The effects of a novel type of disorder in a two dimensional quantum antiferromagnet is considered. The original bipartite structure is geometrically disordered in such a way that no frustration is introduced, and the system retains a Néel ordered ground state. We show, using a linear spin wave expansion and Quantum Monte Carlo, that the staggered moment decreases exponentially as a function of increasing disorder. The spatial distribution of staggered magnetizations becomes more homogeneous compared to the deterministic tiling, the effective spin wave velocity increases with disorder, and singularities in the magnon spectrum and wavefunctions are partly smoothed. For large disorder, the ground state energy as well as the average staggered magnetization appear to tend to a limiting value characteristic of these randomized tilings. These results are discussed and compared with the behavior found in disordered periodic lattices.

7.2 Discussion

Our work shows that linear spin wave theory agrees rather well with Quantum Monte Carlo results for the Penrose tiling. The deviations of the LSWT data from the QMC one are less than 4% in the case of local staggered magnetism and less than 2% in the case of ground state energy.

Real compounds are not good realizations of the model we have considered, because they are 1) three dimensional, 2) have essentially classical spins forming a sublattice of the full structure and 3) have frustrated couplings, as well as, probably, substitutional disorder. These features lead to a spin glass phase at very low temperatures, instead of a perfect quasiperiodic antiferromagnetic phase. However, short range effects are observed and the structure factor measured in neutron diffraction looks qualitatively similar to our theoretical one. We hope however, that it will be possible to obtain a better experimental realization of our model in the future.

The ground state of the quasiperiodic antiferromagnet has a rather complex structure in real space. We have seen, interestingly, that it becomes far simpler when represented in perpendicular space. This suggests that it may be useful in future studies to carry out detailed analyses in the perpendicular space representation to study also magnon eigenfunctions and spin-spin correlation functions.

The real space dependence of eigenmodes shows that in different ranges of energies, states have their support on sites of a different given coordination number. At very low energies all sites participate, and the resulting eigenstates are relatively extended, as seen by the absolute values and the size dependence of the participation ratio. We should stress that one should not rely on the study of inverse participation ratio alone to give an accurate idea of the spatial extent of wavefunctions. A multifractal scaling analysis was carried out for a few low energy states, to estimate quantities such as the similarity dimension and information dimension. In general, our studies seem to show that the dimensionality of the states diminishes progressively as energy increases.

A simple analytical model, the two-tier Heisenberg star, allows us to explain qualitatively the observed z dependence of the onsite staggered magnetizations. The role of next neighbors is shown to be important in explaining the data.

Finally, we have studied the effects of phason disorder in this model for magnetism, as real compounds will certainly have some degree of this type of disorder. Phason disorder is particular characteristic of quasiperiodic structures, and does not destroy long range order in 3D structures, although it does so in the 2D case. Random tilings can be considered to be a new class of disordered antiferromagnets. We have shown in linear spin wave theory that the global value of the staggered magnetization decreases, as does the ground state energy, both tending towards a new limiting value characteristic of a maximally disordered system. The effective low energy spin wave velocity increases with increasing disorder, and eigenmodes tend to be more delocalized compared to the perfect tiling. In analogy with electronic problem, it appears that the effect of disorder is to reduce the strong coherent backscattering of the magnon wavefunctions due to a perfect quasiperiodic potential and favor a diffusive dynamics. A Quantum Monte Carlo study of this model is under way.

7.3 Perspectives

There are several possible perspective of our works. We figure out two of them.

7.3.1 Linear spin wave study of the 3D icosahedral tiling

To understand better the magnetism in the quasiperiodic rare earth compounds it would be definitely useful to extend our analysis to the 3 dimensional icosahedral tiling. Using the same physical model and calculation tools it would be possible to perform spin wave analysis in periodic approximants of the 3D Penrose or icosahedral tiling. These calculations would be more precise because of the generally higher coordination numbers in 3D.

7.3.2 Entanglement properties of the 2D Penrose tiling

Recently the quantum entanglement properties of many body systems is a very intensively studied topic. Most of the achievement has done in one dimension but there are many works also in higher dimensional systems also [128, 129]. There are several work on studying entanglement properties on 1D quasiperiodic systems [130, 131]. Both of these works are agree in that the entanglement properties of quasiperiodic chains are different than for periodic chains. It would be interesting to investigate the entanglement properties of spin systems on quasiperiodic 2D tilings, namely on Penrose tiling. The main question in this problem is the theoretical approach what one could use in this problem. There are just a few theoretical approach that could give the wave functions for 2D systems with at least a reasonable fidelity (in a realistic CPU time). The magnon wavefunctions could be easily calculated for enough big systems with a reasonable precision. The main question of this approach is that this semiclassical approximation could keep the properties of quantum correlations like entanglement or destroy them. Some part of the quantum correlations surely will be destroyed e.g. higher order tangles, but it could remain some type of correlation. This type of quantum correlation could be enough to give some phenomenological description and/or approximative results.

Appendix A

Forbidden rotational symmetries for periodic crystals

Why is fivefold and the greater than six -fold rotational symmetries of the quasiperiodic structure not allowed for periodic crystals? We discuss this here briefly: a lattice by definition always has translational invariance, and possibly rotational invariance as well. The unit cell covers all of space without overlapping or leaving holes. If we consider a 3 dimensional lattice, all the rational 2 dimensional cuts of the 3 dimensional lattice will be periodic also. If the lattice has rotational invariance according to a given direction in space the planes of the cuts of the 3 dimensional lattice should include the rotational and translational symmetry also. Because of this the unit cell of this plane should be n-sided regular polygon if the rotational symmetry is n-fold. The rotational symmetric (regular) polygons that could cover the hole two dimensional plane like unit cell should are the three, four, and six - sided regular polygons. The reason is that the internal angles of the n-sided regular polygons $(\pi - \frac{2\pi}{n})$ should be the integral fractions of 2π. This means for regular n-sided regular polygons:

$$\frac{2n}{n-2} := integer \tag{A.1}$$

This is true for $n = 3, 4$ and 6 but false for all other n value, showing that only 3, 4 and 6 -fold rotational symmetries must exist for periodic structures, while 5-fold symmetry for example is ruled out.

Appendix B

The oblique projection method

As we have mentioned the quasiperiodic approximants are useful for calculations with the physical model, because of the possibility of applying periodic boundary conditions. For generating the approximants one can use a generalized method of the 'cut and project' method, the 'oblique projection' method. Using this method one is able to generate periodic tilings that are built up from the same building elements as the perfect quasiperiodic tiling. Our description is a generalization of the oblique projection method described in [88] (M. Duneau and M. Audier: Approximants of the Penrose tiling) to arbitrary dimensions and tilings. Our description of the oblique projection method is based on the cut and project method described in Ch. 2. and uses the same notation as was used there.

In the cut and project method the subspace $E_{||}$ is the same time the "selection subspace" and also the "physical subspace" that will be tiled. $E_{||}$ is the selection subspace in that sense that orthogonal to the perpendicular subspace $E_{\perp}$. This equivalence is not mandatory: the selection subspace and the physical subspace could be two different subspaces. One could distinguish the physical subspace $E_{||}$ and the selection subspace $\tilde{E}_{||}$. The structural roles of the two subspace are different. The selection subspace determines the long range structure of the tiling. If the orientation of $\tilde{E}_{||}$ compare to Λ is irrational (rational) then the tiling will be quasiperiodic (periodic). The orientation of $E_{||}$ determines the local geometry of the structure: the shapes and dimensions of the building blocks. To have the same building blocks for the approximant tiling one should use the same $E_{||}$ subspace for physical space like $E_{||}$ for the cut and project method. However, one should redefine the orientation of $\tilde{E}_{||}$ to have a rational orientation to get a periodic lattice. One could define the new orientation of $\tilde{E}_{||}$ with $\vec{A}$:

$$\vec{A} = (\vec{a}_1, \vec{a}_2, \dots, \vec{a}_{N_{||}}) \tag{B.1}$$

The orientation of $\vec{A}$ should be close to the irrational orientation of $E_{||}$. The closer the orientation of $\vec{A}$ to the irrational orientation, the longer are the periodic lengths of the rational approximant. One can get the periodic lengths from the parallel projection:

$$\vec{A}_{||} = \Pi_{||}(\vec{A}) \tag{B.2}$$

where the component of $\vec{A}_{||}$ are the periodic lengths of the periodic approximant.

One should redefine also the perpendicular subspace and projection. The redefined perpendicular projection, $\tilde{\Pi}_{\perp}$, should fulfill the following equations:

$$\tilde{\Pi}_{\perp}(\vec{A}) = \vec{0} \tag{B.3}$$

because the perpendicular subspace $\tilde{E}_{\perp}$ is always orthogonal to the $\tilde{E}_{||}$ parallel one. The $\tilde{\Pi}_{\perp}$ will have the following form:

$$\tilde{\Pi}_{\perp} = \Pi_{\perp} + \epsilon \cdot \Pi_{||} \tag{B.4}$$

One can define also the original perpendicular projection of $\vec{A}$: $\vec{A}_{\perp} = \Pi_{\perp}(\vec{A})$. Using (B.3) one determines ϵ:

$$\epsilon = -\vec{A}_{\perp}(\vec{A}_{||})^{-1} \tag{B.5}$$

Using ϵ one can define $\tilde{\Pi}_{\perp}$. Changing $\Pi_{\perp}$ to $\tilde{\Pi}_{\perp}$ the tiling generation method will be the same as in the cut and project method. One projects all the $X \in \Lambda = \mathbb{Z}^N$ points to $E_{||}$ using $\Pi_{||}$ that fulfill

$$\tilde{\Pi}_{\perp}(X) \in \tilde{\Pi}_{\perp}(C) \tag{B.6}$$

where C is again the unit hypercube of $\mathbb{R}^N$.

As an example, in the case of our Taylor τ^3 approximant, we have

$$\vec{a}_1 = \{10, 3, -8, -8, 3\} \tag{B.7}$$

$$\vec{a}_2 = \{0, 8, 5, -5, -8\} \tag{B.8}$$

with the resulting rectangular shape of sides $L_x = 24.7984$ and $L_y = 21.0948$ (see Fig.2.8 in Ch. 2.).

Appendix C

Numerical diagonalization

Here we describe the numerical implementation of the real space diagonalization method described in Ch.3. This description is based on the article [75] where one can find also an another numerical implementation for the same problem.

The main steps of the diagonalization method are the following:

- All the N sites should be ordered according to sublattice. The order of the sites that has S=1/2 (S=-1/2) classical spin expectation values has to be the same as the diagonal elements of the g, g' matrixes have the values 1 (-1), respectively. For example the simplest order when all the sites on the A sublattice should have an ordinal number: $1, \ldots, N/2$ and all the sites on the B sublattice should have an ordinal number: $N/2+1, \ldots, N$ and the diagonals of the g, g' matrixes are the first half is 1, the second half is -1.
- Preparation of the gH matrix. Using (3.14) the matrix should have the following form:

  $$H_{ii} = z(i) \text{ (the coordination number of the i site)}$$

  $$H_{ij} = 1 \text{ if the sites i and j are connected, otherwise } 0$$

  All the other elements are 0.
- Solving the eigenvalue equation numerically. One of the most suited numerical linear algebra package for large matrices is the LAPACK numerical package [132]. One can use this to calculate the λ_i eigenvalues and the Z_i eigenvectors, in the same order, respectively.
- The eigenvectors, Z_i, should fulfill the (3.22) equation. Eigenvectors connected to zero eigenvalue (zero modes) are not included in this this equation. These vectors

arise due to a global rotation of all the spins. Because of this all the zero modes have the following structure: the first half is a, the second half is -a, where a is a real number. The norm of these vectors is exactly 0 for our symmetric $N_A = N_B$ case. The remaining eigenmodes have non-nul norm and their number determines the dimensionality of g' : $(N-2) \cdot (N-2)$.

- Non-degenerate eigenvectors fulfill (3.22), if one sets:

  $$T_i = \frac{Z_i}{\sqrt{Z_i g Z_i}} \tag{C.1}$$

  For the degenerate eigenvectors one can use the Gram-Schmidt orthogonalization respect to g and g' in all degenerate subspace, respectively. One proceeds in two steps:

  a. Normalization of an eigenvector of the given subspace

  $$T_1 = \frac{Z_1}{\sqrt{Z_1 g Z_1}} \tag{C.2}$$

  b. A loop that contain an iterative orthogonalization of the other eigenvectors in the given subspace.
  FOR i = 2, N-2 {
  1. Subtraction of the orthonormalized eigenvectors:

  $$U_i = Z_i - \sum_{i>j} (T_j g T_j)(Z_i g T_j) T_j \tag{C.3}$$

  2. and again normalization of all eigenvectors:

  $$T_i = \frac{U_i}{\sqrt{U_i g U_i}} \tag{C.4}$$

  }

- At the end, we have the eigenvalues λ_i and the T matrix that contains all the information about the magnon wavefunctions.

Bibliography

[1] Peter J. Lu and Paul J. Steinhardt. Decagonal and quasi-crystalline tilings in medieval islamic architecture. *Science*, 315:1106, 2007.

[2] Roger Penrose. Pentaplexity: A class of nonperiodic tilings of the plane. *The Math. Intelligencer*, 2:32, 1979.

[3] F P M Beenker. Algebraic theory of non-periodic tilings of the plane by two simple building blocks: a square and a rhombus. Technical Report 82-WSK04, Eindhoven University of Technology, 1982.

[4] Yanfa Yan Eiji Abe and Stephen J. Pennycook. Quasicrystals as cluster aggregates. *Nature Materials*, 3:759, 2004.

[5] D. Shechtman, I. Blech, D. Gratias, and J. W. Cahn. Metallic phase with long-range orientational order and no translational symmetry. *Phys. Rev. Lett.*, 53(20):1951–1953, Nov 1984.

[6] Linus Pauling. Additional evidence from x-ray powder diffraction patterns that icosahedral quasi-crystals of intermetallic compounds are twinned cubic crystals. *Proc Natl Acad Sci U S A.*, 85:4587, 1988.

[7] Dov Levine and Paul Joseph Steinhardt. Quasicrystals: A new class of ordered structures. *Phys. Rev. Lett.*, 53(26):2477–2480, Dec 1984.

[8] Dov Levine and Paul J. Steinhardt. Quasicrystals. i. definition and structure. *Phys. Rev. B*, 34(2):596–616, Jul 1986.

[9] V. Elser. Comment on ”quasicrystals: A new class of ordered structures”. *Phys. Rev. Lett.*, 54(15):1730, Apr 1985.

[10] C.L. Henley. Random tilings with quasicrystal order: transfer-matrix approach. *Journal of Physics A*, 21:1649, 1988.

[11] P.J. Steinhardt and H.-C. Jeong. New paradigm for quasicrystals – the quasi-unit cell picture based on a single repeating unit; proof that the structure can be obtained by maximizing density of low-energy clusters. *Nature*, 382:433, 1996.

[12] K. Saitoh M. Tanaka E. Abe P.J. Steinhardt, H.-C. Jeong and A.P. Tsai. Empirical evidence for quasi-unit cell picture based on alnico. *Nature*, 396:55, 1998.

[13] P. Gummelt. *Geometriae Dedicata*, 62:1, 1996.

[14] A. I. Goldman and R. F. Kelton. Quasicrystals and crystalline approximants. *Rev. Mod. Phys.*, 65(1):213–230, Jan 1993.

[15] B. D. Biggs, S. J. Poon, and N. R. Munirathnam. Stable al-cu-ru icosahedral crystals: A new class of electronic alloys. *Phys. Rev. Lett.*, 65(21):2700–2703, Nov 1990.

[16] U Mizutani, Y Sakabe, T Shibuya, K Kishi, K Kimura, and S Takeuchi. Electron transport properties of thermodynamically stable al-cu-ru icosahedral quasicrystals. *Journal of Physics: Condensed Matter*, 2(28):6169–6178, 1990.

[17] T. Klein, C. Berger, D. Mayou, and F. Cyrot-Lackmann. Proximity of a metal-insulator transition in icosahedral phases of high structural quality. *Phys. Rev. Lett.*, 66(22):2907–2910, Jun 1991.

[18] S. J. Poon. Electronic properties of quasicrystals: an experimental review. *Advances in Physics*, 41:303, 1992.

[19] C. A. Swenson, T. A. Lograsso, N. E. Anderson, and A. R. Ross. Bridgman-grown $i - al68.9pd21.6mn9.5$ quasicrystal: Comparison of α , cp , σ , and χ with those for flux-grown samples. *Phys. Rev. B*, 70(9):094201, Sep 2004.

[20] J. J. Préjean, C. Berger, A. Sulpice, and Y. Calvayrac. Linear increase of the conductivity with the concentration of local defects in $alpdmn$ quasicrystals. *Phys. Rev. B*, 65(14):140203, Mar 2002.

[21] F. Piechon A. Jagannathan. Energy levels and their correlations in quasicrystals. arXiv:cond-mat/0611081v1 [cond-mat.str-el], 2006.

[22] P. W. Anderson. Absence of diffusion in certain random lattices. *Phys. Rev.*, 109(5):1492–1505, Mar 1958.

[23] D. Mayou and G. Trambly De Laissardière. Quantum transport in quasicrystals and complex metallic alloys. *ArXiv Condensed Matter e-prints*, January 2007.

[24] Mahito Kohmoto, Leo P. Kadanoff, and Chao Tang. Localization problem in one dimension: Mapping and escape. *Phys. Rev. Lett.*, 50(23):1870–1872, Jun 1983.

[25] Julien Vidal, Dominique Mouhanna, and Thierry Giamarchi. Correlated fermions in a one-dimensional quasiperiodic potential. *Phys. Rev. Lett.*, 83(19):3908–3911, Nov 1999.

[26] Kazuo Hida. Quasiperiodic hubbard chains. *Phys. Rev. Lett.*, 86(7):1331–1334, Feb 2001.

[27] V. E. Korepin. Completely integrable models in quasicrystals. *Communications in Mathematical Physics*, 110:157–171, March 1987.

[28] Frédéric Piéchon and A. Jagannathan. Energy-level statistics of electrons in a two-dimensional quasicrystal. *Phys. Rev. B*, 51(1):179–184, Jan 1995.

[29] F. Piechon. PhD thesis, Universite Paris-Sud, 1995.

[30] A. Jagannathan. Ground state of a two-dimensional quasiperiodic quantum antiferromagnet. *Physical Review B (Condensed Matter and Materials Physics)*, 71(11):115101, 2005.

[31] Stefan Wessel, Anuradha Jagannathan, and Stephan Haas. Quantum antiferromagnetism in quasicrystals. *Physical Review Letters*, 90(17):177205, 2003.

[32] S. Kashimoto, S. Matsuo, H. Nakano, T. Shimizu, and T. Ishimasa. Magnetic and electrical properties of a stable Zn-Mg-Ho icosahedral quasicrystal. *SOLID STATE COMMUNICATIONS*, 109:63–68, 1998.

[33] H.; Ishimasa T.; Mori M. Matsuo, S.; Nakano. Anisotropic magnetic property of single-grained $al_{68}\, pd_{23}\, mn_9$ icosahedral quasicrystals. *Journal of the Physical Society of Japan*, 62(11):4044, 1993.

[34] M. A. Chernikov, A. Bernasconi, C. Beeli, A. Schilling, and H. R. Ott. Low-temperature magnetism in icosahedral $al70mn9pd21$. *Phys. Rev. B*, 48(5):3058–3065, Aug 1993.

[35] D. Bahadur. Magnetic properties of al-based icosahedral alloys. *Progress in Crystal Growth and Characterization of Materials*, 34(1-4):287, 1997.

[36] Y. Tang Z. Luo, S. Zhang and D. Zhao. *Scr. Metall. Mater.*, 28:1513, 1993.

[37] A. Inoue A. Niikura, A.P. Tsai and T. Masumoto. *Philos. Mag. Lett.*, 69:351, 1994.

[38] A. Inoue T. Masumoto Y. Nishida K. Tsuda A.P. Tsai, A. Niikura and M. Tanaka. *Philos. Mag. Lett.*, 70:169, 1994.

[39] A. Yamamoto, S. Weber, A. Sato, K. Kato, KI Tsai, A. Niikura, K. Hiraga, A. Inoue, and T. Masumoto. Electron density of icosahedral Zn-Mg-Y quasicrystals determined by a six-dimensional maximum entropy method. *Philosophical Magazine Letters*, 73(5):247–254, 1996.

[40] Y. Hattori, A. Niikura, AP Tsai, A. Inoue, T. Masumoto, K. Fukamichi, H. Aruga-Katori, and T. Goto. Spin-glass behaviour of icosahedral Mg-Gd-Zn and Mg-Tb-Zn quasi-crystals. *Journal of Physics: Condensed Matter*, 7:2313–2320, 1995.

[41] D. Schmitt and B. Charrier. Magnetic properties of $R_8Mg_{42}Zn_{50}$ quasicrystals (R = Tb, Dy, Ho, Er). *Journal of Magnetism and Magnetic Materials*, 171:106–112, July 1997.

[42] I. R. Fisher, K. O. Cheon, A. F. Panchula, P. C. Canfield, M. Chernikov, H. R. Ott, and K. Dennis. Magnetic and transport properties of single-grain $r - mg - zn$ icosahedral quasicrystals [$r = y$, $(y1 - xgdx)$, $(y1 - xtbx)$, tb, dy, ho, and er]. *Phys. Rev. B*, 59(1):308–321, Jan 1999.

[43] B. Charrier and D. Schmitt. Dynamical and irreversible magnetic effects in i-$R_8Mg_{42}Zn_{50}$ quasicrystals (R=Tb, Dy). *Journal of Magnetism and Magnetic Materials*, 189:165–172, November 1998.

[44] DR Noakes, GM Kalvius, R. Wäppling, CE Stronach, MF White, H. Saito, and K. Fukamichi. Spin dynamics and freezing in magnetic rare-earth quasicrystals. *Physics Letters A*, 238(2-3):197–202, 1998.

[45] Benoît Charrier, Bachir Ouladdiaf, and Denys Schmitt. Observation of quasimagnetic structures in rare-earth-based icosahedral quasicrystals. *Phys. Rev. Lett.*, 78(24):4637–4640, Jun 1997.

[46] Z. Islam, I. R. Fisher, J. Zarestky, P. C. Canfield, C. Stassis, and A. I. Goldman. Reinvestigation of long-range magnetic ordering in icosahedral tb-mg-zn. *Phys. Rev. B*, 57(18):R11047–R11050, May 1998.

[47] Taku J. Sato, Hiroyuki Takakura, An Pang Tsai, and Kaoru Shibata. Anisotropic spin correlations in the zn-mg-ho icosahedral quasicrystal. *Phys. Rev. Lett.*, 81(11):2364–2367, Sep 1998.

[48] Hiroyuki Takakura Taku J. Sato and An Pang Tsai. Single crystal growth of the icosahedral zn-mg-ho quasicrystal. *Jpn. J. Appl. Phys.*, 37:L663, 1998.

[49] Taku J. Sato, Hiroyuki Takakura, An Pang Tsai, Kaoru Shibata, Kenji Ohoyama, and Ken H. Andersen. Antiferromagnetic spin correlations in the zn-mg-ho icosahedral quasicrystal. *Phys. Rev. B*, 61(1):476–486, Jan 2000.

[50] Taku J. Sato, Hiroyuki Takakura, An Pang Tsai, and Kaoru Shibata. Magnetic excitations in the zn-mg-tb icosahedral quasicrystal: An inelastic neutron scattering study. *Physical Review B (Condensed Matter and Materials Physics)*, 73(5):054417, 2006.

[51] Ferenc Iglói, Loïc Turban, Dragi Karevski, and Ferenc Szalma. Exact renormalization-group study of aperiodic ising quantum chains and directed walks. *Phys. Rev. B*, 56(17):11031–11050, Nov 1997.

[52] J. M. Luck. A classification of critical phenomena on quasi-crystals and other aperiodic structures. *EPL (Europhysics Letters)*, 24(5):359–364, 1993.

[53] Michael Schreiber Karl-Heinz Hoffmann. *Computational Statistical Physics: From Billards to Monte Carlo.* Springer, 2002.

[54] Ferenc Iglói, Péter Lajkó, and Ferenc Szalma. Critical behavior of hierarchical ising models. *Phys. Rev. B*, 52(10):7159–7165, Sep 1995.

[55] Uwe Grimm Joachim Hermisson and Michael Baake. Aperiodic ising quantum chains. *J. Phys. A*, 30:7315, 1997.

[56] H. Rieger F. Iglói, D. Karevski. Random and aperiodic quantum spin chains: A comparative study. *Eur. Phys. J. B*, 1:513, 1997.

[57] Joachim Hermisson. Aperiodic and correlated disorder in xy chains: exact results. *J. Phys. A*, 33:57, 2000.

[58] Tetsuji Tokihiro. Antiferromagnetic heisenberg model on a quasiperiodic lattice with hierarchical interactions. *Phys. Rev. B*, 41(10):7334–7337, Apr 1990.

[59] K. Hida. Density Matrix Renormalization Group Study of the S= 1/2 Antiferromagnetic Heisenberg Chains with Quasiperiodic Exchange Modulation. *Journal of the Physical Society of Japan*, 68:3177–+, October 1999.

[60] Shang-keng Ma, Chandan Dasgupta, and Chin-kun Hu. Random antiferromagnetic chain. *Phys. Rev. Lett.*, 43(19):1434–1437, Nov 1979.

[61] Chandan Dasgupta and Shang-keng Ma. Low-temperature properties of the random heisenberg antiferromagnetic chain. *Phys. Rev. B*, 22(3):1305–1319, Aug 1980.

[62] A. Szallas. Strong disorder rg study of aperiodic quantum spin chains. Master's thesis, University of Szeged, 2005.

[63] André P. Vieira. Low-energy properties of aperiodic quantum spin chains. *Physical Review Letters*, 94(7):077201, 2005.

[64] André P. Vieira. Aperiodic quantum xxz chains: Renormalization-group results. *Physical Review B (Condensed Matter and Materials Physics)*, 71(13):134408, 2005.

[65] J. M. Luck C. Godréche and H. Orland. Magnetic phase structure on the penrose lattice. *Journal of Statistical Physics*, 45:777, 1986.

[66] H. Aoyama and T. Odagaki. Renormalization Group Analysis of the Ising Model on Two-Dimensional Quasi-Lattices. *International Journal of Modern Physics B*, 2:13–35, 1988.

[67] T. Dotera and R. Abe. High Temperature Expansion for the Ising Model on the Dual Penrose Lattice. *Journal of the Physical Society of Japan*, 59:2064–+, June 1990.

[68] Y. Okabe and K. Niizeki. Phase transition of the ising model on the two-dimensional quasicrystals. 1988.

[69] Erik Schwartz Sørensen, Marko V. Jarić, and Marco Ronchetti. Ising model on penrose lattices: Boundary conditions. *Phys. Rev. B*, 44(17):9271–9282, Nov 1991.

[70] J. Carnet D. Ledue, J. Teillet and J. Dujardin. Frustrated classical xy spin systems in the two-dimensional penrose tiling. *Journal of Non-Crystalline Solids*, 153:403, 1993.

[71] E. Y. Vedmedenko, U. Grimm, and R. Wiesendanger. Noncollinear magnetic order in quasicrystals. *Phys. Rev. Lett.*, 93(7):076407, Aug 2004.

[72] R. Wiesendanger E.Y. Vedmedenko, U. Grimm. Interplay between magnetic and spatial order in quasicrystals. *Philosophical Magazine*, 86:733, 2006.

[73] E. Y. Vedmedenko, H. P. Oepen, and J. Kirschner. Decagonal quasiferromagnetic microstructure on the penrose tiling. *Phys. Rev. Lett.*, 90(13):137203, Apr 2003.

[74] R. M. White, M. Sparks, and I. Ortenburger. Diagonalization of the antiferromagnetic magnon-phonon interaction. *Phys. Rev.*, 139(2A):A450–A454, Jul 1965.

[75] Stefan Wessel and Igor Milat. Quantum fluctuations and excitations in antiferromagnetic quasicrystals. *Physical Review B (Condensed Matter and Materials Physics)*, 71(10):104427, 2005.

[76] Michel Duneau and André Katz. Quasiperiodic patterns. *Phys. Rev. Lett.*, 54(25):2688–2691, Jun 1985.

[77] C. Janot. *Quasicrystals - A Primer.* Clarendon Press Oxford, 1992.

[78] N. G. de Bruijn. *Koninklijke Ned. Akad. Weten. Proc., Ser. A*, 84:39, 1981.

[79] NG de Bruijn. *Koninklijke Ned. Akad. Weten. Proc., Ser. A*, 84:53, 1981.

[80] Joshua E. S. Socolar and Paul J. Steinhardt. Quasicrystals. ii. unit-cell configurations. *Phys. Rev. B*, 34(2):617–647, Jul 1986.

[81] P. M. de Wolff. The pseudo-symmetry of modulated crystal structures. *Acta Cryst. A*, 30:777, 1974.

[82] A. Janner and T. Janssen. Symmetry of periodically distorted crystals. *Phys. Rev. B*, 15(2):643–658, Jan 1977.

[83] A. Katz and M. Duneau. Quasiperiodic patterns and icosahedral symmetry. *J. Phys. France*, 47:181, 1986.

[84] A. Yu. Kitayev P.A. Kalugin and L.S. Levitov. 6-dimensional properties of al0.86mn0.14 alloy. *J. Phys. Lett. France*, 46:L601, 1985.

[85] V. Elser. The diffraction pattern of projected structures. *Acta Crystallographica A*, 42:36, 1986.

[86] T. Janssen. Crystallography of quasi-crystals. *Acta Cryst. A*, 42:261, 1986.

[87] Albertus Hof. *Quasicrystals, aperiodicity and lattice systems.* PhD thesis, University of Groningen, http://irs.ub.rug.nl/ppn/312857101, 1992.

[88] F. Hippert and D. Gratias, editors. *Lectures on quasicrystal.* Les Editions de Physique, 1994.

[89] N. D. Mermin and H. Wagner. Absence of ferromagnetism or antiferromagnetism in one- or two-dimensional isotropic heisenberg models. *Phys. Rev. Lett.*, 17(22):1133–1136, Nov 1966.

[90] P. C. Hohenberg. Existence of long-range order in one and two dimensions. *Phys. Rev.*, 158(2):383–386, Jun 1967.

[91] Sidney Coleman. There are no goldstone bosons in two dimensions. *Comm. Math. Phys.*, 31(4):259–264, 1973.

[92] Bethe HA. *Z Phys.*, 74:205, 1931.

[93] Anderson P.W. *Mater Res Bull.*, 8:153, 1973.

[94] D. Vaknin, S. K. Sinha, D. E. Moncton, D. C. Johnston, J. M. Newsam, C. R. Safinya, and H. E. King. Antiferromagnetism in $la2cuo4-y$. *Phys. Rev. Lett.*, 58(26):2802–2805, Jun 1987.

[95] Efstratios Manousakis. The spin-$\frac{1}{2}$ heisenberg antiferromagnet on a square lattice and its application to the cuprous oxides. *Rev. Mod. Phys.*, 63(1):1–62, Jan 1991.

[96] J. Schulenburg J. Richter and A. Honecker. *Quantum Magnetism in Two Dimensions: From Semiclassical Neel Order to Magnetic Disorder*, volume 645. Springer-Verlag Berlin Heidelberg, 2004.

[97] Zheng Weihong and C. J. Hamer. Spin-wave theory and finite-size scaling for the heisenberg antiferromagnet. *Phys. Rev. B*, 47(13):7961–7970, Apr 1993.

[98] Anders W. Sandvik. Finite-size scaling of the ground-state parameters of the two-dimensional heisenberg model. *Phys. Rev. B*, 56(18):11678–11690, Nov 1997.

[99] T.A.L. Ziman H. J. Schulz and D. Poilblanc. *J. Phys. I (France)*, 6:675, 1996.

[100] S.E. Krueger J. B. Parkinson J. Richter R. F. Bishop, D. J. J. Farnell and C. Zeng. *J. Phys. Cond. Mat.*, 12:6887, 2000.

[101] J. A. Riera J. D. Reger and A. P. Young. *J. Phys.: Condens. Matt.*, 1(1855), 1989.

[102] A. Jagannathan, A. Szallas, Stefan Wessel, and Michel Duneau. Penrose quantum antiferromagnet. *Physical Review B (Condensed Matter and Materials Physics)*, 75(21):212407, 2007.

[103] T. Holstein and H. Primakoff. Field dependence of the intrinsic domain magnetization of a ferromagnet. *Phys. Rev.*, 58(12):1098–1113, Dec 1940.

[104] P. W. Anderson. An approximate quantum theory of the antiferromagnetic ground state. *Phys. Rev.*, 86(5):694–701, Jun 1952.

[105] Robert M. White. *Quantum Theory of Magnetism.* Springer-Verlag, 1983.

[106] Assa Auerbach. *Interacting Electrons and Quantum Magnetism.* Springer-Verlag, 1994.

[107] Anders W. Sandvik and Juhani Kurkijärvi. Quantum monte carlo simulation method for spin systems. *Phys. Rev. B*, 43(7):5950–5961, Mar 1991.

[108] S. Wessel. *Quantum Monte Carlo Studies of Strongly Correlated Systems.* PhD thesis, University of Stuttgart, 2006.

[109] Olav F. Syljuåsen and Anders W. Sandvik. Quantum monte carlo with directed loops. *Phys. Rev. E*, 66(4):046701, Oct 2002.

[110] W. M. C. Foulkes, L. Mitas, R. J. Needs, and G. Rajagopal. Quantum monte carlo simulations of solids. *Rev. Mod. Phys.*, 73(1):33–83, Jan 2001.

[111] B. Kramer and A. MacKinnon. *Rep. Prog. Phys.*, 56:1469, 1993.

[112] U. Grimm and M. Schreiber. *Quasicrystals - Structure and Physical Properties.* Wiley-VCH, Weinheim, 2003.

[113] T. Janssen and M. Kohmoto. Multifractal spectral and wave-function properties of the quasiperiodic modulated-spring model. *Phys. Rev. B*, 38(9):5811–5820, Sep 1988.

[114] T. Janssen J. Los and F. Gähler. The phonon spectrum of the octagonal tiling. *International Journal of Modern Physics B (IJMPB)*, 7:1505, 1993.

[115] T. Janssen J. Los and F. Gähler. Scaling properties of vibrational spectra and eigenstates for tiling models of icosahedral quasicrystals. *J. Phys. I France*, 3:107, 1993.

[116] M. Janssen. Mutifractal Analysis of Broadly Distributed Observables at Criticality. *Arxiv preprint cond-mat/9404015.*

[117] Bodo Huckestein. Scaling theory of the integer quantum hall effect. *Rev. Mod. Phys.*, 67(2):357–396, Apr 1995.

[118] Ashvin Chhabra and Roderick V. Jensen. Direct determination of the f(α) singularity spectrum. *Phys. Rev. Lett.*, 62(12):1327–1330, Mar 1989.

[119] H. Grussbach and M. Schreiber. Determination of the mobility edge in the anderson model of localization in three dimensions by multifractal analysis. *Phys. Rev. B*, 51(1):663–666, Jan 1995.

[120] Herbert Neuberger and Timothy Ziman. Finite-size effects in heisenberg antiferromagnets. *Phys. Rev. B*, 39(4):2608–2618, Feb 1989.

[121] A. Jagannathan. Jagannathan replies:. *Physical Review Letters*, 94(2):029702, 2005.

[122] Yung-Li Wang, S. Shtrikman, and Herbert Callen. Wick's theorem for spin-1/2 operators, with an application to spin waves in antiferromagnets. *Phys. Rev.*, 148(1):419–432, Aug 1966.

[123] A. Jagannathan, R. Moessner, and Stefan Wessel. Inhomogeneous quantum antiferromagnetism on periodic lattices. *Physical Review B (Condensed Matter and Materials Physics)*, 74(18):184410, 2006.

[124] Ron Lifshitz. Magnetic quasicrystals: what can we expect to see in their neutron diffraction data? *Materials Science and Engineering, A*, 294:508, 2000.

[125] Stellan Ostlund Paul J. Steinhardt, editor. *The Physics of Quasicrystals: Lectures and Reprints.* World Scientific, 1987.

[126] W. Steurer C. L. Henley, M. de Boissieu. Discussion on clusters, phasons, and quasicrystal stabilisation. *Phil. Mag. A*, 2005.

[127] Attila Szallas and Anuradha Jagannathan. Spin waves and local magnetizations on the penrose tiling. *Physical Review B (Condensed Matter and Materials Physics)*, 77(10):104427, 2008.

[128] Luigi Amico, Rosario Fazio, Andreas Osterloh, and Vlatko Vedral. Entanglement in many-body systems. *Reviews of Modern Physics*, 80(2):517, 2008.

[129] Fabien Alet, Sylvain Capponi, Nicolas Laflorencie, and Matthieu Mambrini. Valence bond entanglement entropy. *Physical Review Letters*, 99(11):117204, 2007.

[130] F. Iglói, R. Juhász, and Z. Zimborás. Entanglement entropy of aperiodic quantum spin chains. *EPL (Europhysics Letters)*, 79(3):37001 (6pp), 2007.

[131] Róbert Juhász and Zoltán Zimborás. Entanglement entropy in aperiodic singlet phases. *Journal of Statistical Mechanics: Theory and Experiment*, 2007(04):P04004, 2007.

[132] E. Anderson, Z. Bai, C. Bischof, S. Blackford, J. Demmel, J. Dongarra, J. Du Croz, A. Greenbaum, S. Hammarling, A. McKenney, and D. Sorensen. *LAPACK Users' Guide*. Society for Industrial and Applied Mathematics, Philadelphia, PA, third edition, 1999.